Dark Matter search with the CUORE-0 experiment

Candidate

Gabriele Piperno
ID number 1073894

Thesis Advisors

Prof. Fernando Ferroni
Dr. Marco Vignati

A thesis submitted in partial fulfillment of the requirements
for the degree of Doctor of Philosophy in Physics

June 3rd, 2015

Thesis not yet defended

EMAIL: gabriele.piperno@roma1.infn.it

Contents

Introduction

Last decades of astronomical and cosmological observations tell us that our knowledge of the Universe covers a minimum part of it: the Standard Model of particle physics describes only the 5% of the overall energy density components. The largest part, that accounts for the 68% of the total, seems to consist in the so-called Dark Energy, an unknown form of energy introduced to explain the accelerated expansion rate of the Universe. The remaining 27% appears to be made of non-baryonic and non-luminous matter, that for this reason is named Dark Matter.

Among all the possible candidates, the Weakly Interacting Massive Particles (WIMPs) are the today most favored to explain the Dark Matter nature. The strategy for their direct detection is based on the observation of the nuclear recoil produced by an elastic scattering between a WIMP and a target nucleus. Given the very low expected interaction rate, this search is performed with large-mass and low-background detectors located in underground laboratories. None of the experiments searching for nuclear recoils induced by WIMP interactions reported a positive observation.

Another tool that can be exploited in this research field is the signal annual modulation signature. This is an expected modulation in the flux of Dark Matter particles trapped in the Galactic Halo in a detector, due to the Earth motion around the Sun. The DAMA experiment reported a positive signal, consisting in 14 annual cycles. The comparison with other experimental results can be done only in a model dependent way, when the nature of a potential candidate is explored. Many experiments are non-sensitive to the annual modulation effect and those which are have not yet reached the DAMA sensitivity. Consequently any additional information to solve this puzzle is extremely useful.

The bolometric technique, which consists in cryogenic calorimetry, is a suitable approach for the detection of WIMPs interactions. The CUORE experiment, designed to the search of the neutrinoless double beta decay of ^{130}Te, will be the largest bolometric detector ever built. It will consists in 988 TeO$_2$ bolometers arranged in 19 towers for a total active mass of 741 kg and will start to take data by the end of 2015 in the underground Laboratori Nazionali del Gran Sasso. Thanks to the large mass and to the low energy threshold achievable, it can extend its physics potential also to study Dark Matter. A prototype of a single CUORE tower, CUORE-0, was assembled and operated since March

2013 to validate the towers production line and the analysis tools in view of CUORE. Thanks to a remarkable active mass of $39\,\mathrm{kg}$, CUORE-0, which is now in the final phase of its campaign, can be considered as an independent experiment.

This Ph.D. thesis, carried out within the CUORE collaboration, is focused on the Dark Matter search with the CUORE-0 detector. All the necessary steps, starting from the trigger implementation up to the final analysis, passing through the energy calibration, the event selection and the efficiencies evaluation, have been performed for the first time for such studies with TeO_2 bolometers.

In the first part of chapter 1 evidence for the existence of Dark Matter are summarized. In the second part the most important Dark Matter candidates are presented, focusing the attention on WIMPs.

In chapter 2, after a brief overview of WIMP detection methods, the expected signal rate for the direct detection approach is evaluated and the annual modulation effect is described. In the last part of the chapter an overview of current experiments is given.

Chapter 3 is dedicated to the bolometric technique and to the CUORE-0 detector and collected statistics.

In chapter 4 the low energy trigger is illustrated. The improvements to the trigger algorithm made during this thesis work are detailed. A study is dedicated to the trigger efficiency evaluation.

In chapter 5 the analysis procedure is presented, with particular attention to the method that was developed in this work for the validation of the energy calibration procedure.

In chapter 6 the final low-energy spectrum of CUORE-0 is shown and the results of the annual modulation study are discussed.

Chapter 1

The Dark Matter Problem

1.1 Introduction

First observations of presence of a large quantity of non lightening matters were reported in 1933 by the Swiss astronomer Fritz Zwicky [1]. He observed that the Coma cluster galaxies move faster than expected. In fact using the cluster luminosity to deduce the contained quantity of matter, he discovered that the velocity of the galaxies in the cluster was too high. This observation still holds today for scales ranging from galaxies ($\lesssim 100\,\mathrm{kpc}$) to clusters of galaxies ($\sim 100\,\mathrm{Mpc}$), only with small corrections. In all cases the mass that shines is too small to explain the total gravitational effect. To solve this problem, Zwicky proposed the presence of non visible matter, afterwards called *Dark Matter* (DM), to account for the remaining needed mass.

In the next pages, after a brief introduction to the Standard Cosmological Model, evidence for the existence of DM and some of the most important candidates will be reviewed.

1.2 Standard Cosmological Model

The current cosmological model is based on few assumptions [2]. First of all, the laws of physics are assumed to hold in all local inertial frames, an axiom known as *Lorentz invariance*. Secondly, the Copernican principle is assumed: the location of the Earth in the Universe is not special or particularly different from any other location. This, in addiction to the observed isotropy of the Universe, leads to its homogeneity (*Cosmological Principle*). When combined with the further assumption that the spatial component of the metric can be time-dependent, this implies that a specific metric must be used, known as the Robertson-Walker metric:

$$ds^2 = dt^2 - a^2(t) \left(\frac{dr^2}{1 - kr^2} + r^2 d\theta^2 + r^2 \sin^2\theta d\phi^2 \right)$$

where r, θ and ϕ are the fixed comoving coordinates of the observer, $a(t)$ is the cosmic scale factor that describes the expansion or contraction of the Universe and k is the parameter that defines the Universe curvature. The energy content of the Universe is directly connected with k, which can assume three different values: $k = -1$, hyperbolic curvature for an open, infinite Universe, $k = 0$, no curvature for a flat infinite Universe and $k = 1$, spherical curvature for a closed and finite Universe. The simplest case, $k = 0$, is the flat Euclidean space.

In any case, with the Robertson-Walker metric, the Einstein equations of general relativity simplify to the Einstein-Friedmann equations, which determine the time evolution of the cosmic scale factor as a function of the cosmological constant Λ and of the cosmic substrate density $\rho(t)$ and pressure $p(t)$:

$$\left(\frac{\dot{a}(t)}{a(t)}\right)^2 = \frac{8\pi G}{3}\rho(t) - \frac{k}{a^2(t)} + \frac{\Lambda}{3} \tag{1.1}$$

$$\frac{\ddot{a}(t)}{a(t)} = -\frac{4\pi G}{3}(\rho(t) + 3p(t)) + \frac{\Lambda}{3} \tag{1.2}$$

where G is Newton's gravitational constant. Generally one refers to the ratio $\frac{\dot{a}(t)}{a(t)} = H(t)$ as the *Hubble parameter*, which describes the expansion rate of the Universe.

It is possible to define a critical density at the present epoch t_0 that holds assuming a flat Universe ($k = 0$) with vanishing Λ model:

$$\rho_{c,0} = \frac{3H_0^2}{8\pi G}.$$

In fact this was originally intended for the determination of the Universe geometry: if $k = 1$, $\rho > \rho_{c,0}$ for a closed Universe, while if $k = -1$, $\rho < \rho_{c,0}$ for a open hyperbolic Universe. In $\rho_{c,0}$ definition only constants appear, so it is a constant itself. In particular, according to the latest results, the Hubble parameter H_0, has a value of $67.80 \pm 0.77\,(\mathrm{km/s})/\mathrm{Mpc}$ [3] and therefore $\rho_{c,0} = 8.6\,\mathrm{g/cm}^3$.

Defining the normalized densities:

$$\Omega_m(t) = \frac{\rho(t)}{\rho_{c,0}}$$

$$\Omega_k(t) = -\frac{k}{a^2(t)H_0^2}$$

$$\Omega_\Lambda(t) = \frac{\Lambda}{3H_0^2}$$

it is possible to rewrite eq.(1.1) as (removing the explicit time dependency for simplicity):

$$1 = \Omega_m + \Omega_k + \Omega_\Lambda. \tag{1.3}$$

This means that the present total energy density of the Universe is directly linked to its curvature. So eq.(1.1), or its new version (1.3), and eq.(1.2) with the values of Ω_m and Ω_Λ can describe the time evolution of the Universe. The latest observations indicate that the best models to describe the Universe are those with $\Omega_\Lambda \simeq 0.68$ [3].

The non vanishing value of Ω_Λ can be interpreted, in a quantum field theory framework, as the energy density of the vacuum, generally called *Dark Energy*. Its negative pressure accounts for a repulsive gravitational interaction in general relativity. As a consequence, models with a positive Ω_Λ present a slowed down expansion that can become an accelerated expansion in a later phase of the Universe. Therefore it is fundamental to determine the values of the three variables H_0, Ω_m and Ω_Λ to understand the ultimate fate of all cosmological models with $\Omega_\Lambda \neq 0$.

1.3   Dark Matter evidence

1.3.1   Spiral galaxies

The strongest convincing observations of DM existence after the Zwicky claim in the 30's arrived in the 70's, when Rubin and Ford discovered that most of the stars in spiral galaxies orbit at roughly the same speed [4]. Assuming the gravitation model is correct, the straightforward implication is that the mass density in galaxies can not be ascribed only to the visible mass in the galactic bulge, where the largest part of the mass is seen. A spiral galaxy, such as Andromeda, consists of a central bright bulge surrounded by a rotating disk of younger stars.

Simply using Newtonian mechanics and presupposing circular orbit around the galaxy center for the stars in spiral galaxies, it is possible to estimate their rotation velocity. Using the Gauss theorem (all the mass can be assumed being in the center of the sphere with radius r) it is possible to equate the gravitational and the centrifugal forces:

$$\frac{GM(r)m}{r^2} = \frac{mv^2(r)}{r},$$

that, for the rotation velocity, leads to

$$v(r) = \sqrt{\frac{GM(r)}{r}}$$

where G is the gravitational constant and $M(r) = 4\pi \int \rho(r)r^2 dr$, with $\rho(r)$ mass density profile inside radius r. If the mass is given only by the visible components of the galaxy, outside the optical disk the velocity should fall as $\propto 1/\sqrt{r}$. The fact that, instead, the velocity is approximately constant implies that $M(r) \propto r$ and $\rho \propto 1/r^2$. An example of this behavior is given in Fig.1.1, where the rotation curve of NGC 6503 is shown. The missing mass can be accounted for by the non-visible DM with a spherical density halo.
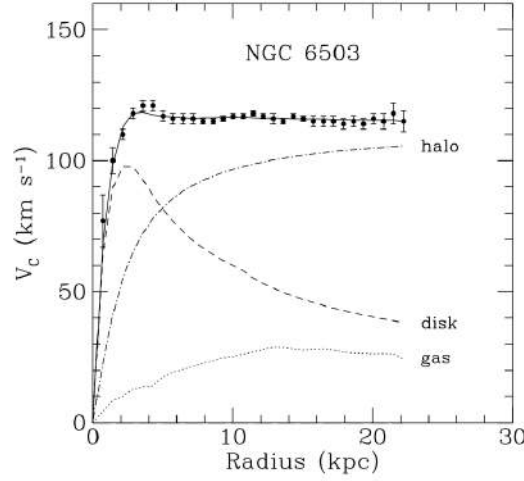
Figure 1.1: Rotation curve of NGC 6503. The dotted, dashed and dash-dotted lines are the contributions of gas, disk and dark matter, respectively. Figure from [5].

There are other convincing observations of this hypothesis: vertical velocity dispersion supports the fact that the DM cannot be contained alone in the disk, as well as material orbiting perpendicularly to the normal disk, which concludes to an almost spherical gravitational potential [6].

1.3.2   Galaxy clusters and gravitational lensing

At a much larger scale than a single galaxy there are the galaxy clusters. These are the largest gravitationally bounded structures in the Universe and consist of from hundreds to thousands galaxies to form a total mass up to 10^{18} solar masses $M_\odot$. They are formed from the gravitational collapse of regions of several Mpc of the early universe. As mentioned previously, it was from a galaxy cluster - the Coma cluster - that the first indication of the existence of a large amount of non visible matter in Universe arrived.

A typical variable used to describe the relative DM mass quantity in a cluster is the mass-to-light ratio, that represents the ratio between the mass and the luminosity of an object. For the Coma cluster this value is 400 solar masses per solar luminosity, two orders of magnitude larger than the solar neighborhood. Different studies demonstrated that this objects are largely dominated by non luminous matter [7].

There are three independent methods to study the mass of a cluster: application of the virial theorem to the cluster itself [8], X-ray of hot intra-cluster gas [9] and gravitational lensing [10].

The virial theorem states that in a system at equilibrium, which center is at rest, the average potential energy $\langle V \rangle$ is two times the average kinetic energy

$\langle T \rangle$, where average is meant over time:

$$2 \langle T \rangle = - \langle V \rangle \,.$$

Making the calculations for a cluster of N galaxies the kinetic and potential energies result to be:

$$\langle T \rangle = \frac{1}{2} N \langle mv^2 \rangle$$

$$\langle V \rangle = -\frac{1}{2} GN(N-1) \frac{\langle m^2 \rangle}{\langle r \rangle}$$

where $\langle m \rangle$ and $\langle r \rangle$ are the average mass and distance from the center, respectively. In particular $\langle V \rangle$ has been derived as follows from the gravitational potential energy:

$$V = \sum_i^N \sum_{j<i} \frac{Gm_i m_j}{r_{ij}} = G \sum_i^N \sum_{j<i} \frac{\langle m^2 \rangle}{\langle r \rangle} = G \frac{N(N-1)}{2} \frac{\langle m^2 \rangle}{\langle r \rangle}$$

applying the substitutions $m_i m_j \to \langle m^2 \rangle$ and $r_{ij} \to \langle r \rangle$ considering the sum over all the elements. Hence, inserting the two energy formulas in the virial theorem, the total dynamic mass is:

$$M \simeq 2 \frac{\langle r \rangle \langle v^2 \rangle}{G}$$

using $N - 1 \simeq N$ and $N \langle m \rangle = M$, where M is the cluster mass. Generally M results to be larger than the luminous matter amount, giving indications of the presence of a large quantity of non visible matter.

The second way to evaluate the total mass is to measure the X-ray profiles of hot intracluster gas. In fact fitting these profiles with temperature and density distribution models, under the hypothesis of hydrostatic equilibrium, it is possible to determine the mass of the cluster. Similarly to the virial theorem application, results indicate the presence of a large, unseen, portion of matter.

Finally, the gravitational lensing is based on the gravitational effect of the cluster mass on light coming from a behind source. The general relativity foreseen a deviation angle α for a light ray passing at distance r from a mass M given by

$$\alpha = 4 \frac{GM}{c^2 r}$$

where c is the speed of light. If the source, the central "bending" mass and the detector are sufficiently aligned, the observer sees a luminous ring (called Einstein ring) due to light distortion, which is tangential to the center of the gravitational potential (e.g. in Fig.1.2). As as in previous cases, the typical measured mass is larger than the luminous one. Additionally in Fig.1.3 there is the comparison between the dispersion velocities of the galaxies as obtained by X-ray measurements against the dispersion velocities as obtained from weak lensing: a good agreement between the two is evident.
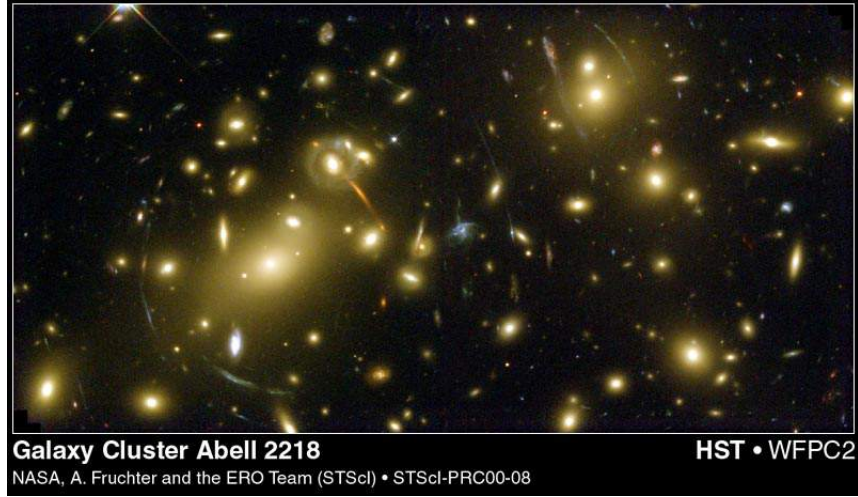
Figure 1.2: Gravitational lensing example. Giant luminous arcs and many arclets are visible. They are produced by the bending of light due to the Abell 2218 cluster mass. Image from Hubble Space Telescope [11].
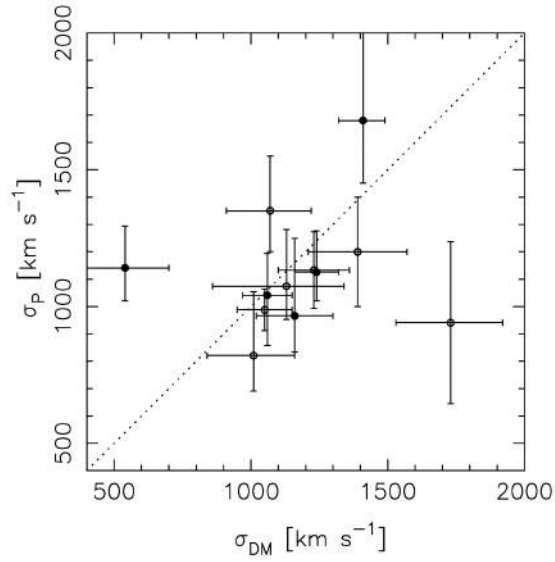
Figure 1.3: Scatter plot of spettroscopically measured velocity dispersion σ_P from X-ray vs DM velocity dispersion σ_{DM} from weak lensing measurements. Each point represents a galaxy cluster and errors indicates $1\,\sigma$. The dotted line represent equality between the two velocity. Figure from [12].

1.3.3 The early Universe

On distance scales of the size of galaxies and clusters of galaxies, evidence of DM appears to be compelling. Despite this, the observations discussed do not permit a determination of the total amount of Dark Matter in the Universe. In subsequent sections will be shown how such information can be extracted from the study of the Cosmic Microwave Background and from the analysis of the light nuclei abundances related to the Big Bang Nucleosynthesis.

1.3.3.1 Cosmic Microwave Background

Proceeding back in time, Universe becomes hotter and denser. In the firsts 400000 years after the Big Bang, temperature was larger than $\approx 3000\,$K, hence atoms were not stable and matter and radiation were in thermal equilibrium. Matter existed in an opaque plasma state of ionized atoms, which strongly absorbed electromagnetic radiation of all wavelengths. After this period, temperature was low enough to allow stable atoms formation, in particular hydrogen and helium. At this point only radiation with precise wavelengths, or with sufficient energy to ionize them, was absorbed by atoms. This is called the era of decoupling of matter and radiation, since from now on the Universe is transparent to all that wavelengths carrying energies lower than the one needed for the atoms ionization.

If the Universe began in a hot and dense state, then it should be filled with a relic background of the last scatterings before decoupling. This remnant of the transparency point, at which the expanding universe dropped below about $3000\,$K, so that radiation could escape, should have the Planck black-body spectrum:

$$\int_0^\infty \frac{\nu^3}{e^{h\nu/k_B T_r} - 1} d\nu \propto T_r^4$$

where ν is the radiation frequency, h the Planck constant, k_B the Boltzmann constant and T_r the radiation temperature. This microwave radiation takes the name of Cosmic Microwave Background (CMB) which is isotropic and constant in time. The first to measure a discrepancy from the black-body radiation was the COBE satellite, which measured an anisotropy of the order of a part in 10^5 [13]. Then other two satellites, WMAP [14] and Planck [15], measured this anisotropy with a 13 and a 5 arcminute full width at half maximum (FWHM) resolution, respectively, of the sky with their onboard instrumentation. Fig.1.4 shows the temperature fluctuations of the CMB anisotropy in the full sky as measured by Planck in combination with WMAP and $408\,$MHz observations. The microwave background temperature fluctuations record inhomogeneities in the photon-baryon fluid at the era of last-scattering. These inhomogeneities can be seen as incoherent acoustic waves in the photon-baryon fluid of the last-scattering surface, and the densities of baryonic and non-baryonic matter have strong effects upon these oscillations: baryons increase the inertia of the
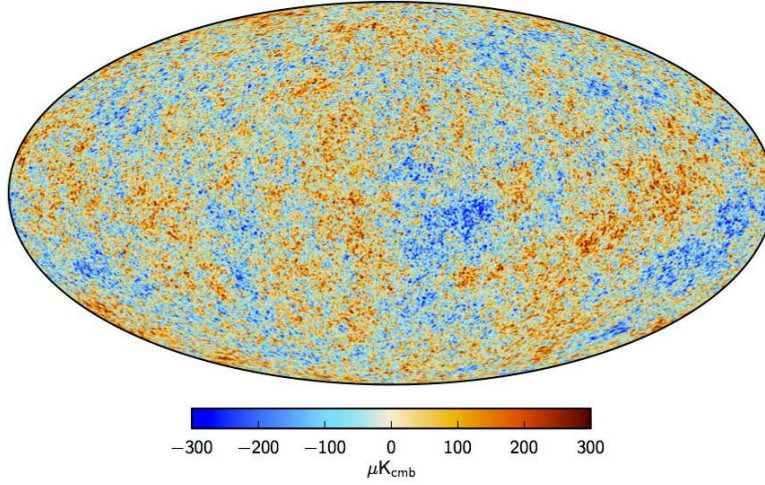
Figure 1.4: Map of temperature anisotropy from Planck in addition to WMAP and 408 MHz measurements. A 1.6% of the galactic plane is filled with a constrained realization that has the same statistical properties as the rest of the sky. The resolution is of 5 arcminute FWHM. Figure from [15].

oscillating photon-baryon fluid, while DM reduces the driving effect of those oscillations upon the gravitational potential.

Using the spherical harmonics $Y_{lm}(\theta, \phi)$ it is possible to expand the observed temperature anisotropies in the sky as

$$\frac{\delta T}{T}(\theta, \phi) = \sum_{l=2}^{+\infty} \sum_{m=-l}^{m=l} a_{lm} Y_{lm}(\theta, \phi)$$

where variance C_l of a_{lm} is

$$C_l \equiv \left\langle |a_{lm}|^2 \right\rangle \equiv \frac{1}{2l+1} \sum_{m=-l}^{m=l} |a_{lm}|^2 .$$

Given that fluctuations seem to be gaussian, all the information contained in the CMB map can be described by the power spectrum, essentially giving C_l as a function of l. In Fig.1.5 the typical variable $D_l^{TT} = l(l+1)C_l/2\pi$ is presented as a function of l, as measured from Planck. The position of the first peak allows to find that the Universe is flat/Euclidean to 0.7% ($1\,\sigma$, using only Planck data) [15], in agreement with WMAP, that measures a Ω_k equal to $-0.0027^{+0.0039}_{-0.0038}$ [14]. The peaks relative height of Fig.1.5 probes the matter and the barion densities, which result to be respectively:

$$\Omega_m h^2 = 0.1186 \pm 0.0020$$
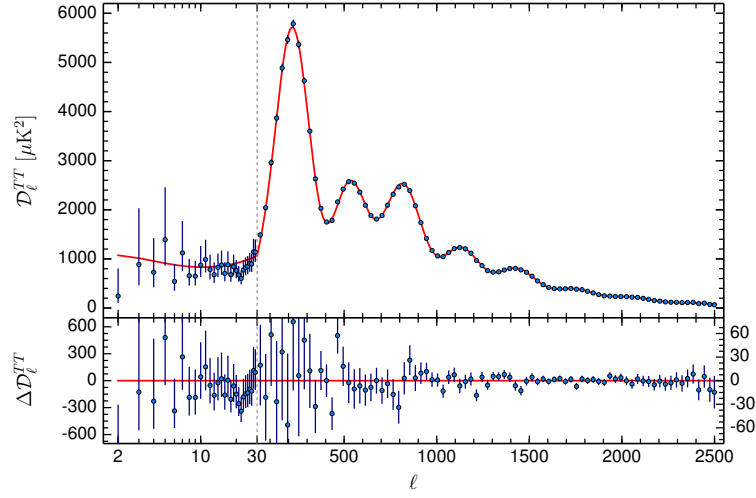
Figure 1.5: TT angular power spectrum. Points with error bars are Planck data, while the superimposed line is the best-fit CDM theoretical spectrum fitted to Planck likelihood. In the lower panel residuals are shown. The vertical line at $l = 30$ indicates that before and after this value two different fit approaches are used (see [15]). Figure from [15].

$$\Omega_b h^2 = 0.02226 \pm 0.00023$$

with numbers taken from [15]. It is evident that baryonic contribution to the total matter in the Universe is very small, even compared to the total matter quantity.

1.3.3.2   Big Bang Nucleosynthesis

To study nature on its largest scales, it is useful to turn to observations related to the early Universe. Studies of Big Bang Nucleosynthesis (BBN) lead to robust and independent measurements of the baryon density of the Universe, and therefore represent a cornerstone for the existence of non baryonic Dark Matter. Big Bang Nucleosynthesis is a non equilibrium process that took place over the course of a few minutes in an expanding, radiation-dominated plasma with high entropy and many free neutrons [16].

Light element abundances prediction of the Big Bang Nucleosynthesis are reported in Fig.1.6.

In the first 10^{-5} s of the Universe, before the QCD transition, there were roughly equal numbers of electrons, positrons, neutrinos, antineutrinos and photons. The ratio of photons to nucleons, i.e. protons and neutrons, was more than a billion to one. The nuclei had not been formed and the ratio of neutrons and protons was unity due to the weak processes that interconvert them. At

Figure 1.6: Big Bang Nucleosynthesis abundance prediction for D, ^{3}He, ^{4}He and ^{7}Li, the bands show the 95% C.L. range. Boxes indicate the light element measured abundance (smaller boxes: $\pm 2\sigma$ statistical errors; larger boxes: $\pm 2\sigma$ statistical and systematic errors). The narrow vertical band indic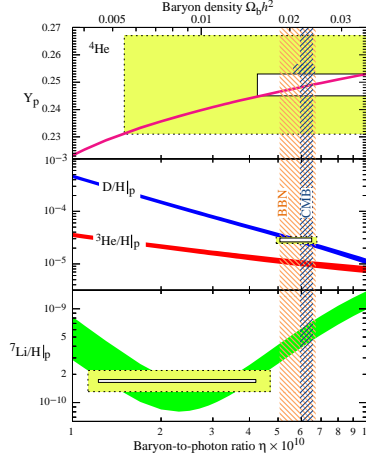ates the CMB measure of the cosmic baryon density, while the wider band indicates the BBN concordance range (both at 95% C.L.). Apart from ^{7}Li, there is a very good agreement between light elements. Figure from [17].

about one second, when the Universe had cooled to around 10^{10} K, the weak processes were not able to keep the same number of neutrons and protons. At the temperature of $\sim 10^9$ K the first formation of D, ^{3}H, ^{3}He and ^{4}He took place. As the Universe continued to expand and cool, the processes maintaining equilibrium slowed down according to the temperature evolution and, after five minutes, most neutrons were "trapped" in ^{4}He nuclei, while most protons remained free. There was also formation, in much smaller amounts, of D, ^{3}He, ^{7}Li. Subsequently, the low density and temperature caused the elemental composition of the Universe to remain unchanged until the formation of the first stars a few billion years later.

The photon density sets time and interval of nucleosynthesis through its control of the Universe expansion rate; given equal photon densities, a greater baryon density leads to a faster rate of fusion to ^{4}He and fewer nucleons left over in ^{2}H and ^{3}He. Since the photon density is well known from the microwave background black body temperature, light element ratios thus provide an excellent "baryometer" with which to measure the abundance of ordinary matter.

Looking at Fig.1.6, despite the lithium, the concordance between the elements is very good and leads to $5.1 \leq \eta \cdot 10^{10} \leq 6.5$ (95% C.L.), fundamentally bound by D/H. The precise measurement of deuterium is due to the fact that it has been created only once during BBN and it is easily destroyed in stars. Since the deuterium abundance is sensitive to η and decreases with time, any

measurement of deuterium yields a direct upper limit on η. This provides a barionic content of the Universe of $0.019 \leq \Omega_b h^2 \leq 0.024$ (95% C.L.), that means $\Omega_b \approx 0.05$ (where Ω_b is the barionic component of eq.(1.3)). These results are compatible with the ones coming from the CMB study. Hence only a small percentage of Universe consists of the same matter we are made of.

1.3.3.3   Large scale structures

The black-body nature of CMB tells that the early Universe was almost perfectly homogeneous. The inhomogeneities seen on the radiation are due to small density fluctuation. This density contrasts are enhanced by gravitation force with time, leading eventually to the formation of galaxies or clusters if the self-gravity of an overdense region becomes large enough to decouple from the overall Hubble expansion.

Currently, the Sloan Digital Sky Survey (SDSS) is systematically mapping a quarter of the entire sky and determining the position and absolute brightness of more than 100 million celestial objects [18]. This survey measures the Universe geometry by means of the distance-redshift relation in the clustering of galaxies using the Baryon Acoustic Oscillation (BAO) [19]. Latest results drives to $\Omega_m \approx 0.3$, depending on the models and on the used set of data from various experiments [20].

In addition to direct measures, cosmologists are interested in large scale structures because they provide a unique model to refer to in the realization of numerical computer simulations of the Universe. Many N-body simulations are done based on Big Bang model. Filling the primordial Universe with different composition of elements and initial density perturbation it is possible to study its evolution in time. Hence models can be refused and parameters bounded by comparing simulation results with observations.

There are fundamentally two possible models: Hot Dark Matter and Cold Dark Matter.

Hot Dark Matter (HDM) is formed by light particles ($\lesssim 100\,\text{eV}$), that remained relativistic for a long time after the Big Bang. Due to particles high speed, small area region (distances below $\approx 40\,\text{Mpc}$) fluctuations were dumped by the streaming of energy among particles. This allows formation first of large scale structures and only in a second moment of smaller ones, like galaxies. In this *Top-down* scenario, Standard Model (SM) neutrino seems to be a possible DM candidate. However, neutrino streaming results in very low density contrast on galactic scales, thus making galaxy formation nearly impossible [21].

Cold Dark Matter (CDM) is formed by heavy particles ($\gtrsim 1\,\text{GeV}$), that freezed quite soon. These particles could decouple from the cosmic fluid much earlier than baryons and are free to cluster as soon as they become non relativistic. Differently from the HDM case there is no relevant energy exchange dumping. Consequently in this picture, CDM drove, first, the formation of structures on a sub-galactic scale, that then grouped in larger systems (*Bottom-up* scenario).

The outcome of these numerical simulations to study large scale structure formation strongly support models with a cosmological constant $\Lambda \neq 0$ and a large fraction of non baryonic CDM [22]. HDM does not provide a good fit with observations, since essentially all small scale structures corresponding to supercluster scale or below are wiped out.

1.4 Dark Matter candidates

As seen in the previous section, the existence of DM is supported by many observations at all astrophysical scales. It is also undeniable that it represents a much larger fraction of the Universe than baryonic matter (about five times larger). Despite all of this, very little is known about the particle/s that make up the DM. The constrains that arise from observations are:

- DM must be stable, or at least with a long life time compared to the present age of the Universe;

- DM is probably only gravitationally/weakly interacting, since, despite its large amount, it is hard to directly detect and because of upper limits on self-interactions from astrophysical observations;

- DM nature is non baryonic, due to BBN and CMB observations, in addition to the fact that it seems to not interact with light;

- DM is slow moving, since CDM models better reproduce the current Universe structure and content.

There are many DM particle candidates, with masses ranging from $10^{-5}\,\mathrm{eV} = 9\times10^{-72}\,\mathrm{M_\odot}$ for axions to $10^4\,\mathrm{M_\odot}$ for black holes. There are some historical candidates that do not fit one or more of the conditions above. Baryonic candidates, for example, are MAssive Compact Halo Objects (MACHOs) [23, 24, 25, 26], such as brown dwarfs (balls of H and He with masses below $0.08\,\mathrm{M_\odot}$), jupiters (masses near $0.001\,\mathrm{M_\odot}$), stellar black-hole remnants (masses near $100\,\mathrm{M_\odot}$) and neutron stars. These hypotheses have been discarded by experiments like EROS that put a stringent limit on their fraction in the halo composition (in the EROS case smaller than 25% [27]).
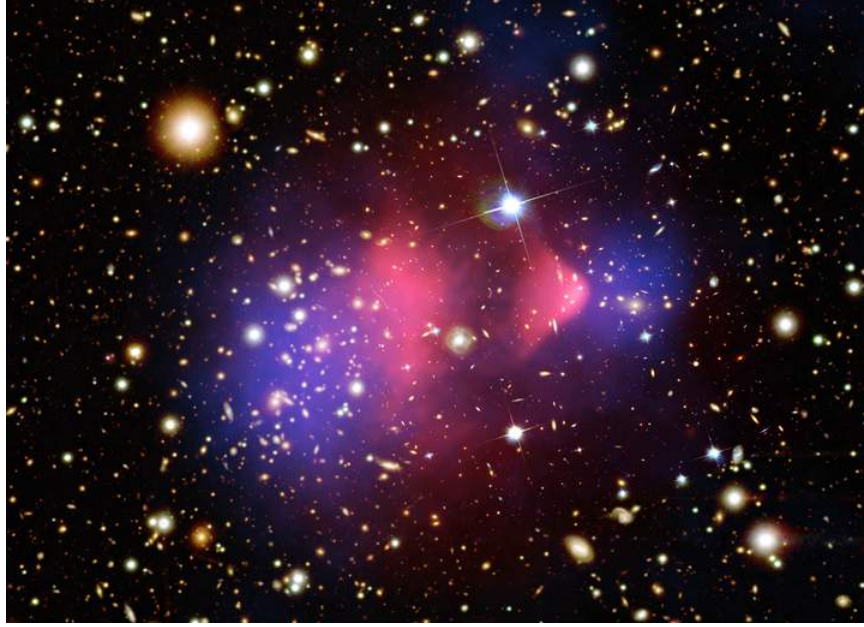
Figure 1.7: The galaxy cluster 1E0657-56, also known as the "Bullet Cluster". Color code: X-rays from intracluster medium (accounts for the largest baryonic fraction) in Pink from Chandra telescope [31], Optical (galaxies) in White/Orange from Magellan [32] and Hubble [33] telescopes and Lensing Map in Blue. Since there are two different lens centers, one can conclude that DM is the predominant mass component of the cluster. Figure from [28].

A possible explanation of the behavior observed at various scales is to modify the gravitational dependence on distance, making it decrease less rapidly than $1/r^2$. This possibility has been taken into consideration since Newton's laws have never been checked at very low accelerations, like those due to gravity at very large distances. This theory was first introduced in 1983 by Milgrom [29] under the name MOdified Newtonian Dynamics (MOND). The idea is to substitute $\vec{F} = m\vec{a}$ with

$$\vec{F} = m\mu \left(\frac{a}{a_0} \right) \vec{a}$$

where $\mu(x) = 1$ for $x \gg 1$ or $\mu(x) = x$ for $x \ll 1$ and a_0 is the constant that marks the transition between the standard Newtonian regime and the MOND one.

However, DM existence and dominance at large scale is proved by gravitational lensing of colliding galaxy clusters. In Fig.1.7 the cluster 1E0657-56 is shown, where two subcluster have collided [30]. The galaxies of two subclusters are far away each other after the interaction, having passed with no collisions.

The intracluster medium, instead, heats up and lags back near the interaction point, because of the collisions.

Using gravitational lensing it is possible to test the DM hypothesis. If DM, which undergoes no electromagnetic or strong interactions, is the predominant component of the subclusters, being low self-interacting, two different lens centers should be visible, near the concentration of galaxies. On the contrary if the intracluster medium is the larger component, basing on the mass-to-light ratio of galaxies and clusters explained by modified gravity, the weak lensing should show one center, near the gas.

The system mapping with gravitational lensing shows that there are two centers (the blue regions in Fig.1.7), one per subcluster region, rather than only one located on the gas, where the most of the baryonic matter is concentrated [30, 34]. Weakly interacting DM would move together with the galaxies, and therefore explains the observed system. There are other examples of colliding clusters of galaxies, all showing the same behavior, which supports the non-baryonic CDM model [35, 36]. Therefore, these observations fundamentally rule out the MOND theories and provide a direct and model-independent observation and proof of the existence of DM.

In the following sections, historical DM particle candidates will be presented, focussing in particular on the Weakly Interacting Massive Particles, which are the actual most favorite DM candidate.

1.4.1   Standard Model and sterile neutrinos

The only non-baryonic, massive, long-lived particle within the SM is the neutrino. The SM predicts a massless neutrino, but several experimental results on oscillations require a non-null mass [37, 38, 39, 40]. Even if they cannot be the dominant constituent of the DM, as seen in sec.1.3.3.3, they can contribute significantly to the total density. The density of neutrinos Ω_ν as a function of their assumed masses m_{ν_i} is given by:

$$\Omega_\nu = \frac{8\pi G}{3H_0^2} n_\nu \sum_i m_{\nu_i}$$

where n_ν is the current number density of neutrinos. Neutrinos decouple from other particles at a temperature of $T \approx 1\,\mathrm{MeV}$, when their reaction rate becomes less than the expansion rate of the Universe. At the decoupling moment neutrinos are still relativistic (masses $< 1\,\mathrm{MeV}$) and their number density per flavor is linked to the photon density n_γ by [19]

$$n_\nu = \frac{3}{4}\frac{4}{11} n_\gamma = \frac{3}{4}\frac{4}{11}\frac{2\zeta(3)}{\pi^2} T^3 \simeq 113\,\mathrm{cm}^{-3}$$

where $T = 2.72548\,\mathrm{K}$ is the CMB black body temperature [41], $\zeta(x)$ is the Riemann's zeta function, the factor 3/4 comes from Fermi statistics and the factor 4/11 is due to the rise of n_γ by e^+e^- annihilation. The total density

contribution for a Dirac neutrino (or half of this for a Majorana neutrino, see sec.3.3.1) can then be written as [42]:

$$\Omega_\nu = \frac{\sum\limits_i m_{\nu_i}}{93\,\text{eV}} h^{-2}$$

Given the very low neutrino masses ($\sum\limits_i m_{\nu_i} \lesssim 1\,\text{eV}$ [17]) their contribution to DM density is negligible: $\Omega_\nu \lesssim 0.07$.

Sterile neutrinos are hypothetical particles similar to SM neutrinos, with the difference that they are not weakly interacting, apart from mixing with standard neutrinos. They were proposed as DM candidates in 1993 [43]. Stringent cosmological and astrophysical constraints on sterile neutrinos come from the analysis of their cosmological abundance and the study of their decay products [44]. Sterile neutrinos could also be CDM, if there is a very small lepton asymmetry, in which case they are produced resonantly with a non thermal spectrum [45].

It is evident at this point that known SM particles are not enough to account for the full amount of DM needed in the Universe. Therefore a new, yet unknown, component of the Universe must be found expanding the current SM of particle physics.

1.4.2 Axions

Axions are hypothetical particles introduced in 1977 by Peccei and Quinn to try to solve the Strong CP Problem: strong force has been found not to violate CP as predicted by quantum chromodynamics [46]. In fact, the neutron electric moment from SM calculations should be several orders of magnitude larger than the current experimental upper limit of $10^{-26}e$ cm [47]. The theory supposes the existence of a hidden global U(1) symmetry, named the Peccei-Quinn (PQ) symmetry, which breaks spontaneously, producing a new pseudo-Nambu-Goldstone boson. This particle, the axion, relaxes the CP violation term to zero.

Axion mass is related to the PQ symmetry and is given by

$$m_a \simeq 6\,\mu\text{eV} \cdot \left(\frac{10^{12}\,\text{GeV}}{f_a}\right)$$

where f_a is the axion decay constant and is proportional to the vacuum expectation value that breaks PQ symmetry. Axion mass is unknown, but there are limits on f_a. The duration of the neutrino burst from SN1987A provides the limit $f_a \gtrsim 10^9\,\text{GeV}$ [48], while the axion energy density could not be too large, otherwise the early universe would have collapsed, hence $f_a \lesssim 10^{12}\,\text{GeV}$ [49, 50, 51]. This binds the axion mass in the range that goes from μeV to meV [52]. The axion-photon coupling $g_{a\gamma\gamma}$ is proportional to the axion mass:

$$g_{a\gamma\gamma} = \frac{\alpha g_\gamma}{\pi f_a}$$

where α is the fine structure constant and g_γ is a dimensionless, model-dependent coupling parameter of order 1 [53]. Axions may be created in the early Universe as a non relativistic condensate [50]. The average axion relic density can be estimated as

$$\Omega_a h^2 \approx \left(\frac{f_a}{10^{12}\,\text{GeV}} \right)^{7/6} .$$

Axion coupling to matter is extremely small, but its decay into two phonons can be stimulated by a resonant cavity and a strong magnetic field. All the axion detection techniques are based on the exploitation of this possibility.

Several ongoing experiments, such as CAST [54] (axions from the Sun), ADMX [55] (axions in the DM halo) and PVLAS [56] (axions produced in laboratory), are trying to detect axions, with no positive results. Ongoing and future experiments are expected to probe the couplings of axions to various particles and set limits on the contribution of axions to the Dark Matter content of the Universe.

1.4.3   Weakly Interacting Massive Particles

An extremely suitable DM candidate is represented by the Weakly Interacting Massive Particles (WIMPs), generally denoted by χ. A point in their favor is that they arise naturally in many particle models, like Supersymmetry (SUSY). These hypothetical massive particles interact only weakly and gravitationally, are non relativistic (CDM) and can be generated as a Big Bang relic with the desired density.

In the very early Universe the particles χ were in thermal equilibrium because the temperature was much higher than their mass: $T \gg M_\chi$. This resulted in a continuos process of creation and destruction: $\chi\bar{\chi} \Longleftrightarrow l\bar{l}$, where $l\bar{l}$ can be quark-antiquark, lepton-antilepton pairs, Higgs and/or boson pairs, if the mass M_χ is larger than twice the masses of these particles. In an ideal gas, the number density of these relativistic particles is $n_\chi \propto T^3$. With temperature lowering, at the moment of falling below M_χ, the particle number density falls exponentially ($n_\chi \propto e^{-M_\chi/T}$) and the annihilation rate of the WIMPs $\Gamma_\chi = \langle \sigma v \rangle n_\chi$ (σ is the thermal averaged total annihilation cross section, v is the relative velocity) becomes smaller than the expansion rate of the Universe, that is $\Gamma_\chi < H$. The annihilation of the particles then becomes inefficient and a relic abundance remains (they "freeze out"). Using Boltzmann's equation it is possible to evaluate the WIMP matter contribution:

$$\Omega_\chi = \frac{8\pi G}{3H_0^2} M_\chi n_\chi \simeq \left(\frac{3 \times 10^{-27}\,\text{cm}^3\text{s}^{-1}}{\langle \sigma v \rangle} \right) \frac{1}{h^2} \tag{1.4}$$

which approximation is independent from M_χ, and dependent only from the total annihilation cross section. In Fig.1.8 are shown numerical solutions for the Boltzmann equation. The equilibrium (solid line) and present-day (dashed lines) abundances per comoving volume are plotted as a function of m_χ/T, which

increases with increasing time. As the annihilation cross section is increased,
the WIMPs stay in equilibrium longer and the relic abundance today is smaller.
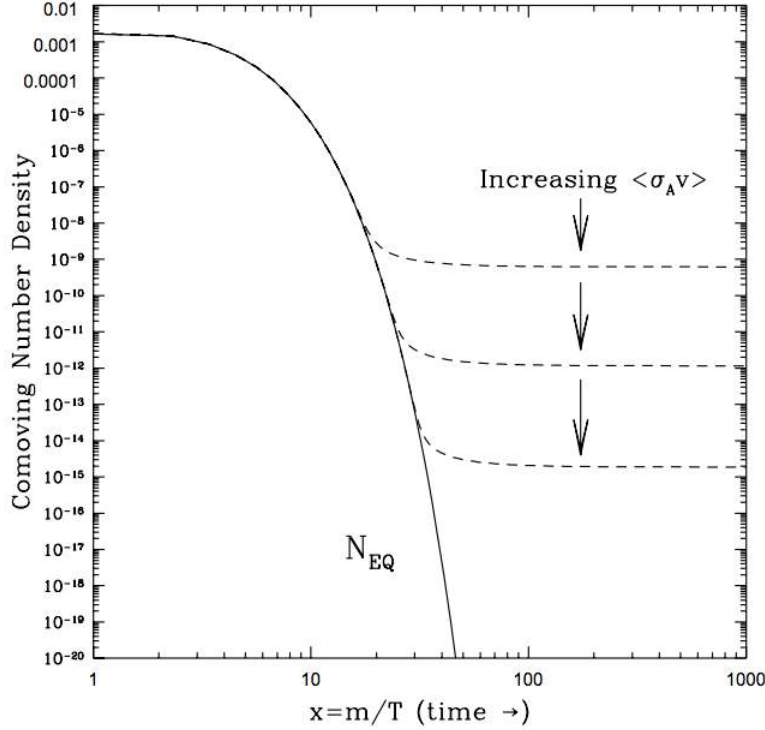
Figure 1.8: WIMP comoving number density as a function of the inverse of
the temperature (in units of M_χ). Solid line represents the equilibrium, while
the dashed lines represent the current abundances for different values of $\langle \sigma v \rangle$
(velocity-weighted annihilation cross-section). The freeze-out occurs when the
reaction rate drops below the expansion rate (for $T < M_\chi$). Figure from [57].

   As discussed in the previous section, it seems that there are no solutions
to the DM problem within the SM, so a new paradigm is needed. A possible
solution comes from Supersymmetry, already quoted at the beginning of this
section. The SUSY theory is introduced to solve the problems of the mass hi-
erarchy of particle physics as well as to unify all the non-gravitational forces
towards a Grand Unified Theory (GUT). In this model, each particle is fore-
seen to have a supersymmetric parter. The new symmetry relates elementary
particles of one spin to another particle that differs by half a unit of spin and
are known as superpartners. Since none of these supersymmetric partners has
been found, the symmetry must be broken to allow the superpartners to have
a much higher mass, allowing them to be not yet discovered. A new quantum
number is introduced, called R-parity, defined as:

$$R = (-1)^{3(B-L)+2S}$$

with B, L and S baryon, lepton and spin operators respectively. For ordinary particles $R = 1$, while superpartners have $R = -1$. If R-parity is broken, it means that there are no selection rules to prevent the decay of the supersymmetric particles in the spectrum with masses of order a few GeV or heavier. The scale of R-parity violation regulates the strength of baryon and lepton number violation processes, which have not been observed in nature so far and severe constraints on R-parity violation arise. If this R number is conserved, then a lightest supersymmetric particle (LSP) will have to be stable.

The smallest SUSY extension to the SM is called Minimal Supersymmetric Standard Model (MSSM). In [58] is presented an introduction to the SUSY model with motivation, lagrangian construnction, supersymmetric particles, MSSM and some his extensions.

Assuming supersymmetric models with the LSP being the lightest mass eigenstate of a superposition of neutral spin 1/2 fermions, namely the photino (the superpartner of the photon), the zino (the superpartner of the Z_0 boson) and the higgsino (the superpartner of the neutral Higgs boson), the so-called neutralino turns out to be an ideal DM candidate. The cosmic abundance of the neutralino, if it were a DM particle, would be determined by the freeze-out from thermal equilibrium (see eq.(1.4)) with its annihilation and scattering cross sections, as well as its mass, depending on specific parameters of the assumed supersymmetric model.

Despite the strong theoretical motivation for supersymmetry, no convincing experimental evidence for the existence of supersymmetric particles has been found so far. The search for supersymmetric particles, with masses proclaimed to be around the weak scale, is one of the prime goals of today and next generation accelerators. In particular, the Large Hadron Collider results put severe limits to the SUSY parameters and ruled out many of models [59]. Until positive results from accelerators arrive, the cosmological need for a suitable CDM candidate is the strongest empirical hint to the existence of new physics.

Beyond the discussed neutralino, there are other DM candidate particles, which currently seem almost impossible to detect. For instance, the gravitino, the spin 3/2 superpartner of the graviton, the mediator particle of gravity states from the "hidden sector" and thought responsible for supersymmetry breaking, can be a stable particle with masses in the TeV range. This would be the case if the gravitino is the LSP of R-parity-conserving supersymmetric models. Other candidates are the axino, the spin-1/2 superpartner of the axion (discussed in the previous section) and the sneutrino the superpartner of the neutrino. In addition to the presented ones, there are further DM candidates such as Kaluza Klein particles, mirror matter, inelastic DM, self-interacting DM and various other exotic matter possibilities that are not discussed here being beyond the scope of this work.

Chapter 2

Dark Matter detection

2.1 Introduction

As seen in the previous chapter, there are many compelling proofs of the existence of DM, but, despite this, practically nothing is known about it. Hence it is comprehensible the huge effort to determine its characteristics. Many experiments have been built or designed to detect WIMPs, currently the most favorite DM candidate. Beside the detection (direct or indirect, see below), there is also the possibility to directly produce these particles with accelerators, with a very small cross-section. Only by combining the information provided by many different experimental approaches, the mystery of Dark Matter particle nature can be solved.

In the next sections, a brief description of the possible experimental strategies for DM search will be given, mostly focusing on the WIMP candidate and on the direct-detection approach. In particular, the calculation of the expected WIMP rate in a detector and its annual modulation will be discussed. At the end of the chapter, a short overview of the current direct-DM-search situation will be provided.

2.2 Detection strategies

The DM search can be tackled with three different methods: accelerator production, direct and indirect detection. Each one can bring a different piece to the global mosaic. While the detection approach is of primary importance to prove the existence of DM, it is not capable of identifying most of its properties. On the contrary, the production in accelerators is the only strategy that allows to identify a long-lived weakly interacting particle, but is not able to test its cosmological stability or abundance.
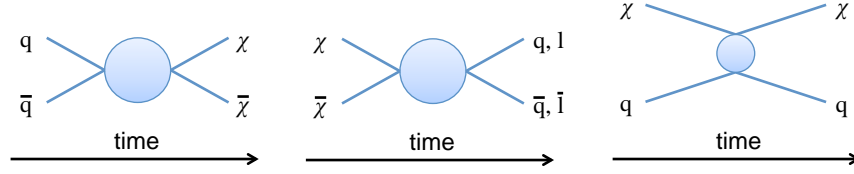
Figure 2.1: WIMPs production/detection strategy schemes. Left: accelerator production. Middle: indirect detection. Right: direct detection.

Accelerators (production scheme for hadronic machines in Fig.2.1 left) are designed to characterize particle phenomena at the electroweak symmetry breaking scale (the TeV scale). With such mass values, these particles have QCD color and therefore will be pair-produced at the LHC with a cross section in the order of tens of picobarns [60]. Hence, if DM is related to this new physics, it is possible that accelerators, like LHC second phase and the future International Linear Accelerator (ILC), may produce WIMPs.

Given their very small cross section, WIMPs are expected to escape the detector without depositing energy in it. Consequently, their fundamental signature is missing energy and momentum from a particle collision. The signature of WIMPs at the LHC would be events with many hadronic jets and an imbalance of measured momentum [61]. Direct collider constraints upon the lightest neutralino or other WIMP candidates tend to be extremely model-dependent. More in general, at the moment, collider results are less strong than the ones obtained from direct and indirect approaches.

Indirect detection (Fig.2.1 middle) is based on the search of the WIMP annihilation products. This can happen, for example, if the WIMP is the neutralino, which is a Majorana particle and therefore it is the antiparticle of itself. The annihilation of two neutralinos can occur in the galactic halo or inside astrophysical objects like the Sun or the Earth, where it should be enhanced because of the accumulation of WIMPs due to gravity.

When WIMPs annihilate, they can produce quarks, leptons, gauge bosons, Higgs bosons and gluons. One of the most favorable experimental channels is the search for positrons. The origin of positrons comes when heavier particles either decay and/or hadronize. WIMP annihilation is then expected to produce an equal mixture of electrons and positrons, but this raises the generally low positron-electron ratio from more trivial background processes. Therefore WIMP annihilation should appear as a broad excess of high energy positrons, inconsistent with the declining power laws expected from background processes. In the last years, multiple experimental results have been interpreted as possible products of WIMPs. The PAMELA experiment, which began its satellite mission in June 2006, reported an anomalous rise in the cosmic ray positron flux above $20 \div 30\,\mathrm{GeV}$ [62]. Behavior that has been confirmed also by the AMS-02 satellite experiment, launched in May 2011, on energies ten times larger [63]. This result is unexpected because positrons are predicted to be produced as secondary cosmic rays and their number should decrease with energy. The AMS-02

positron to positron-plus-electron ratio as a function of the energy in comparison with results from other experiments is shown in Fig.2.2 for energies larger than 10 GeV, point at which the positron fraction starts to rise.

At the moment there are three possible ways to explain this observation:

- Standard acceleration processes: positrons are created as secondary products by hadronic interactions in the same region where cosmic rays are accelerated. Consequently positrons present a spectrum more flat than the expected, that drives to the measured excess. Even if this process is certainly present, its intensity depends on environmental parameter values during the late stages of evolution of supernova remnants [69].

- Astrophysical sources: mature and energetic pulsars nearby can be an additional electron-positron source. In particular both of the well known nearby pulsars can produce the required AMS-02 positron flux. A very convincing piece of evidence would be an anisotropy in the the cosmic-ray electrons and positrons arrival direction. A measurement of such effect may be detectable by existing, or future, telescopes. Current AMS-02 results are consistent with the expected anisotropy. Additionally, models predict, that after the flat region, the positron fraction will begin to slowly decrease [63, 70].

- Dark Matter: DM collisions produce electron-positron pairs, that reflect in a rise in the measured positron ratio. Different models fit very well with the measured spectrum and foresee, after flattening, a rapid decrease of the flux with energy, due to the finite value of the DM particle mass. In this scenario no dipole anisotropy should be observed[63, 71, 72].

Additional information can be obtained from muon neutrinos, which can be produced by annihilation of neutralinos trapped inside the Sun or the Earth. Neutrinos, like gamma rays, maintain their original direction and for this reason they are now one of the most promising hopes for indirect detection methods with present and future neutrino telescopes. For example, the SuperKamiokande neutrino detector [73], the IceCube experiment [74] and the ANTARES neutrino telescope [75] can set limits on the rate of WIMP annihilations in the Sun.

Direct searches for WIMPs (2.1 right) are carried out in low-background underground experiments, where the direct signal of a WIMP interaction with the target nucleus is detected. This signal can be due to the nucleus recoiling after elastic scattering off WIMPs. As will be explained in the next section, the recoil energy spectrum increases roughly exponentially towards low energies and extends up to several tens of keV. Its shape mostly depends on the WIMP mass, the mass of the target nucleus and the WIMP velocity distribution.

2.3   WIMP rate in a detector

Formulae, calculations and approximations presented in this section follow [76].
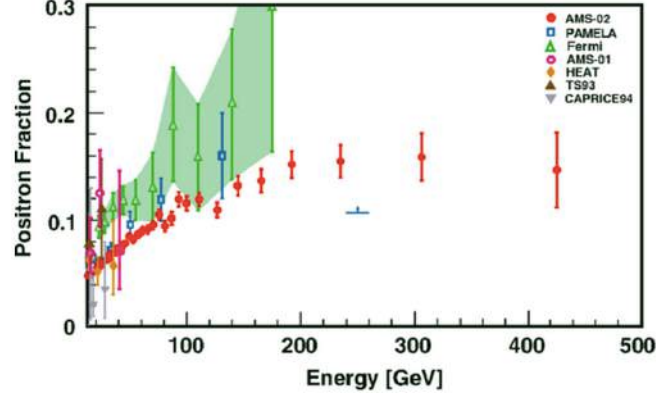
Figure 2.2: AMS-02 and other experimental measurements of the positron to positron-plus-electron fraction starting from $10\,\mathrm{GeV}$: CAPRICE94 [64], TS93 [65], HEAT [66], AMS-01 [67], Fermi [68], PAMELA [62] (which lower limit is reported as a horizontal blue line). Starting from about $200\,\mathrm{GeV}$ the positron fraction is no longer dependent on energy. The PAMELA, Fermi, AMS-01 and AMS-02 results are from space-borne experiments. Figure from [63].

The differential rate per unit mass of elastic nuclear recoils is expected to be featureless and smoothly decreasing, with the typical form:

$$\frac{dR}{dE_R} = \frac{R_0}{E_0 r} e^{-E_R/E_0 r} \tag{2.1}$$

where E_R is the recoil energy, R_0 is the total event rate, E_0 is the most probable incident kinetic energy of a DM particle of mass M_χ and $r = 4 M_\chi M_{\mathrm{A}}/(M_\chi + M_{\mathrm{A}})^2$ is a kinematic factor for a target nucleus of mass M_{A}. This equation represents the simplest case of a detector stationary in the Galaxy. In practice the real distribution is considerably more complicated due to several corrections:

- The total rate depends on the WIMP-nucleon coupling. Results will be different for spin-dependent and spin-independent interactions.

- The target consists of more than one element.

- The detector is not stationary in the Galaxy. It is on Earth, orbiting around the Sun, moving through the Galaxy with a velocity $v_E \simeq 230\,\mathrm{km/s}$.

- A nuclear form factor correction must also taken be into account, owing to the finite size of the nucleus and depending mostly on nuclear radius and recoil energy.

- In most detectors, only a fraction of the whole recoil energy is detected. True recoil energy differs from the observed one by a quenching factor $f_n \leq 1$ depending on target material and detection strategy.

2.3.1 Particle density and velocity distribution

Differential WIMP density is given by

$$dn = \frac{n_0}{k} f(\vec{v}, \vec{v}_E) d^3 v \qquad (2.2)$$

where

$$k = \int\limits_{0}^{2\pi} d\phi \int\limits_{-1}^{+1} d(\cos\theta) \int\limits_{0}^{v_{esc}} f(\vec{v}, \vec{v}_E) v^2 dv$$

is the normalization constant. Here $n_0 = \rho_\chi / M_\chi$ is the mean WIMP number density for DM density ρ_χ (standard value is $0.3\,\mathrm{GeVc}^{-2}\mathrm{cm}^{-3}$), $\vec{v}$ is the WIMP velocity relative to the Earth, $\vec{v}_E$ represents the velocity of the Earth relative to the Galaxy, v_{esc} is the local Galactic escape velocity (a good value is $600\,\mathrm{km/s}$, since $580\,\mathrm{km/s} < v_{esc} < 625\,\mathrm{km/s}$ [77]) and dn is the particle density of DM with relative velocities within d^3v about $\vec{v}$. Assuming a Maxwellian DM velocity distribution with $v_0 = 220\,\mathrm{km/s}$ [78]

$$f(\vec{v}, \vec{v}_E) = e^{-|\vec{v}+\vec{v}_E|^2/v_0^2},$$

we obtain

$$k = k_1 = k_0 \left[\mathrm{erf}\left(\frac{v_{esc}}{v_0} \right) - \frac{2}{\pi^{1/2}} \frac{v_{esc}}{v_0} e^{-v_{esc}^2/v_0^2} \right],$$

where $k_0 = \left(\pi v_0^2 \right)^{3/2}$ is the normalization in case of $v_{esc} = \infty$.

2.3.2 Differential rate

The event rate per unit mass on a target of atomic number A is

$$dR = \frac{N_a}{A} \sigma_A v\, dn$$

where N_a is Avogadro's number ($6.02 \times 10^{26}\,\mathrm{kg}^{-1}$) and σ_A is the "zero momentum transfer" cross-section per nucleus. In the case of spin-independent interaction and assuming same coupling for protons and neutrons, this cross-section can be approximate as

$$\sigma_A = \sigma_0 \frac{\mu_A^2}{\mu_n^2} A^2 \qquad (2.3)$$

where σ_0 is the WIMP-nucleon cross-section, $\mu_A = M_A M_\chi/(M_A + M_\chi)$ is the reduced mass of the "WIMP-nucleus system" and μ_n is the reduced mass of the "WIMP-nucleon system". Then:

$$R = \frac{N_a}{A} \sigma_A \int v\, dn = \frac{N_a}{A} \sigma_A n_0 \langle v \rangle. \qquad (2.4)$$

R_0 is defined as the event rate per unit mass for $v_E = 0$ and $v_{esc} = \infty$:

$$R_0 = \frac{2}{\pi^{1/2}} \frac{N_a}{A} \frac{\rho_\chi}{M_\chi} \sigma_A v_0. \qquad (2.5)$$

Substituting eq.(2.2) and eq.(2.5) in eq.(2.4), we obtain

$$R = R_0 \frac{\pi^{1/2}}{2} \frac{\langle v \rangle}{v_0} = R_0 \frac{k_0}{k} \frac{1}{2\pi v_0^4} \int v f(\vec{v}, \vec{v}_E) d^3 v$$

and the differential form

$$dR = R_0 \frac{k_0}{k} \frac{1}{2\pi v_0^4} v f(\vec{v}, \vec{v}_E) d^3 v. \qquad (2.6)$$

The recoil energy of a nucleus struck by a WIMP of kinetic energy $E = \frac{1}{2} M_\chi v^2$, scattered in centre of mass at angle θ, is

$$E_R = Er(1 - \cos\theta)/2$$

with r defined at the beginning of sec.2.3.

Assuming the scattering is isotropic, the recoils are uniformly distributed in E_R over the range $0 \le E_R \le Er$. Thus

$$\frac{dR}{dE_R} = \int_{E_{min}}^{E_{max}} \frac{1}{Er} dR(E) = \frac{1}{E_0 r} \int_{v_{min}}^{v_{max}} \frac{v_0^2}{v^2} dR(v),$$

where we define $E_0 = \frac{1}{2} M_\chi v_0^2 = \left(v_0^2/v^2 \right) E$, while $E_{min} = E_R/r$ is the smallest particle energy that can give a recoil energy of E_R and v_{min} is the DM particle velocity corresponding to E_{min}, i.e.

$$v_{min} = \sqrt{\frac{2E_{min}}{M_\chi}} = v_0 \sqrt{\frac{E_R}{E_0 r}}.$$

Substituting into eq.(2.6) it results

$$\frac{dR}{dE_R} = \frac{R_0}{E_0 r} \frac{k_0}{k} \frac{1}{2\pi v_0^2} \int_{v_{min}}^{v_{max}} \frac{1}{v} f(\vec{v}, \vec{v}_E) d^3 v$$

which, with non-zero v_E and finite $v_{max} = v_{esc}$ (again assuming a Maxwellian velocity distribution), gives

$$\frac{dR}{dE_R} = \frac{k_0}{k_1} \frac{R_0}{E_0 r} \left\{ \frac{\pi^{1/2}}{4} \frac{v_0}{v_E} \left[\text{erf}\left(\frac{v_{min} + v_E}{v_0} \right) - \text{erf}\left(\frac{v_{min} - v_E}{v_0} \right) \right] - e^{-v_{esc}^2/v_0^2} \right\}.$$
$$(2.7)$$

2.3.3 Scalar and axial-vector interactions

In the above equations, only spin-independent scattering was considered. However, interactions between nuclei and WIMP can be of two types, depending on the WIMP-quark coupling (the typical neutralino model is assumed):

- scalar or spin-independent (SI) interactions take place through the exchange of a squark or a Higgs and can be very important, especially for heavier nuclei;

- axial-vector or spin-dependent (SD) interactions take place through the exchange of a squark or a Z boson.

The theoretical calculations leading to the WIMP-nucleus cross-section from the WIMP-quark coupling will not be discussed here. The total WIMP-nucleus elastic cross section for an element with mass number A can be written as:

$$\sigma_{\mathrm{A}} = \sigma_{\mathrm{A,SI}} + \sigma_{\mathrm{A,SD}}$$

While the spin-independent cross section is proportional to $\mu_{\mathrm{A}}^2 \mathrm{A}^2$ (as can be seen in eq.(2.3)), the spin-dependent cross section is proportional to $\mu_{\mathrm{A}}^2 I_s$ [79]. The factor I_s has the form

$$I_s = \left(a_p \left\langle S_p \right\rangle + a_n \left\langle S_n \right\rangle\right)^2 J(J+1)$$

where a_p and a_n are the effective WIMP-nucleon couplings, $\langle S_p \rangle$ and $\langle S_n \rangle$ are the expectation values of the proton and neutron spins within the nucleus and J is the total nuclear spin. Only nuclei with non-zero J can have SD interactions.

2.3.4 Nuclear form factor correction

So far, the dependence on the momentum transfer ($q = \sqrt{2 M_{\mathrm{A}} E_R}$) was neglected. When the wavelength $\hbar/q$ is no longer large compared to the nuclear radius, the cross-section decreases with increasing q. It is useful to introduce a "nuclear form factor" F, a function of the dimensionless quantity qr_n (using natural units, in which $\hbar = 1$), where r_n is the effective nuclear radius. Cross-sections then behave as

$$\sigma(qr_n) = \sigma_0 F^2(qr_n)$$

considering the two different cases of SI and SD interactions. Several multiparameter fits to charge density have been proposed to calculate SI $F(qr_n)$. Among them, the distribution proposed by Helm [80] has the advantage of yielding an analytic form factor expression:

$$F(qr_n) = 3\frac{j_1(qr_n)}{qr_n}e^{-(qs)^2/2}$$
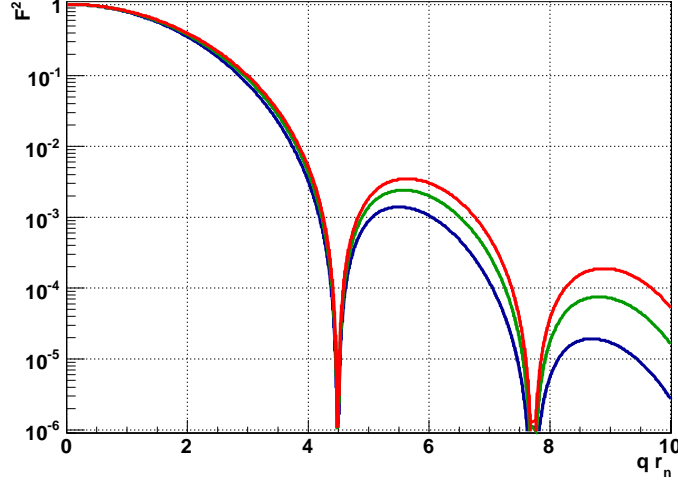
Figure 2.3: SI nuclear form factors for ^{131}Xe (in red), for ^{40}Ar (in blue) and for ^{73}Ge (in green).

where $s \simeq 0.9\,\mathrm{fm}$ is a measure of the nuclear thickness and j_1 is the first spherical Bessel function:

$$j_1(qr_n) = \frac{\sin(qr_n) - qr_n \cos(qr_n)}{(qr_n)^2}.$$

Nuclear radius can be approximated by:

$$r_n^2 = b^2 + \frac{7}{3}\pi^2 a^2 - 5s^2,$$

where $a \simeq 0.52\,\mathrm{fm}$ and $b \simeq (1.23\mathrm{A}^{1/3} - 0.60)\,\mathrm{fm}$. In Fig.2.3 are reported the obtained form factors for some typical nuclei.

In the case of SD interactions, a useful approximation is to consider only the contribution coming from the unpaired nucleon ("single particle model") or from nucleons of the same type as the unpaired nucleon ("odd-group model"). In this case the form factor can be written:

$$F(qr_n) = j_0(qr_n) = \frac{\sin(qr_n)}{qr_n}.$$

More precise calculations have been carried out for a small number of nuclei (for example see [81] and [82]).

2.3.5 Quenching factor

The signal induced by a nuclear recoil of a given energy is usually less than the signal produced by an electron recoil of the same energy. This is due to the different energy percentages going to detectable channels (light or electric charge, for example) and to undetectable ones (for example heat). The ratio f_n between observed energy and true energy is named quenching factor and can be determined by neutron scattering measurements. While spectra could be directly expressed in terms of E_R, it is usually preferred to work with the γ calibrated energies for easier identification of γ background. Consequently E_R in the above formulas should be replaced by the "visible" energy E_v, using $E_R = E_v/f_n$ and, considering possible variations of f_n with E_R,

$$\frac{dR}{dE_R} = f_n \left(1 + \frac{E_R}{f_n} \frac{df_n}{dE_R} \right) \frac{dR}{dE_v}.$$

2.3.6 Combining results

All the equations above are strongly dependent on mass number A. Since detectors are often composed of several different materials, one has to consider the different contribution of each of them. The total differential recoil rate per kg of target mass can be obtained by

$$\left. \frac{dR}{dE_R} \right|_{total} = \sum_A x_A F_A^2 \left. \frac{dR}{dE_R} \right|_A$$

where F_A^2 is the nuclear form factor for a target nucleus with mass number A, $dR/dE_R|_A$ its differential rate calculated in eq.(2.7) and x_A its fraction of the total target mass.

For example, TeO_2 bolometers (which will be introduced in the next chapter) are composed of several different Te isotopes and ^{16}O atoms (see Tab.2.1), with $f_n \simeq 1$ since in bolometers the whole energy is converted into phonons and fully detected [83]. More in detail in [83] has been measured the total energy and the single energies of the α and of the nuclear recoil of a ^{224}Ra source with a set of two TeO_2 bolometers of $2 \times 2 \times 3 \, cm^3$ faced each other. In fact, looking at ^{224}Ra events happening in single crystals it is possible to measure the total transition energy, while looking at events in coincidence between the two crystals it is possible to evaluate the single components energy (the α and the nuclear recoil). Using a γ calibration it is possible to evaluate $f = 1.025 \pm 0.3$ for the recoiling nuclei at $103.4 \, keV$. No deviation from this factor is observed with energies down to $15 \, keV$. Moreover, SD interactions in TeO_2 are negligible because it is composed almost exclusively of spin-0 nuclei and, even for the small non-zero spin isotopes, scalar cross-sections are favored by the high mass number. The obtained TeO_2 spectral function is shown in Fig.2.4 as resulting from all the modellizations and parameter values previously assumed.

Isotope	A	Natural abundance in Te	TeO$_2$ mass fraction (x_A)
^{120}Te	120	0.0009	0.0008
^{122}Te	122	0.0255	0.0204
^{123}Te	123	0.0089	0.0071
^{124}Te	124	0.0474	0.0379
^{125}Te	125	0.0707	0.0565
^{126}Te	126	0.1884	0.1506
^{128}Te	128	0.3174	0.2538
^{130}Te	130	0.3408	0.2725
^{16}O	16		0.2004

Table 2.1: TeO$_2$ bolometer composition. Data from [84].
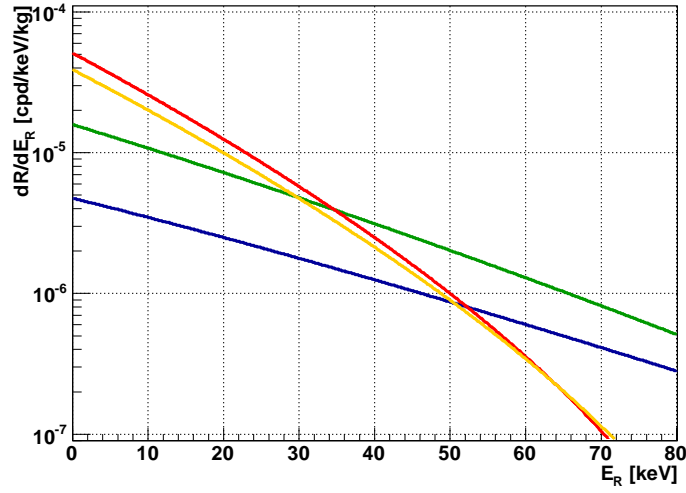
Figure 2.4: Differential rate of WIMP SI elastic scattering on TeO$_2$ (yellow), on ^{131}Xe (red), on ^{40}Ar (blue) and on ^{73}Ge (green), for $M_\chi = 100$ GeV and $\sigma_0 = 10^{-45}$ cm^2.

2.4 The annual modulation

It is important to stress out that only some experiments are able to distinguish nuclear recoils from other background events, exploiting the different interaction features of the various particles in the detector. Without this capability, direct DM searches become more complex.

In fact, the energy spectrum of WIMP-induced nuclear recoils, which can be calculated using the above formulas, is exponentially decreasing with the recoil energy in the typical range $1 \div 100\,\mathrm{keV}$ and, unfortunately, its shape is smooth and featureless. The absence of any feature in the spectrum and the low energy region where it is confined makes it practically impossible to distinguish this signal from the low energy background of the detector, which comes partially from intrinsic sources (radioactive contaminations inside the detector itself or in the nearby material) and partially from external sources, like cosmic rays and neutrons entering the detector area. It is clear now that it is impossible to detect a "positive" WIMP signal just by looking at the shape of the experimental spectrum. However, the absence of a positive signal does not mean no result at all: every experiment, providing an observation of nuclear recoils at low energy, can set limits on the WIMP presence in our Galaxy, excluding those WIMPs that would produce a nuclear recoil event rate higher than observed. Obviously, some model assumption must be made to this end. Moreover, a reduction of the background, obtained for example working in an underground site or using background suppression or discrimination methods, increases the sensitivity of the detector and allows the experiment to set more and more stringent limits to the WIMP parameters.

Saying that the WIMP induced nuclear recoil spectrum has no distinctive features is true for the shape of the spectrum but not for the WIMP signal in general. The recoil spectrum produced by WIMP-nucleus scattering in a target detector is expected to show the so-called *annual modulation* effect [85]. Since the Earth rotates around the Sun and the Sun itself moves into the galactic reference frame (see Fig.2.5 left), we can express the Earth speed with respect the Galaxy (v_E) as the sum of the two motions:

$$v_E = v_\odot + \langle v_{rot} \rangle \cos\gamma \cos(\omega(t - t_0))$$

where $v_\odot$ is the Sun speed in the galaxy, $\langle v_{rot} \rangle$ is the average Earth speed in its motion around the Sun and γ is the angle between the Earth rotation plane and the galactic plane. The period and phase of the cosine function are known to be $\omega = 2\pi/T$ ($T = 1\,y$) and $t_0 = 2^{\mathrm{nd}}$ June. It is customary to express the Earth velocity in units of the parameter v_0, defined above (sec.(2.3.1)) as the parameter of the Maxwellian WIMP speeds distribution function. The adimensional quantity $\eta = v_E/v_0$ shows the following time dependence:

$$\eta(t) = \eta_0 + \Delta\eta \cos(\omega(t - t_0))$$

where the amplitude of the annual modulated component ($\Delta\eta \simeq 0.07$) is small compared to the average value $\eta_0 \simeq 1.05$. In this framework, the expected
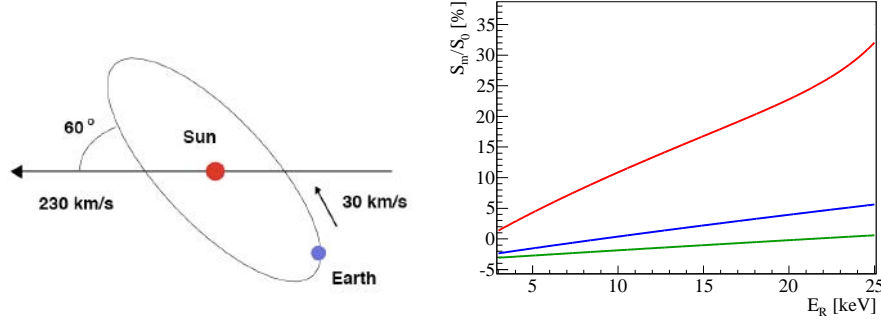
Figure 2.5: Left: The combined motion of the Earth around the Sun (average velocity $\langle v_{rot} \rangle = 30\,\text{km/s}$) and of the Sun itself with respect to the galaxy ($v_\odot = 232\,\text{km/s}$) is responsible for the annual modulation effect. Right: Predicted ratio of the modulated to the constant WIMP signal in TeO_2 for $M_\chi = 20\,\text{GeV}$ in red, $M_\chi = 50\,\text{GeV}$ in blue and $M_\chi = 100\,\text{GeV}$ in green.

WIMP signal in the Earth reference system can be written (first order Taylor approximation):

$$S = S_0 + S_m \cos(\omega(t - t_0))$$

where $S_0 = S(\eta_0)$ is the time-independent signal and $S_m = \left.\frac{\partial S}{\partial \eta}\right|_{\eta_0} \Delta\eta$ is the amplitude of the modulated signal. As we can see from the expressions of S_0 and S_m and from Fig.2.5 right, the amplitude of the annual modulation is only a few percent of the time-independent signal, strongly dependent on M_χ and E_R. Moreover, its contribution to the total signal S can be not only positive but also negative or zero. To point out the presence of such fluctuation, superimposed on a constant count rate of WIMP interactions but also background from other sources, is not an easy task. What is needed is a large mass detector, with background stable over time, very high stability of running condition and high exposure time.

Despite the difficulties related with its detection, the annual modulation effect remains the main signature of a possible DM signal, a positive indication that, if observed, would allow to constrain the WIMP parameters space with an allowed region instead of several exclusion plots. It is important to point out that two different analyses can be performed in this case: a model-independent analysis, in which only the presence of the modulation is looked for in the data and a model-dependent analysis, where, assuming a complete model framework, it is possible to allow (or to exclude) a region in the space of the parameters M_χ and σ. Therefore, if a modulation signature is discovered in the experimental data, it is possible to extract information on the WIMP relevant quantities only in the framework of a given model (for example: SI WIMP-nucleon interactions, non-rotating halo, Maxwellian distribution of WIMP velocity, Galactic escape

velocity and so on).

2.5 WIMP direct detection techniques

A variety of techniques are presently in use for WIMP searches. Due to the numerous ways to achieve sensitivities to the WIMP properties (high A, high target mass, low threshold, low background, background rejection and background subtraction techniques, *etc.*), only a few, among the most successful and most promising ones, are discussed in this section. One of the main difficulties of any such technique is the low signal rate to be expected from any model calculations. The typical count rates are much lower than the usual radioactive backgrounds. Therefore, common to all WIMP searches, is the goal to reduce the natural radioactive contamination by using extremely pure substances and to actively reject background events by special techniques.

Experimentally, there are several ways of particular importance to measure the event rate of WIMP-nucleus collisions discussed previously. First, one may search for scintillation light created by the energy deposit of the WIMP in the target detector, as in NaI or Xe detectors. Here, the recoiling particle directly or indirectly excites electrons to energy levels above their ground states, from which they may decay by emission of ultraviolet or visible photons. Due to the reasonably low background, by using ultrapure materials, and large masses achievable, scintillators are naturally used for annual modulation searches. This has been successfully done by the DAMA/NaI and DAMA/LIBRA experiments at Laboratori Nazionali del Gran Sasso (Italy), which observes an annual modulation on data taken over several annual cycles [86, 87, 88, 89]. Fitting data with the function $A\cos\omega(t - t_0)$, two cases are taken into consideration. The first, with fixed parameters, $T = \frac{2\pi}{\omega} = 1\,y$ (period) and $t_0 = 152.5\,\mathrm{d}$ (maximum position, June 2nd), which gives $A = (0.0110 \pm 0.0012)\,\mathrm{counts/day/kg/keV}$, corresponding to $9.2\,\sigma$ C.L. The second approach leaves all the parameters in the fitting procedure free, resulting in: $A = (0.0112 \pm 0.0012)\,\mathrm{counts/day/kg/keV}$ $(9.3\,\sigma$ C.L.$)$, $T = (0.998 \pm 0.002)\,y$ and $t_0 = (144 \pm 7)\,\mathrm{d}$. With the measured effect, the collaboration obtains a model-independent evidence for the presence of a DM particle component in the galactic halo (see Fig.2.6).

The deduced allowed region for the WIMP mass and the WIMP-nucleon cross section depends on the considered model. If the usual WIMP-neutralino model is considered, this allowed region is reported in Fig.2.7, together with results from other experiments. Without regard to the exception of annual modulation, the detection technology described offers little or no direct background rejection capability. An important background rejection technique, possible with many detectors, is nuclear recoil discrimination. In NaI scintillators, this can be achieved by pulse shape analysis, since nuclear recoils produce scintillation pulses that decay more quickly than those produced by electron recoils.

Liquid noble gas detectors with scintillation readout have shown competitive WIMP sensitivities. Most notable has been liquid xenon (LXe), started by
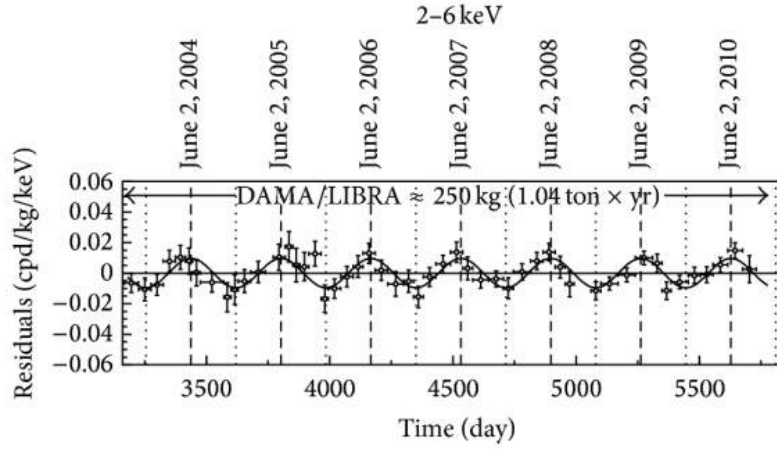
Figure 2.6: Experimental residual rate of DAMA of the single-hit scintillation events measured by DAMA/LIBRA-phase1 in the $(2 \div 6)\,\mathrm{keV}$ energy interval as a function of the time. Vertical bars are the experimental point errors, while the horizontal bars are the time bin width. The superimposed curve is the expected signal modulation: $A\cos\omega(t - t_0)$, with period $T = \frac{2\pi}{\omega} = 1\,y$, maximum at $t_0 = 152.5\,\mathrm{d}$ (June 2nd) and amplitude given by central value resulting from the best fit to the data. The dotted and the dashed vertical lines represent the positions of minima and maxima of the expected DM signal modulation, respectively. Depending on the fitting procedure adopted, the results are: $A = (0.0112 \pm 0.0012)\,\mathrm{counts/day/kg/keV}$ with A, T and t_0 free to vary, or in $A = (0.0110 \pm 0.0012)\,\mathrm{counts/day/kg/keV}$ with fixed T and t_0. Figure from [89].

DATA listed top to bottom on plot

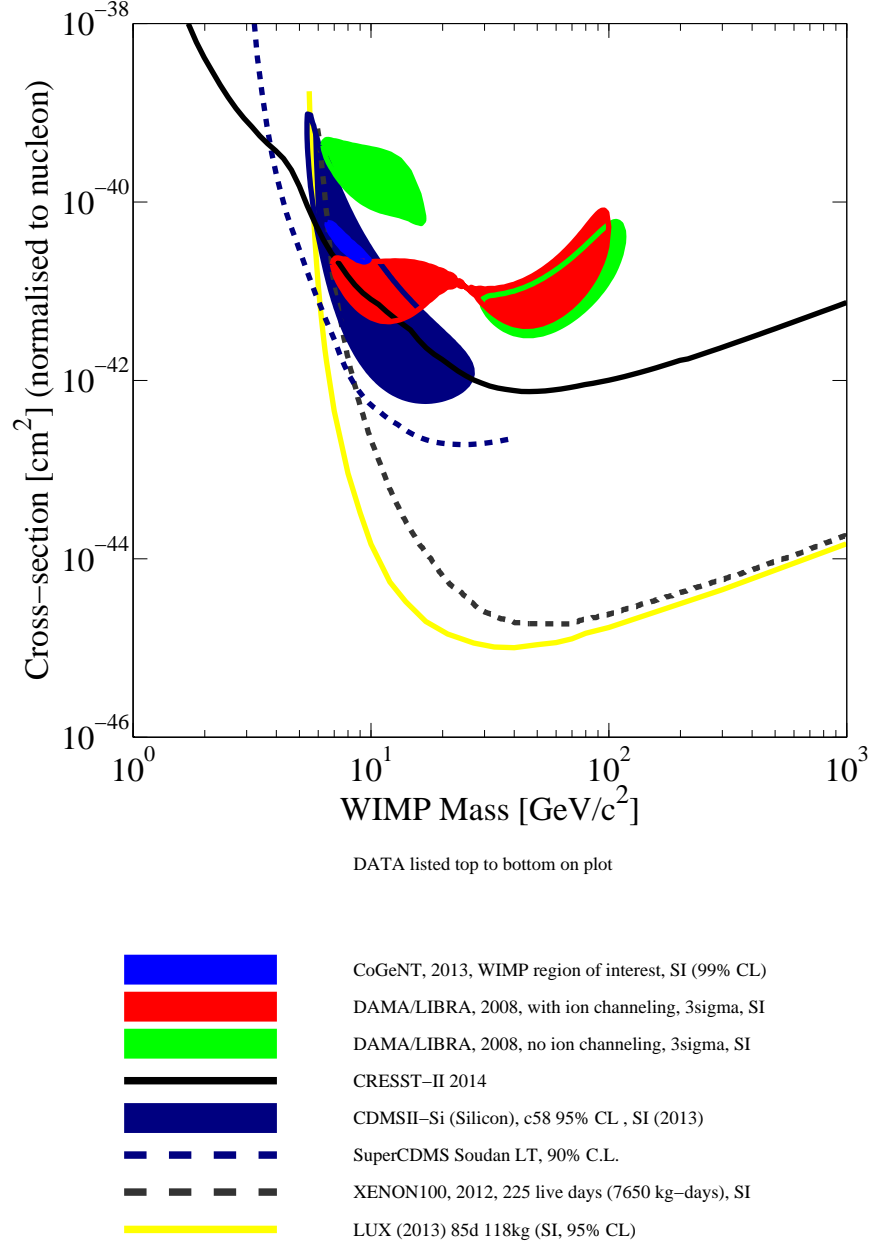|	
🟦	CoGeNT, 2013, WIMP region of interest, SI (99% CL)
🟥	DAMA/LIBRA, 2008, with ion channeling, 3sigma, SI
🟩	DAMA/LIBRA, 2008, no ion channeling, 3sigma, SI
▬	CRESST–II 2014
⬛	CDMSII–Si (Silicon), c58 95% CL , SI (2013)
┅	SuperCDMS Soudan LT, 90% C.L.
┅	XENON100, 2012, 225 live days (7650 kg–days), SI
▬	LUX (2013) 85d 118kg (SI, 95% CL)

Figure 2.7: Current limits (open lines) and allowed regions (filled areas) from various direct DM search experiments in the WIMP mass - WIMP-nucleon cross section (normalized to nucleon) plane assuming the standard neutralino model. Figure generated using [90].

the DAMA/LXe experiment [91], but also liquid neon and liquid argon in the DEAP/CLEAN experiments [92]. Liquid argon is also used in the DarkSide collaboration [93]. Furthermore, argon is also used for the ArDM experiment [94], one ton two-phase liquid argon detector, presently under commissioning underground at Laboratorio Subterráneo de Canfranc. LXe as a target for WIMP detection, on the other hand, has particularly good intrinsic properties, *i.e.* high mass, high scintillation and ionization efficiency and high radiopurity. However, the recoil discrimination achievable is of greater importance. This is realized firstly, as in NaI scintillators, by pulse shape analysis of the scintillation light, which is the basis of single-phase LXe experiments such as XMASS [95] in Japan and UK-based ZEPLIN-I [96]. More powerful discrimination in LXe can be achieved by recording also the ionization produced by the WIMP-nucleus interaction. The recoiling nucleus travels through the target material before stopping, ionizing atoms as it passes. The lower velocities of nuclear recoils, though, induce less ionization relative to the ionization induced by electromagnetic interactions with electrons of the shell by β and γ radiation. This helps to significantly lower the background rate for DM searches. In liquid noble gas detectors this yields to a different ionization/scintillation ratio for nuclear and electron recoils, respectively. This detection principle is implemented using two-phase LXe by the ZEPLIN-II/III [96, 97, 98], the XENON 10/100/1T [99, 100, 101] and the LUX [102] experiments. Hereby, the charge produced by the recoil first drifts out of the liquid into a gaseous phase, where a proportional scintillation signal (electroluminiscence) can be observed. A future experiment that will use the LXe technique is LZ, born from the merging of LUX and ZEPLIN experiences [103].

Another way to detect WIMP-nucleus collisions in a target detector is to search for the ionization signal in a semiconductor, notably in high-purity germanium detectors. These detectors were initially used to look for the Neutrinoless Double Beta Decay of an isotope in the detector itself (see sec.3.3.1). The main problem of those detectors is the large background rate from natural radioactivity. However, very low limits have been achieved by means of careful material selection and detector shielding (GERDA [104], for example). Among the germanium-based experiments, CoGeNT sees an annual modulation signal [105]. The MAJORANA experiment [106], built primarily to search for Neutrinoless Double Beta Decay, will also be made of germanium detectors.

A further possibility to search for the energy deposition by a WIMP-nucleus scattering is the cryogenic or bolometric approach. Whereby the target is cooled to very low temperatures of around 10 mK, so that a 10 keV energy deposit causes a measurable proportional increase in the detector temperature (see next chapter for details). This heating can be measured, *e.g.*, by a superconducting thermometer, which is shifted toward the normal conducting phase by the temperature increase, attached to the target. The initial prospect of detectors of this type was to obtain very low recoil energy thresholds combined with a very high energy resolution. However, it was soon demonstrated that a simultaneous measurement of the ionization signal, together with the heat or phonon signal, also provides a good discrimination against electron recoils. In fact, a recoiling

nucleus produces proportionally less ionization than an electron recoil of the same energy. Experiments using, or that used, the hybrid technique of simultaneous ionization and heat collection are EDELWEISS [107], as well as CDMS II, which had a positive result [108]. This observation is in contrast with the recently released results of its upgrade, the SuperCDMS [109].

As an alternative, the CRESST collaboration has developed $CaWO_4$ cryogenic phonon detectors and pursued the use of scintillation for the second signal channel, next to the heat signal. In particular, instead of using photomultipliers to obtain the scintillation signal, a second phonon-mediated detector with a light absorber is placed adjacent to the primary detector. CRESST also detected a DM signal that, anyway, has been recently ruled out from the collaboation itself [110].

Besides the well established techniques discussed in this section, further approaches to detect DM directly are investigated. One promising technique uses superheated droplet detectors, or "bubble detectors". The goal of these detectors is to detect single bubbles induced by nuclear recoils in heavy liquid bubble chambers. In this implementation of the method, the metastable state of the target liquid is preserved by dispersing it into a viscous/inmiscible gel, effectively resulting in a collection of mini-bubble chambers. The great advantage of this technique, besides the low costs, the room temperature operation and the well known detector technology is the nuclear recoil discrimination power. The energy deposition by an electron recoil is too distributed to cause a bubble to boil, contrary to nuclear recoils. Among the experiments exploiting this technique, there are PICASSO [111] and COUPP [112].

Finally, a powerful, though technologically challenging, possibility to prove that a signal is of galactic origin is to correlate events with the Earth's motion through the galactic WIMP halo. So, the goal is to measure the direction of the recoiling particle and to make use of the diurnal modulation of the signal due to directionality of the "WIMP wind". This is the motivation behind the DMTPC [113], DRIFT [114] and MIMAC [115], time proportional chamber detectors and of the ADAMO project [116], based on $ZnWO_4$ anisotropic scintillating crystals.

Chapter 3

CUORE-0 and the bolometric technique

3.1 Introduction

Among the possible experimental techniques for direct DM detection, the bolometric one is promising. A *bolometer* is a crystal operated as a calorimeter that works at cryogenic temperature ($\sim 10\,\text{mK}$), in which almost all the energy of an interaction is converted into phonons. CUORE-0 is the largest bolometric experiment ever built and is taking data in the underground Laboratori Nazionali del Gran Sasso. It is originally intended for $0\nu\beta\beta$ decay search of ^{130}Te, but it has been demonstrated that a DM study can also be undertaken with this detector [119].

In this chapter the bolometric technique will be described and subsequently a CUORE-0 introduction and summary will be given.

3.2 Bolometers

Generally a detector is sensitive to a single energy release mechanism; consequently only a fraction of the total released energy is detected. Conversely, in a bolometer this does not happen because almost all the deposited energy is converted into thermal phonons that raise its temperature. Thus it is possible to measure this temperature increase by means of a thermometer. Given this, a bolometer can be described as composed of two parts: an *absorber* and a *sensor*. The absorber is a crystal in which an energy release raises the temperature, while the sensor is the thermometer that measures the variation. Then the accumulated heat is dissipated by means of a coupling to a thermal bath (see Fig.3.1).

Given their working principle, bolometers are detectors whose response time develops in tens of ms, making them suitable only for low rate experiments.
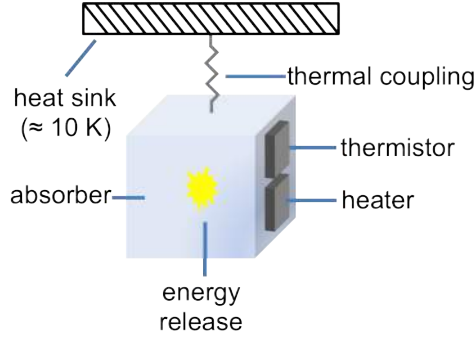
Figure 3.1: Bolometer schema. An interaction with a particle releases energy in the crystal (the absorber), raising its temperature. This temperature variation is measured by means of a thermometer (the thermistor) and then the accumulated heat is dissipated via a coupling to a thermal bath. The heater is an electronic component mainly used for two reasons: to find the working point of the bolometer (see sec.3.2.3) and to correct for pulse amplitude variations due to temperature oscillations (see sec.5.2).

3.2.1 The absorber

The absorber can be sketched as a capacitance C connected to a heat sink via a conductance G. If C is independent from the temperature T, an energy release E causes a temperature variation $\triangle T$ given by:

$$\Delta T = \frac{E}{C}. \tag{3.1}$$

The accumulated heat flows through the conductance to the thermal bath until an equilibrium is reached, following:

$$\Delta T(t) = \frac{E}{C} \cdot e^{-t/\tau}$$

with characteristic time $\tau = C/G$. To have a large and fast signal (temperature variation), the capacitance C must be very small and this is why bolometers work at cryogenic temperatures ($\lesssim 100\,\text{mK}$).

More in detail the specific heat at low temperature of a material is given by two components, one coming from the lattice (c_R) and the other coming from the conduction electrons (c_e) [117]:

$$c(T) = c_R(T) + c_e(T).$$

The $c_R(T)$ part arises from the Debye law [118]

$$c_R(T) = \frac{12\pi^5}{5} N_a k_B \left(\frac{T}{\Theta_D} \right)^3 \tag{3.2}$$

where N_a again is Avogadro's number and k_B and Θ_D are the Boltzmann constant and the Debye temperature of the material, respectively.

The $c_e(T)$ electronic component is described by

$$c_e(T) = \frac{ZR}{\Theta_D}\pi^2\frac{T}{\Theta_F} \tag{3.3}$$

with Z conduction electron number, R gas constant and Θ_F Fermi temperature.

Since $c_R \sim T^3$ and $c_e \sim T$ (from (3.2) and (3.3)) it follows that, to reduce the heat capacitance, it is convenient to choose dielectric and diamagnetic materials, where the contribution of the conduction electrons, dominant at low temperatures, is absent.

3.2.1.1 Intrinsic resolution

In a simplified model, where all the phonons thermalize, it is possible to give an estimate of the energy resolution. In this approximation the energy resolution is limited only by fluctuations of the number of phonons exchanged with the thermal bath. This happens because fluctuations in the number of phonons produce random variations of the energy contained in the absorber. This energy E can be written as

$$E = C(T)T,$$

which, in terms of phonons, is

$$E = N\epsilon$$

where N is the phonon number and $\epsilon = k_BT$ is the phonon average energy. From last two equations it results $N = C(T)T/\epsilon$, and assuming that phonons obey the Poisson law ($\Delta N = \sqrt{N} = \sqrt{C(T)T/\epsilon}$), it is easy to see that the energy fluctuation is described by

$$\Delta E = \Delta N\epsilon = \sqrt{C(T)T\epsilon} = \sqrt{k_BC(T)T^2} \tag{3.4}$$

where the last step is obtained replacing ϵ with k_BT. In (3.4) should be inserted an adimensional parameter to consider the experimental setup, but with a correct realization of the experiment this factor is close to 1. Making calculations with numbers from CUORE-0 ($C \approx 10^{-9}$ J/K and $T = 10$ mK) the resulting resolution is much better than the real one: 10 eV in contrast with the measured $1 \div 2$ keV. This is because the real resolution is dominated by other factors, like electronic noise, microphonism, mechanical vibration of the detector, baseline temperature variation, *etc.*

Particles can interact with the absorber in two ways: via scattering with nuclei or via scattering with electrons; in both cases energy is converted into phonons [120]. In the interaction with the nuclei, the crystal lattice can trap part of the energy in some defects, avoiding its release and worsening the energy resolution. The fraction of total energy lost in this way depends on the particle

nature, being negligible for photons and electrons and of the order of $100\,\text{keV}$ for αs of some MeV.

In the case of electronic channel, the particle creates electron-hole pairs that rapidly propagate through the detector till a quasi-equilibrium state is reached. Once this condition is obtained, phonons are created by means of the interaction of these charge carriers with the lattice. It is possible that part of this energy escapes from the crystal or remains trapped in stable or meta-stable states, turning into a reduction of the energy resolution given that, even if the energy is released, this would happen in a too long time scale to be part of the signal generation.

3.2.2   Thermal sensor

A semiconductor is a material with a small energy gap between the valence band and the conductance band, but in any case too big for an electron to jump to the conduction level, in particular at low temperature. Typical values are of the order of eV, while at room temperature $k_B T \approx 0.026\,\text{eV}$. This gap can be reduced using some doping, which, by introducing intermediate levels between the two bands, allows conduction also at low temperature. If the dopant concentration is high enough, it is possible to obtain a conductor, while with a slightly lower concentration the material is in the metal-insulator transition region (MIT), where the resistance strongly depends on the temperature [121].

In a doped semiconductor at low temperature ($\approx 10\,\text{mK}$) the conduction is dominated by charge carrier migration from one impurity site to another. If the impurities are enough, the wave functions of the charge carriers of nearby impurity atoms are overlapped, so the electrons are no longer localized and are free to jump to different donor sites, without passing through the conduction band. This process, that takes the name of *hopping mechanism* (see Fig.3.2), is possible because electrons can pass from an impurity to another via tunnel effect thanks to the energy of the phonons.

At lower temperatures the energy of the phonon responsible for the mechanism is smaller and the charge carriers migrate on far impurities with free energy levels close to the Fermi energy. In this regime of Variable Range Hopping (VRH) [122] the concentration of minority charge carriers is fundamental because it determines the density of the states near the Fermi level. Therefore it is possible to enter transition region varying mutual concentrations of acceptors and donors.

In VRH regime thermal sensor resistivity highly depends on temperature:

$$\rho(T) = \rho_0 \exp\left(\frac{T_0}{T}\right)^\gamma$$

where ρ_0 and T_0 depend on dopant concentration and $\gamma \simeq 1/2$.

In conclusion for examined thermistors, doped with the *Neutron Transmutation Doped*[1] (NTD) method [123, 124], it is possible to write:

---

[1]This technique consists in thermistors (in the CUORE-0 case germanium parallelepipeds)
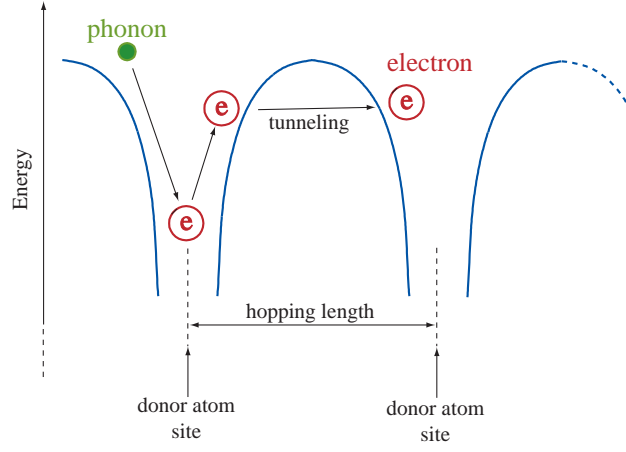
Figure 3.2: Hopping mechanism representation. Electrons can pass from a donor atom site to another; the energy needed for the tunnel effect is provided by phonons.

$$R(T) = R_0 \exp\left(\frac{T_0}{T}\right)^{\gamma}. \tag{3.5}$$

The thermal sensor is a device able to convert a temperature variation into a resistance variation and, by means of a bias current, in an electrical signal. The sensor used is a *Semiconductor Thermistor* (ST), whose working principle relies on its temperature-dependence resistance. These STs are characterized by a sensitivity defined as

$$A = \left|\frac{d \ln R(T)}{d \ln T}\right|$$

and from eq.(3.5) follows that

$$\frac{dR}{R} = A\frac{dT}{T}. \tag{3.6}$$

Typical values of A for STs are ≈ 10, with a response of the order of milliseconds.

3.2.3 Signal generation and readout

To read the sensor resistance variation and thus the signal produced by the event in the detector, a polarization circuit for the thermistor is needed as indicated in Fig.3.3 left.

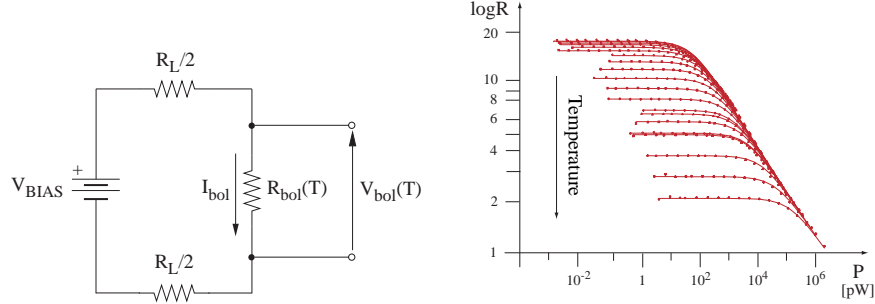
doped by means of thermal neutrons.

Figure 3.3: Left: thermistor polarization circuit for the readout of the signal generated by an event in the detector. Right: dependence of the resistance on dissipated power for different temperature values. Curves with lower resistance at $P \simeq 0$ correspond to higher temperatures.

The thermistor is polarized through a bias current I_{BIAS}, given by a current generator with a voltage V_{BIAS}. The sensor is positioned between two load resistances $R_L/2$, much larger than $R_{bol}(T)$ of the thermistor. In this way the current across the circuit is practically constant independently of $R_{bol}(T)$. So the voltage at the ends of the thermistor is given by:

$$V_{bol} = I_{bol} \cdot R_{bol}(T)$$

with $I_{bol} = I_{BIAS}$. This voltage can produce a power dissipation on the sensor, described by the law $P = V \cdot I$, which causes a resistance diminution (a process known as *electrothermal feedback*). In this case the thermistor no longer presents an "ohmic" behavior. When the power dissipated on the sensor is equal to the one yields to the thermal bath, an equilibrium condition is obtained. Calling the thermal bath temperature T_0, in static conditions the sensor temperature results to be

$$T_{bol} = T_0 + \frac{P}{G}$$

where G is the conductance between the bolometer and the thermal bath. In Fig.3.3 right, dependence of the thermistor resistance on the dissipated power is presented.

The "non-ohmic" behavior described before leads to a non-linearity in the characteristic $I - V$ curve, shown in Fig.3.4. For small values of current the dissipated power is small, thus the temperature rise is negligible and the curve $I - V$ practically has a linear slope. Increasing the voltage the load curve departs from the linear slope until it reaches the inversion point. Over this point a V_{BIAS} increase produces a voltage decrease at the ends of the thermistor. The best working point is the one that optimizes the Signal-to-Noise Ratio
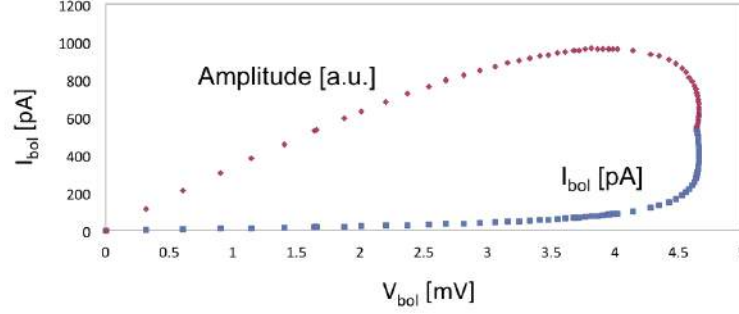
Figure 3.4: Load curve (blue squares) and corresponding signal amplitude (red rhombi) for a bolometer. The load curve shows a "non-ohmic" behavior as V_{BIAS} increases: the slope deviates from linearity until reaches the inversion point, above which any additional increase of V_{BIAS} causes a decrease of the voltage V_{bol} at the ends of the thermistor. The best working point is not the one corresponding to the largest signal amplitude, but the one that optimizes the SNR (obtained with V_{BIAS} above the value that maximizes the signal amplitude).

(SNR), obtained for voltages larger than the one that maximizes the signal amplitude (shown in Fig.3.4). Its search is pursued by first looking for the voltage corresponding to the highest signal amplitude, then rising V_{BIAS} until the maximum is reached in the SNR, since noise decreases faster than the signal. One of the functions of the heater (an electronic component of the detector that releases a constant amount of energy in the bolometer) is to allow a fast search of the working point. Indeed, thanks to the constant intensity of its signal, it is not necessary to build the entire spectrum of the detector, but just to measure the pulse height for any V_{BIAS} applied to the thermistor.

When an interaction releases energy in the crystal there is a consequent temperature rise, which results in a thermistor voltage variation. The produced signal amplitude can be estimated as follows. The thermistor voltage in static condition is given by

$$V_{bol} = V_{BIAS} \frac{R_{bol}}{R_{bol} + R_L}$$

while its voltage variation, due to an energy release E, is described by

$$\Delta V = V_{bol} \frac{\Delta R}{R_L + R_{bol}} \simeq A V_{bol} \frac{\Delta T}{T_{bol}} = A \sqrt{P R_{bol}} \frac{E}{C T_{bol}} \tag{3.7}$$

having used eq.(3.6) in the second step and eq.(3.1) and $V_{bol} = \sqrt{P R_{bol}}$, where P is the power dissipated on the thermistor, in the last one. Eq.(3.7) indicates that signal amplitude goes to zero trivially for $P \to 0$ and $P \to \infty$

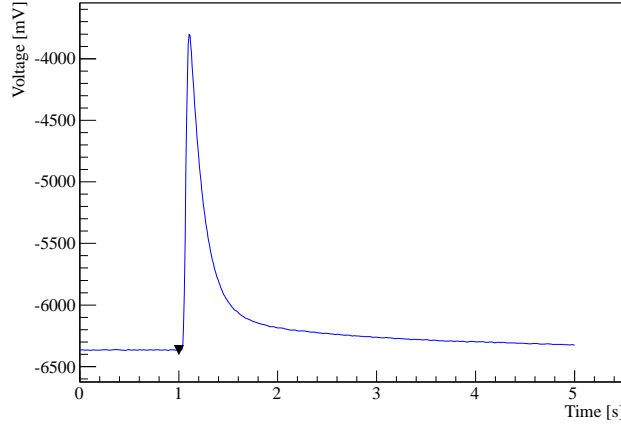Figure 3.5: Typical pulse produced in a bolometer after the energy release by an interaction in the crystal, in this case a $2615\,\mathrm{keV}$ event in a TeO_2 bolometer. The black triangle is the trigger flag and the first second in the acquired window consists of the so-called "pretrigger" points. Thermistor voltage passes through a two-stage amplifier that increases the signal from $\sim 100\,\mu\mathrm{V/MeV}$ up to $\sim 1\,\mathrm{V/MeV}$.

because of the logarithmic sensitivity and the resistance that vanishes at high temperatures.

In Fig.3.5 is shown the typical pulse produced by an interacting particle in a bolometer. Here and in next sections, triangles indicate the trigger flag, in black the one of the considered event, in green the ones of other (preceding or following) triggered events. In addition to the amplitude, two other variables are useful to define the shape of the pulse: the *rise time* and the *decay time*. The first is the time needed to pass from 10% to 90% of the amplitude before the maximum ($\sim 10\,\mathrm{ms}$), while the latter is the time needed to pass from 90% to 30% of the amplitude after the maximum ($\sim 100\,\mathrm{ms}$).

It is possible to evaluate the signal amplitude for an experiment like CUORE-0, where $C \simeq 10^{-9}\,\mathrm{J/K}$ at $10\,\mathrm{mK}$. An event that releases $\approx 1\,\mathrm{MeV}$ of energy in the detector produces a temperature rise of $\sim 0.1\,\mathrm{mK}$ (see eq.(3.1)) and given that $\Delta V/V = A\Delta T/T$, with $V \sim 1\,\mathrm{mV}$ and $A \approx 10$, then $\Delta V \sim 100\,\mu\mathrm{V}$ (subsequently the signal passes a two-stage amplifier that increases its amplitude up to $\sim 1\,\mathrm{V/MeV}$).

3.3 CUORE-0

The CUORE-0 detector is a fundamental step towards the CUORE (Cryogenic Underground Observatory for Rare Events) experiment, the main goal of which
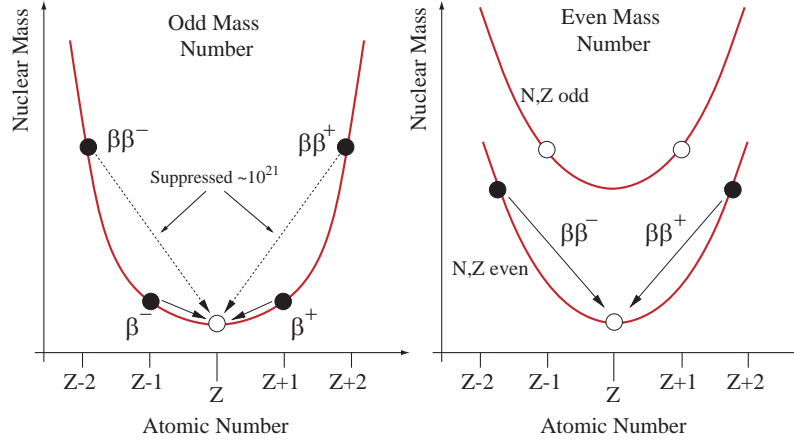
Figure 3.6: Atomic mass as a function of atomic number for odd (left) and even (right) atomic number.

is to search for the neutrinoless double beta decay of ^{130}Te [125, 126]. The detector will consist of 988 $5 \times 5 \times 5\,\text{cm}^3$ TeO$_2$ crystals of 750 g each (for a total mass of 741 kg) grouped in 19 towers, each identical to CUORE-0, which has been built to test the tower assembly line. CUORE will be hosted in a dedicated hut in Hall A of the underground Laboratori Nazionali del Gran Sasso (LNGS) in Italy, under 3650 meters-water-equivalent of rock shielding from cosmic rays. Operations will start in 2015 and data taking will last for 5 years.

First neutrinoless double beta decay will be briefly described and then the CUORE-0 detector and collected statistics will be presented.

3.3.1 Neutrinoless Double Beta Decay

Double beta decay is a very rare process, where the involved nucleus changes its atomic number by two units:

$$(A,Z) \longrightarrow (A,Z \pm 2)$$

In particular, if two neutrons transform into two protons $(Z \to Z + 2)$, it is a negative double beta $(\beta^- \beta^-)$, while if two protons transform in two neutrons $(Z \to Z-2)$ it is a positive double beta $(\beta^+ \beta^+)$. Being a second order process, it has a very small probability to occur and it is possible only when the normal beta decay is forbidden. Even-even nuclei (even number of protons and neutrons) are favorites with respect odd-odd nuclei (odd number of protons and neutrons), because in the former case it is more likely that the starting nucleus (A,Z) is less bounded than the final one $(A,Z \pm 2)$, but more bounded than the intermediate status $(A,Z \pm 1)$, as shown in Fig.3.6.

If two neutrinos are emitted during the decay $(2\nu\beta\beta$, Fig.3.7 left), this is a process allowed by the SM and observed for the first time in 1987 for ^{82}Se [127].
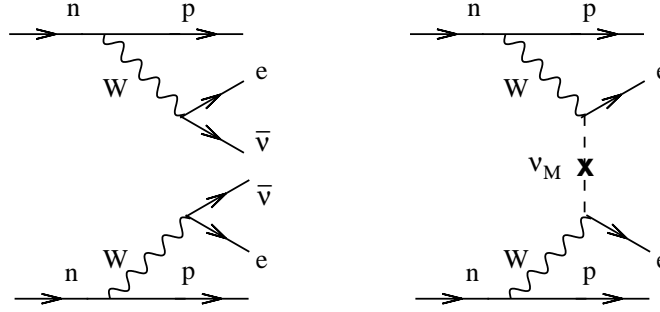
Figure 3.7: Double beta decay diagrams with two neutrino emission ($2\nu\beta\beta$, on the left) and without neutrino emission ($0\nu\beta\beta$, on the right). The latter is possible only by exchange of a Majorana neutrino.
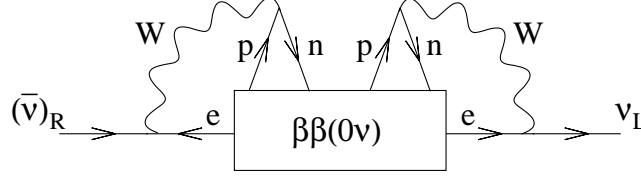

Figure 3.8: A $\bar{\nu}_e$ turns into a ν_e by means of a $0\nu\beta\beta$ interaction. This diagram proves that the eventual existence of the $0\nu\beta\beta$ decay implies the presence of a Majorana mass term for the neutrino.

Nowadays around thirty atoms that decay via $2\nu\beta\beta$ are known, with half-lifes ranging from $\sim 10^{18}$ and $\sim 10^{22}$ years. This process conserves lepton number, is not significantly dependent on the neutrino mass and is not able to discriminate the neutrino nature: Dirac [128] or Majorana [129].

The Majorana model of the neutrino allows a SM forbidden decay: the *neutrinoless double beta decay* ($0\nu\beta\beta$, Fig.3.7 right). This decay can not be realized within the SM because it violates lepton number conservation by two. Such a process requires a Majorana mass component for the neutrino, whichever is the mechanism that generates it [130]. This is shown in Fig.3.8: a mass term allows a chirality flip passing from $\bar{\nu}_e$ to ν_e. This way the antineutrino produced in a vertex becomes a neutrino that can be absorbed in the other interaction vertex, obtaining a $0\nu\beta\beta$ decay.

This decay has never been observed in a convincing way, consequently there are only lower limits on the half-life. At present only about ten isotopes between the possible ones are considered interesting for this study: ^{48}Ca, ^{76}Ge, ^{82}Se, ^{96}Zr, ^{100}Mo, ^{116}Cd, ^{130}Te, ^{136}Xe and ^{150}Nd (for half-life values see [131], and [132] for more updated results on ^{76}Ge and ^{136}Xe).

Figure 3.9: CUORE-0 tower rendering and close up. Left: the 52 $5 \times 5 \times 5\,\mathrm{cm}^3$ TeO$_2$ crystals of 750 g each are set up in 13 floors in groups of 4, for a total mass of 39 kg. The tower skeleton is made of ultra-clean copper and the crystals are plugged to the frames by PTFE clamps. Right: close up of the tower during the assembly; crystals, copper structure and PTFE brackets (white components) are visible.

3.3.2   The detector

A first tower prototype of CUORE, named CUORE-0, is now in the final part of data taking and lasted about 2 years. It is composed of 52 crystals for a total mass of 39 kg of TeO$_2$, and is hosted in the Cuoricino, its predecessor [133], cryostat in Hall A of LNGS. As shown in Fig.3.9, crystals are arranged in 13 floors in groups of 4 and are held to the copper structure (that act also as the heat sink of Fig.3.1) by polytetrafluoroethylene (PTFE) brackets (the weak thermal coupling of Fig.3.1). The typical base temperature of the cryostat is $13 \div 15\,\mathrm{mK}$.

Each crystal is instrumented with a single NTD germanium thermistor for the signal readout and one silicon Joule heater for the offline correction of thermal gain drift, as described in sec.3.2.3, in Fig.3.1 and in [134].

Particular attention was put into the selection and handling of the detector materials with the objective of minimizing the background contamination for CUORE-0. To reduce bulk and surface contamination of crystals during their growth, a radiopurity control protocol was developed in collaboration with the TeO$_2$ crystal producer at the Shanghai Institute of Ceramics, Chinese Academy of Science [135]. Only materials certified for radiopurity were used to grow the crystals. After production, the crystals were transported to LNGS at sea level to limit cosmogenic activation. Once they arrived at the underground laboratory, a small number of them was mounted and operated as a bolometer for quality test. Contaminations from ^{238}U (^{232}Th) decay chain for bulk and surface are less than $6.7 \cdot 10^{-7}\,\mathrm{Bq/kg}$ ($8.4 \cdot 10^{-7}\,\mathrm{Bq/kg}$) and $8.9 \cdot 10^{-9}\,\mathrm{Bq/cm}^2$ ($2.0 \cdot 10^{-9}\,\mathrm{Bq/cm}^2$) at

90% C.L., respectively [136]. Checks of small parts, including NTD thermistors and silicon heaters, indicate that their radioactive content contributes to less than 10% of the total background in the $0\nu\beta\beta$ decay region of interest (ROI).

The Cuoricino experience suggests that the most significant background for the measurement comes from smeared α particles originating in the tower frame and the surrounding cylindrical thermal shield, which deposit only a fraction of their energy in the crystals. All these components are made from radiopure electrolytic tough pitch copper [137]. A different tower geometry with respect Cuoricino allowed a reduction by a factor of 2.3 and 1.8 for total copper mass and surface area, respectively. Monte Carlo simulations predict a factor of 1.3 decrease in α background from the thermal shield arriving at the crystals due to the change in the disposal [138]. In addition, different surface treatments were tested to further reduce the copper contaminations [139]. Among them a series of tumbling, electropolishing, chemical etching, and magnetron plasma etching for the surface treatment was selected. After these processes the measured surface contaminations are $1.3 \cdot 10^{-7}$ Bq/cm^2 90% C.L. for ^{238}U and ^{232}Th [139].

The CUORE-0 detector assembly procedure was designed to minimize the recontamination of clean components. Tower mounting took place in a dedicated class 1000 clean room in Hall A of the LNGS underground facility. To reduce exposure of components to radon (and its progeny), all the assembly was performed under nitrogen atmosphere inside glove boxes [140]. All the tools inside the glove boxes, in particular those that touched the tower components, were cleaned and certified for radiopurity. Then, as already said, the completed tower was enclosed in copper thermal shield and then inserted in the Cuoricino cryostat. To minimize exposure to the environment during this operation, mounting was performed in the Cuoricino clean room, and the tower was kept under nitrogen flux for as long as possible.

CUORE-0 uses for the first time flexible printed circuit board (PCB) cables and *in situ* wire bonding for electrical wiring of the tower. This is one of the major upgrades that significantly improved the robustness of bolometer readout wiring, compared to the Cuoricino design. A series of flexible PCB cables with copper traces [141, 142] was attached to the copper frame from the bottom plane to the top. The lower ends of these cables were bonded to the metal pads of thermistors and heaters with $25\,\mu$m diameter gold wires. The upper ends were connected through flexible PCB at the $10\,$mK plate to a set of Manganin twisted pair flat ribbon cables running un-interrupted to the feedthroughs on the top plate of the cryostat. If on one side PCB cables, of course, improve the robustness and reproducibility of the assembly, on the other side they could potentially affect the noise and thermal behavior of the array. In any case the negative effects are under control and possible means to mitigate them have been identified. Overall, only 3 bolometers (6%) are not fully functional from the loss of one thermistor and two heaters. The two heater-less bolometers (namely channel 1 and 10) can be used in non-standard analysis with thermal gain correction based on the model presented in [143], but anyhow they will not be taken into account in the work presented in this thesis.

CUORE-0 is operated in the same cryostat, uses the same external lead and

borated-polyethylene neutron shielding, and is enclosed in the same Faraday cage that was used for Cuoricino. The front-end electronics [144, 145, 146] and data acquisition hardware are also identical to those used in Cuoricino. A new algorithm is implemented to automate the search for the correct working point (see sec.3.2.3), which scans different voltages until the best SNR is obtained for every single channel. Bolometer signals are amplified and filtered with a six-pole Bessel low pass filters. Subsequently, signals are digitized by two 32-channel National Instruments PXI analog-to-digital converters with a $125 \, \mathrm{S/s}$ sampling rate, 18-bit resolution, and $21 \, \mathrm{V}$ full scale. All samples are both triggered and stored continuously on disk, in such a way that data can be retriggered and reprocessed offline, eventually with a different trigger. During triggering (in real time or during reprocessing) for every trigger a window of 626 sampling points ($5.008 \, \mathrm{s}$), including a pretrigger segment of 125 samples, is saved, as indicated in Fig.3.5. Each bolometer has an independent trigger threshold. As explained in sec.3.2.3 one of the function of the heater is to stabilize the amplitude variation due to temperature instability of the cryostat. To this end, every $300 \, \mathrm{s}$ a pulse of constant energy is released from the heater (also called pulser for this reason) and the detector is triggered by that pulse. Finally, a baseline trigger identifies a baseline pulse every $300 \, \mathrm{s}$ to provide snapshots of the detector working temperatures and noise spectra.

CUORE-0 data taking is subdivided into "datasets". Each dataset consists of a series of initial calibration runs, some background runs and a set of final calibration runs. Calibration runs are done to calibrate the channel spectra using known energy peaks from $^{232}\mathrm{Th}$ decay chain, with energies ranging from 511 to $2615 \, \mathrm{keV}$. The source consists of two thoriated tungsten wires with activities of $50 \, \mathrm{Bq}$ each and is positioned in two vertical tubes on opposite sides of the tower that run between the outer vacuum chamber and the external lead shielding. Background refers to data acquired without calibration sources. These data are good for physics analysis such as DM and $0\nu\beta\beta$ decay search; generally a background run lasts $24 \, \mathrm{h}$. The signal rates on each bolometer for the calibration and background data acquired with the standard trigger are $60 \div 70$ and $0.5 \div 1.0 \, \mathrm{mHz}$, respectively.

3.3.3 Collected statistics

CUORE-0 started to take data in March 2013 and had some interruptions for cryostat maintenance. In Fig.3.10 is shown the duty cycle from the beginning up to March 2015. As can be seen, there is a large stop from the end of August 2013 to the second half of November 2013, for an important cryostat maintenance, after which baseline and peak resolutions improved considerably. In fact, dividing acquired data into these two phases and considering single channels, the median noise FWHM at the baseline in background runs before and after the long cryostat maintenance are 3.9 and $2.6 \, \mathrm{keV}$, respectively. For this reason in this thesis only data from November 2013 on will be considered. The list of used datasets with relative start and stop time is in Tab.3.1.

When acquired data quality is low it is possible to set "bad intervals", mean-
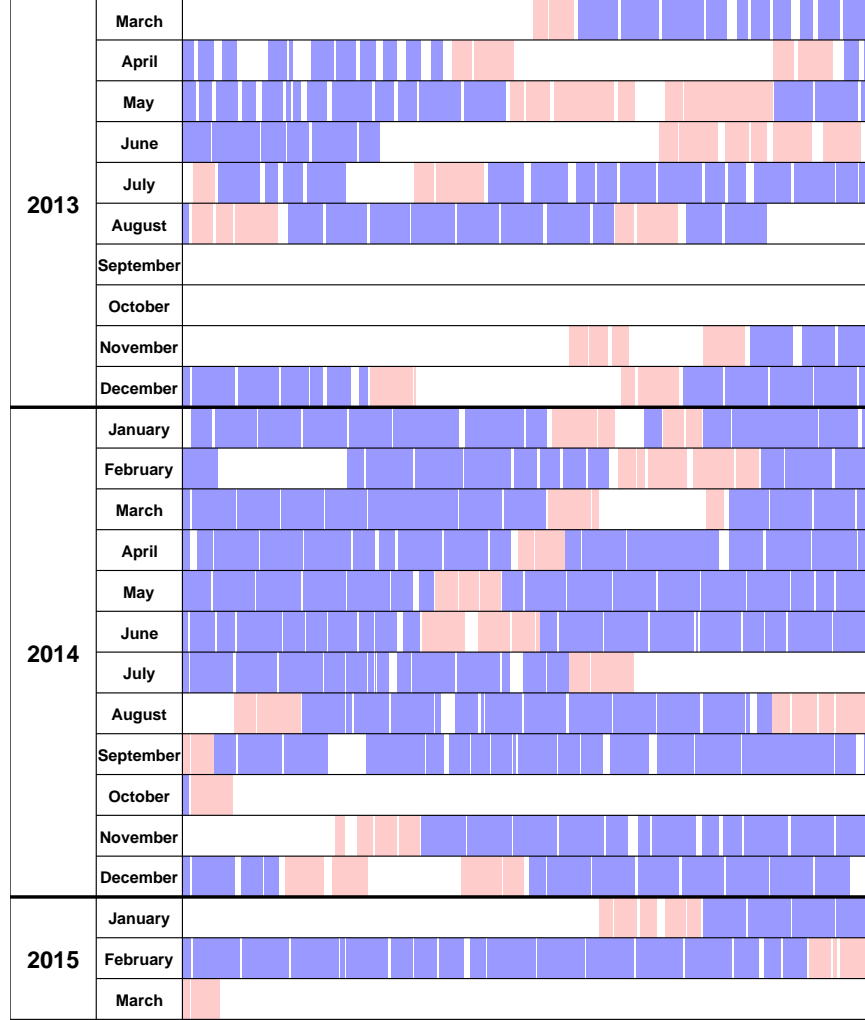
Figure 3.10:   CUORE-0 duty cycle. Data taking started in March 2013 and ended in March 2015. Blue indicates background runs, while red indicates calibration runs. In the period August-September 2013 a large cryostat maintenance operation took place, after which baseline and peak resolutions improved substantially. In this thesis only data taken after this operation is used for the analysis.

Dataset	Start Time UTC	Stop Time UTC	Background [d]	Calibration [d]
2079	13-11-17 20:41	13-12-11 13:05	8.72	2.68
2085	13-12-20 18:03	14-01-20 11:46	23.22	5.12
2088	14-01-17 16:56	14-02-24 10:57	18.03	9.26
2091	14-02-18 17:40	14-03-19 18:24	19.40	7.14
2097	14-03-24 14:55	14-04-17 17:30	18.04	2.71
2100	14-04-15 17:07	14-05-15 09:30	21.24	4.62
2103	14-05-12 11:01	14-06-13 08:17	22.77	4.38
2109	14-06-13 23:00	14-07-21 09:24	27.48	5.09
2124	14-08-29 17:32	14-10-03 08:30	23.21	5.00
2130	14-11-07 16:48	14-12-09 09:10	17.49	4.69
2139	15-01-19 18:36	15-03-02 17:23	18.97	4.48

Table 3.1: List of datasets used in this analysis with their start and stop times. Start Time and Stop Time for each dataset are the start and the stop time of the first and of the last calibration run, respectively. Background and calibration indicates the average live time for each dataset of this kind of run. In this second phase of the experiment there are two additional datasets (2118 and 2133) that are not taken into account since they closed unexpectedly without a n-pulsers measurement (see sec.4.4).

ing that these intervals are not good for the analysis. Interval selection is performed channel-by-channel by looking at baseline resolution, baseline stability, noise during run, electronic problems and in general everything that worsens the measure. Consequently the total exposure is given by the sum of single channel live times. The accumulated exposure is $35.2 \, \text{kg} \cdot \text{y}$ (corresponding to $9.8 \, \text{kg} \cdot \text{y}$ of ^{130}Te isotopic exposure, considering 51 channels and removing bad intervals). The energy calibration is performed with a second order polynomial fit in the energy range $0 \div 2.6 \, \text{MeV}$, to account for a small non-linearity that leads to a $10 \, \text{keV}$ discrepancy at the $2615 \, \text{keV}$ peak. If, applying the initial calibration coefficients to the final calibration spectrum, the $2.6 \, \text{MeV}$ peak position is shifted from nominal value more than a FWHM, initial and final calibration are considered incompatibles and a bad interval is set all along the dataset for that channel.

To select $0\nu\beta\beta$ candidate events some cuts are applied to the data:

- All the bad intervals are discarded, for a 7% of total exposure reduction.

- To allow a bolometer time to equilibrate after each event (pileup rejection) it is required that the times since the previous event and until the next event on the same bolometer are greater than $3.1 \, \text{s}$ and $4.0 \, \text{s}$, respectively.

- To reject noisy pulses, which can contribute to background, six pulse-shape parameters are taken into account, constructed for each channel/dataset pair. These parameters are tuned simultaneously on a set of peaks in the

> background data to maximize the signal sensitivity at each peak, defined as the the ratio of signal accepted to square root of the background accepted, where the signal sample is drawn from events that populate each peak and the background is drawn from nearby off-peak events. For a more detailed explanations of the the event selection and the quality cuts done in the $0\nu\beta\beta$ decay ROI look at [148].

- to reduce background from radiation that deposits energy in multiple crystals, such as α decays at crystal surfaces or multiple Compton scattering, an event is rejected if there is another event in the tower within $\pm 5\,\mathrm{ms}$ (anti-coincidence).

In the $0\nu\beta\beta$ decay ROI the pileup and pulse-shape cuts efficiency correspond to $93.7\pm0.7\%$ [149], and is estimated from the fraction of $2615k\,\mathrm{keV}$ ^{208}Tl events in background data that pass this selection. The anti-coincidence cut is composed of two parts: the probability that the $0\nu\beta\beta$ decay electrons are fully contained in a single crystal and probability that a candidate event will not be rejected due to an accidental coincidence. Geant4 simulations showed that the former is $88.40 \pm 0.09\%$, while the latter corresponds to $99.64 \pm 0.10\%$ [149]. Considering the $98.529 \pm 0.004\%$ trigger efficiency, measured on pulser events near the ROI (using the Derivative Trigger, see next chapter), the total detection efficiency of CUORE-0 in the $0\nu\beta\beta$ decay region is $81.3 \pm 0.6\%$ [149]. This result is close to the one obtained for Cuoricino: $82.8 \pm 1.1\%$ [133].

One of the greatest results obtained by CUORE-0 is the reduction of the background counts due to contaminations. As can be seen in Fig.3.11, where a comparison of the two spectra is shown in the range $300 \div 7500\,\mathrm{keV}$, the CUORE-0 spectrum is lower than the Cuoricino spectrum at all energies. In particular, ^{238}U γ lines are reduced by a factor of 2 due to better radon control, ^{238}U and ^{232}Th α lines are reduced thanks to the new detector surface treatment, while ^{232}Th γ lines are not reduced since they originate in the cryostat (the CUORE one is designed to decrease this effect).

More precisely in the $0\nu\beta\beta$ decay ROI the background rate is equal to $0.058\pm 0.004\,(\mathrm{stat.}) \pm 0.002\,(\mathrm{syst.})\,\mathrm{counts/keV/kg/y}$ in CUORE-0 [149] and $0.153 \pm 0.006\,\mathrm{counts/keV/kg/y}$ in Cuoricino crystals with dimensions of $5 \times 5 \times 5\,\mathrm{cm}^3$, while for the whole detector it is $0.169 \pm 0.006\,\mathrm{counts/keV/kg/y}$ [133]. The reduction of the α background is evaluated in the region that goes from 2.7 to $3.9\,\mathrm{MeV}$ excluding the ^{190}Pt peak in the range $3.1 \div 3.4\,\mathrm{MeV}$. In this interval, the so-called α flat continuum region, CUORE-0 reached a background rate of $0.016 \pm 0.001\,\mathrm{counts/keV/kg/y}$ [150], which is almost 6 times smaller than the Cuoricino result of $0.110 \pm 0.001\,\mathrm{counts/keV/kg/y}$ [148].

These encouraging results imply that the more rigorous copper surface treatment, the improved crystal production and treatment protocols, and the more stringent assembly procedures in the clean environment have been extremely effective in the background reduction aim. Thanks to this, CUORE-0 reached a $0\nu\beta\beta$ median lower-limit sensitivity of $2.9 \cdot 10^{24}\,\mathrm{y}$ at 90% C.L. and a Bayesian lower bound on the decay half-life, $T^{0\nu}_{1/2} > 2.7 \cdot 10^{24}\,\mathrm{y}$ at 90% C.L. [149].
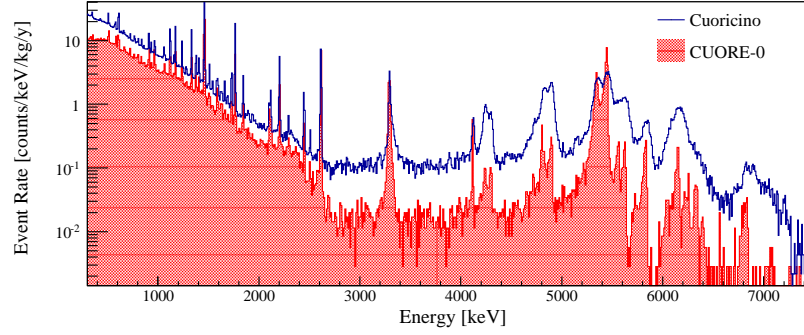
Figure 3.11: CUORE-0 (red shaded) and Cuoricino (black) background spectra comparison. The improvements in CUORE-0 are evident along all the energy interval that goes from 300 to 7500 keV: ^{238}U γ lines reduced by a factor 2 (better radon control), ^{232}Th γ lines not reduced (originated from the cryostat); ^{238}U and ^{232}Th α lines reduced thanks to the new detector surface treatment.

By means of its larger array, which allows a more powerful time coincidence analysis and a more effective self-shielding from external backgrounds, CUORE will be able to reach the background goal of 0.01 counts/keV/kg/y, which corresponds to a 90% C.L. sensitivity of $9.5 \cdot 10^{25}$ y for 5 years of live time [151].

Chapter 4

Optimum Trigger: the low energy trigger

4.1 Introduction

In order to be able to observe a DM interaction in CUORE-0, a low energy trigger is needed. In fact, the standard trigger used in CUORE-0, the Derivative Trigger (DT), has an extremely small detection probability an event below 30 keV. Given the very low event rate and sampling frequency it is possible to use a trigger which is software generated. Using a trigger and a pulse shape algorithm based on the matched filter technique [152], which removes the non physical pulses, it has been demonstrated that is possible to push the energy threshold down to a few keV [153]. Such trigger, named Optimum Trigger (OT), uses a transfer function that maximizes the SNR and is applied to the data flow coming from the detector.

The following sections describe the Optimum Trigger, its implementation and efficiency, starting from the the algorithm on which it is based.

4.2 Optimum Filter

The Optimum Filter (OF) is the algorithm that the OT is based on. This filter evaluates the amplitude of a pulse maximizing the SNR. It is based on the assumption that a detector waveform $y(t)$ can be written as:

$$y(t) = A \cdot s(t) + n(t) \tag{4.1}$$

where $s(t)$ is the known signal time evolution (its shape), A the signal amplitude and $n(t)$ the detector noise, which is stationary. The first term indicates that the signal shape is independent from the amplitude and thus from the event

energy[1]. The last assumption is that the noise has a known power spectrum, defined by:

$$N(\omega) = \langle n(\omega)n(\omega^*) \rangle$$

where $n(\omega)$ is the Fourier transform of $n(t)$ and $\langle \rangle$ denotes the expectation value over a large number of noise waveforms. Given that the filter works on sampled data, the eq.(4.1) can be re-written as:

$$y_i = A \cdot s_i + n_i \tag{4.2}$$

where i is the sample index.

Now the formalism of the filter will be derived, first for the case of white noise and then in general for any type of noise.

4.2.1 White noise case

White noise is noise with a time-independent Gaussian distribution. The filter is supposed to maximize the likelihood as a function of the displacement j between the template s and the signal in y. The likelihood is given by:

$$L_j(y_i|A_j) = \prod_i \frac{1}{\sqrt{2\pi}\sigma} \exp\left[-\frac{(y_i - A_j s_{i-j})^2}{2\sigma^2}\right] \tag{4.3}$$

where σ is the noise RMS and the product extends over the length of y_i. In the numerator of the exponential is present a $-j$ in the subscript of s since the assumption is that the registered signal is not only scaled (property described by A_j), but also shifted from the known one. So, for each shift j, one can impose:

$$\frac{d}{dA_j} L_j(y_i|A_j) \propto \sum_i (y_i - A_j s_{i-j})s_{i-j} = 0.$$

The solution $\hat{A}_j$ for the amplitude is

$$\hat{A}_j = \frac{\sum_i y_i s_{i-j}}{\sum_i s_{i-j}^2}. \tag{4.4}$$

To evaluate the delay j it is possible to take the numerator of eq.(4.3), $\sum_i (y_i - A_j s_{i-j})^2$, and substitute the solution just found for A_j. Before doing this, it is useful to expand the square, that must be minimized:

$$\sum_i (f_i + n_i)^2 + A_j^2 \sum_i s_{i-j}^2 - 2A_j \sum_i f_i s_{i-j} - 2A_j \sum_i n_i s_{i-j}. \tag{4.5}$$

---

[1]This approximation introduces a systematic error that varies with energy from per mille to per cent. Anyhow the calibration function with its non-linearity removes this error.

where we used the eq.(4.2) and for simplicity $y_i = f_i + n_i$ (meaning that $f_i = A_j \cdot s_{i-j}$). The first and the last terms can be removed since they have no influence on the result, given that they are constants: the first because the measured signal is given and the last because the noise is uncorrelated and with 0 means. Now, changing the signs, the sum to maximize is:

$$2A_j \sum_i f_i s_{i-j} - A_j^2 \sum_i s_{i-j}^2 = A_j^2 \sum_i s_{i-j}^2,$$

that, replacing A_j, becomes

$$\frac{\left(\sum_i y_i s_{i-j}\right)^2}{\sum_i s_{i-j}^2}.$$

Using the Cauchy-Swartz inequality, it results

$$\left(\sum_i y_i s_{i-j}\right)^2 \leq \sum_i y_i^2 \cdot \sum_i s_{i-j}^2.$$

The equality sign is possible only if $s_{i-j} = c y_i$, with c numerical constant. So the maximum position for the filtered pulse is obtained for $j = 0$, and the filtered signal will be shifted by $-i_M$, where i_M is the maximum position of the template.

Coming back to eq.(4.4) it is possible to rewrite it, the filtered amplitude y_i', as a convolution of the "kernel" K_i of the filter and the original waveform y_i:

$$y_i' = y_i \otimes K_i \tag{4.6}$$

$$K_i = \frac{s_{-i}}{\sum_l s_l^2}.$$

The filter leaves the pulse amplitude unmodified, while the noise RMS is reduced to

$$\sigma'^2 = \frac{\sigma^2}{\sum_l s_l^2}. \tag{4.7}$$

To align the maxima of the two signals the kernel can be shifted by $-i_M$. In the frequency domain eq.(4.6) can be written as:

$$y'(\omega_k) = y(\omega_k) \cdot K(\omega_k) \tag{4.8}$$

that becomes

$$y'(\omega_k) = y(\omega_k) \cdot K(\omega_k) e^{-j\omega i_M}$$

including the delay of the filtered maximum.

From this equation it is possible to obtain the filter transfer function:

$$H(\omega_k) = K(\omega_k)e^{-j\omega i_M} = \frac{1}{E_s}s^*(\omega_k)e^{-j\omega i_M} \tag{4.9}$$

where E_s is the signal energy, defined as $E_s = \sum_l s_l^2$.

4.2.2 General noise case

When the noise is correlated, the elements of the product in eq.(4.3) are no longer independent. This means that the filter in eq.(4.9) cannot be used as-is. Applying a "whitening" filter like

$$W(\omega_k) = \frac{1}{n(\omega_k)}$$

to the noise it is possible to use the equations presented in the previous section. This filter has to be applied to the combination signal + noise (*i.e.* to y_i), so the signal shape is modified into $s(\omega_k)/n(\omega_k)$ and the transfer function becomes

$$H(\omega_k) = h\frac{s^*(\omega_k)}{n^*(\omega_k)}e^{-j\omega i_M}\frac{1}{n(\omega_k)} = h\frac{s^*(\omega_k)}{N(\omega_k)}e^{-j\omega i_M} \tag{4.10}$$

where h is a normalization constant that leaves unmodified the signal amplitude after the filter:

$$h = 1/\sum_k \frac{|s(\omega_k)|^2}{N(\omega_k)}.$$

The new noise power spectrum is

$$N'(\omega_k) = h^2\frac{|s(\omega_k)|^2}{N(\omega_k)}$$

and the new noise RMS is

$$\sigma'^2 = \sum_k N'(\omega_k) = h. \tag{4.11}$$

In the case of white noise, the input power spectrum is given by

$$N(\omega_k) = M\sigma^2$$

where M is the window length. In this case eq.(4.11) reduces to

$$\sigma'^2 = \sigma^2\frac{M}{\sum_k |s(\omega_k)|^2},$$

which, using the Parseval identity, can be demonstrated to be equal to eq.(4.7).

4.2.3   Filter transfer function

Going from eq.(4.6) to eq.(4.8), and then to eq.(4.10), the discrete convolution theorem has been implicitly used [154]. In fact the theorem says that if a signal s_i is periodic with period M, then its discrete convolution with a kernel H_i of finite duration M is a member of the discrete transform pair:

$$\sum_{j=0}^{M-1} s_{i-j} H_j \Longleftrightarrow s(\omega_k) \cdot H(\omega_k).$$

To apply this theorem the two conditions in the hypothesis must be fulfilled: The kernel and the signal must have the same duration and the signal must be periodic. The first condition is simple, it only requires to add some zeros to the kernel until it reaches the signal length. The second condition is needed because the Discrete Fourier Transform (DFT) works on periodic windows of finite length. This is because the DFT frequency spectrum is the spectrum of an infinite repetition of the input window. If the input data are not periodic the filter will pollute the right side of the filtered signal with the left part of the original sampled data (and vice versa); problem known as DFT convolution wraparound [155]. This way the only part of unspoiled signal is the one that corresponds to the zeros of the kernel (see Fig.4.1).

To accomplish the hypothesis, the transfer function has been built following these steps:

1. build the OF transfer function $H(\omega_k)$ of length M using the template of the signal s_i and the noise power spectrum $N(\omega_k)$, both of length M;

2. transform $H(\omega_k)$ in the time domain by means of DFT, obtaining the kernel H_i of length M;

3. insert M zeros in the middle of H_i, obtaining the new kernel H_i^d of length $2M$;

4. smooth H_i^d in proximity of the zeros to get the new smoothed kernel H_i^{ds};

5. transform H_i^{ds} into the frequency domain, obtaining the $H_i^{ds}(\omega_k)$, of length $2M$.

The fourth point is needed to avoid the Gibbs phenomenon [156]: if H_i^d does not approach zero in the central part of the kernel, where zeros are, a discontinuity will be created in the filtered signal, introducing fake oscillations in the DFT. This means that only the central part of length M of the filtered samples will be correctly filtered, the first and the last $M/2$ points will be spoiled, as described in Fig.4.1. In CUORE-0 the smoothing is done using the cosine function. In particular the quarter-period that goes from one to zero for the first $M/2$ samples and the quarter-period that goes from zero to one for the last $M/2$ points are used.
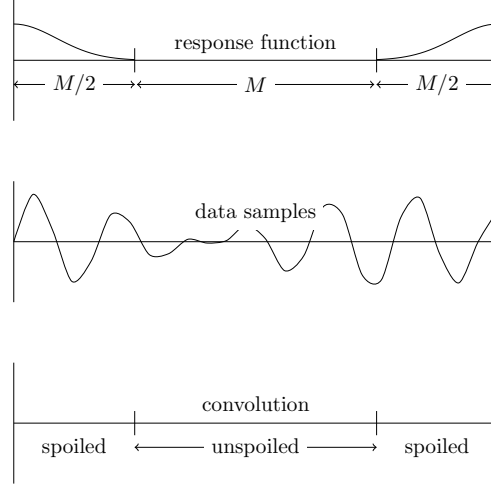
Figure 4.1: The filter kernel is composed by a central part made up of zeros and two external bands. The central part, of length M, equal to the length of the signal to be filtered, correctly transforms the data samples. In the outer parts, each of length $M/2$, the data samples are spoiled when filtered (the left side with data from the right side and vice versa).
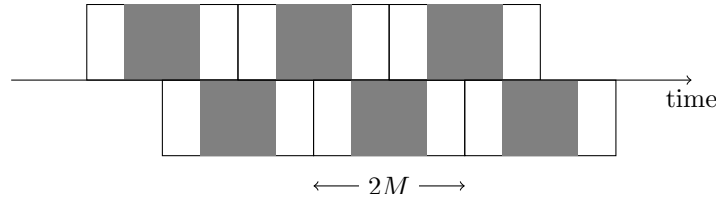

Figure 4.2: The data flow is divided into concatenated windows, each of length $2M$. The overlapping is needed to bypass the Gibbs problem: only the central (gray) part is correctly filtered, while the external (white) ones are not. The central part is of length M, while both the external bands $M/2$.
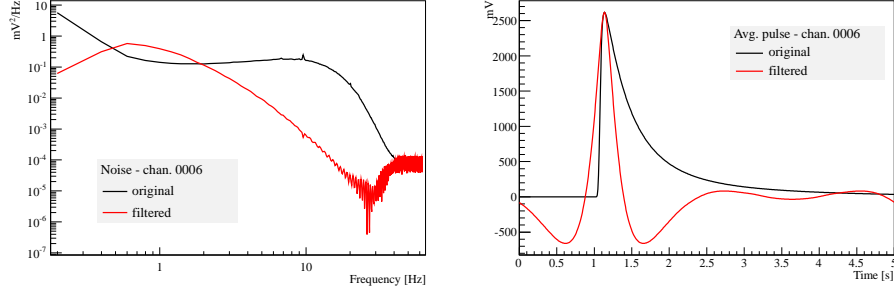
Figure 4.3: Average noise power spectrum (left) and average pulse (right), original in black and filtered in red, of channel 6 in dataset 2088. As can be seen the filtered average pulse shows a quasi-symmetric shape and a zero baseline (the original pulse is moved to have zero baseline for an easier comparison with the filtered one). The acquisition windows are 626 samples long, corresponding to 5.008 s. Since the window length is not doubled, only its central part is correctly filtered.

To filter all the data flow from the detector correctly, concatenated windows of length $2M$ should be taken, where the overlap is equal to $M/2$ with the preceding and following windows, as indicated in Fig.4.2.

In practice the filter is implemented using the the average pulse of a channel as s_i and the average noise power spectrum of the same channel as $N(\omega_k)$. As described, the cosine has been selected as smoothing function, so the first half of the filter can be written as:

$$H_i^{ds} = H_i^d \quad , \quad i < \frac{M}{2} - L$$

$$H_i^{ds} = \frac{H_i^d}{2} \left\{ 1 + \cos \left(\frac{\pi}{L} \left[i + 1 - \left(\frac{M}{2} - L \right) \right] \right) \right\} \quad , \quad \frac{M}{2} - L \leq i < \frac{M}{2}$$

$$H_i^{ds} = H_i^d = 0 \quad , \quad \frac{M}{2} \leq i < M$$

where L is the cosine half-period. The second half is identical to the first, but mirrored. Once H_i^{ds} has been calculated, the transfer function in the frequency domain $H(\omega_k)$ can be applied to the data. In Fig.4.3 are shown the average noise power spectrum on the left and the average pulse on the right, original (black) and filtered (red), of channel 6 in dataset 2088. Looking at the second image it is evident that the filtered pulse presents an almost symmetric shape and a zero baseline.
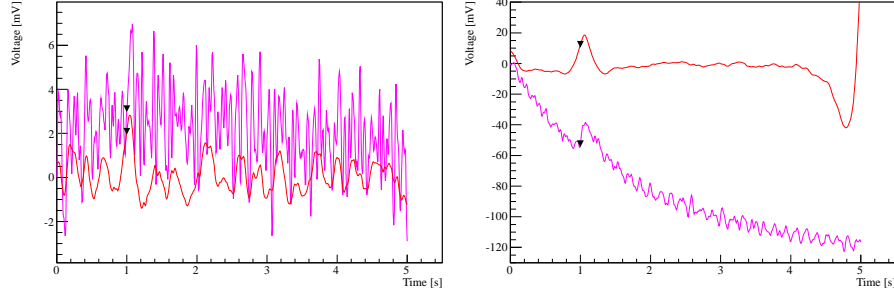
Figure 4.4: A 4 keV (left) and a 18 keV (right) events triggered with the OT, original pulses in blue, OF filtered ones in red. In both cases it is possible to see that filtered samples are less noisy: baseline oscillations are smaller and frequencies that do not belong to the signal are suppressed, like the baseline slope in the image on the right. It shows also the Gibbs problem, recognizable in the steep slope at the very end of the filtered pulse. Triangles indicate the trigger position.

4.3   Optimum Trigger

As mentioned in sec.3.3.2, the continuous data flow from the detector is saved on disk, in such a way that it can be reanalyzed offline. Reprocessing it with the OT, the data flow is divided into concatenated windows, as shown in Fig.4.2, where the trigger can fire only in the central part. The name Optimum Trigger comes from the fact that trigger works on samples filtered with the Optimum Filter.

Looking at data filtered with the OF in Fig.4.4 it is evident that:

- noise fluctuations are reduced;

- the baseline has zero mean;

- the filter is sensitive to the signal shape, suppressing pulses with a shape different from the expected one.

All of this allows to lower the energy threshold with respect to a trigger that works with non-filtered data.

The OT fires when pulse height exceed a threshold and a local maximum is found within a FWHM of the filtered ideal pulse (the average pulse). The threshold is channel-dependent, and is set equal to a given number of sigma n_σ of filtered noise σ_{OF}, which is known *a priori* (eq.(4.11)). Data presented here are triggered with $n_\sigma = 3$, meaning that the threshold is equal to $3 \times \sigma_{OF}$. Once the trigger fires, it will be possible to set a new trigger flag only after a FWHM of the filtered ideal pulse. The trigger position is then shifted back by a fixed number of samples, equal to the time that elapses between the middle of the rise and the maximum of the non-filtered average pulse. This is because during
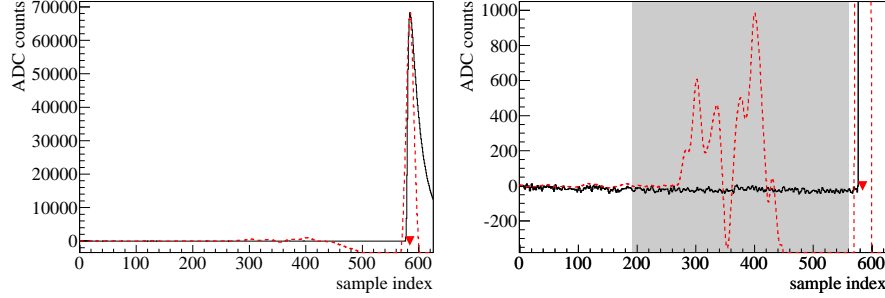
Figure 4.5: Left: a high energy pulse (5.4 MeV) is triggered. Right: side lobes of the filtered pulse can exceed the trigger threshold. To avoid triggering on these fake pulses, in the old version of the trigger a veto region was set (gray band): in this region it was not possible for the trigger to fire. In both images black continuum line for the original pulse, red dashed line for the filtered one.

data analysis the trigger flag is expected to be before the pulse maximum. In all figures with triggered pulses (as in Fig.4.4) the triangles represent the trigger position.

When a high energy event occurs (and is triggered), its filtered samples may present a set of side pulses due to effects of the OF. These fake pulses can exceed the threshold and make the trigger fire again. In the old version of the OT this problem was solved by putting a veto region on the sides of the primary pulse, where it is not possible to set a trigger (see Fig.4.5). Clearly the veto becomes an important source of inefficiency, in particular when contaminations with high energy peaks are present (like ^{210}Po or ^{210}Pb), since their high rates produce a lot of dead time.

In the new version of the trigger, no veto is applied. Side pulses are not triggered by checking that, in the vicinity of them, there is no higher pulse that can generate them as side lobes. This evaluation is based on the filtered average pulse shape, since the number and the distance of side lobes change channel-by-channel. An example of this is in Fig.4.6, which shows what the trigger sees: the gray bands are the regions where is not possible to make the trigger fire and the horizontal red line is the threshold. A high energy pulse is present in the window and it is evident that two side lobes per side exceed the threshold, but nevertheless they are not triggered.

Another new OT feature is that it no longer trigger on negative pulses anymore (example given in Fig.4.7). They are produced by electronics or temperature variations. The simplest way to understand why they may make the trigger fire is to look at a normal pulse, as in Fig.4.6, and imagine to turn it upside down. At this point the lower oscillations, introduced by the OF, that now are on the top, can be high enough to exceed the threshold. To avoid this, a similar check to the one done for the side lobes is performed, which controls that the event has not been generated by the filtering of a negative pulse.
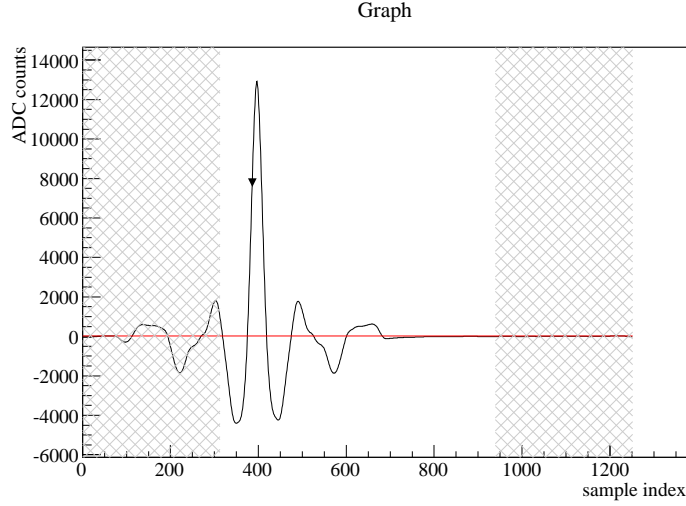
Figure 4.6: Trigger window with a high energy pulse. The gray bands are the regions where it is not possible to set a trigger, while the red horizontal line represents the threshold. As can be seen on the sides of the pulse there are lobes higher than the threshold, that anyway are not triggered thanks to the new implementations of the OT.
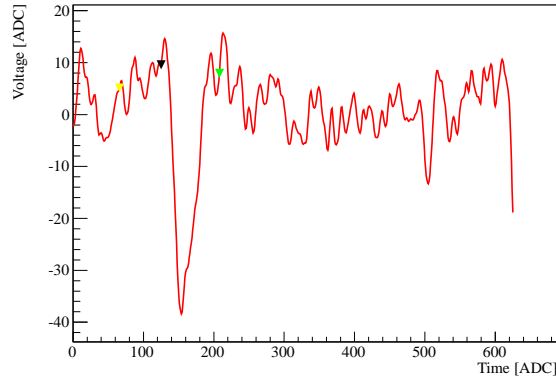

Figure 4.7: Example of a negative pulse. This kind of event can make the trigger fire, so in the new version of the OT a dedicated check is implemented to avoid this.

Compared to traditional algorithms, this trigger is much more powerful, but requires the knowledge of the average pulse and of the noise power spectrum of each channel. Consequently it cannot be used at the beginning of the data taking, since at least a long measurement is needed to estimate the average pulse and the noise power spectrum. After these first runs, it can be used as standard trigger, without reprocessing the continuous data saved on disk.

4.4   Trigger efficiency

At high energy the trigger efficiency (standard and OT) can be measured with a single pulser at few MeV. The idea is to evaluate efficiency as the number of triggered heater pulses over the number of fired heater pulses. The value obtained can be used on a large energy range that extends down to $\approx 100 \, \text{keV}$, well below the ROI of $0\nu\beta\beta$ decay. When dealing with low energies this approach no longer works, because going toward $0 \, \text{keV}$ the trigger efficiency goes to 0. In the OT case, the characteristic energy width in which this efficiency variation occurs is given by the filtered baseline resolution, as explained later.

In this scenario, a measure on a single pulser is not sufficient to estimate the trigger efficiency and a dedicated run is needed. This dedicated run takes the name of *n-pulsers* measurement, where a set of many heaters pulses are used, in such a way to study the efficiency as a function of energy. The DAQ system sets a pulser flag every time that the heater fires. A heater pulse is considered detected if a trigger is present within a $100 \, \text{ms}$ window after the DAQ flag. Then the efficiency ε is evaluated as the ratio of the triggered over the total fired heater pulses and the error is estimated using the formula

$$\sqrt{\frac{\varepsilon(1-\varepsilon)}{N}}$$

where N is the number of pulses fired from the heater for that energy.

As mentioned in sec.3.3.2, each time that a group of crystals were delivered from the producer some of them were operated as bolometer to check that they match the required quality. In one of these measurements, the Cuore Crystals Validation Run 2 (CCVR2), the first version of the OT was tested. A 2-days n-pulsers run was acquired and two Monte Carlo simulations were performed to validate the obtained results. The two Monte Carlo where carried out with the method described in [143]:

- a run with simulated heater pulses, generated with a flat spectrum between 1 and $50 \, \text{keV}$, intended to validate the Monte Carlo. The time interval between two consecutive heater pulses was $25 \, \text{s}$, like in the n-pulsers measurement;

- a run with simulated particle pulses, generated with a flat spectrum between 1 and $50 \, \text{keV}$, intended to evaluate the particle efficiencies. The time interval between two consecutive pulses was $25 \, \text{s}$, like in the n-pulsers measurement.
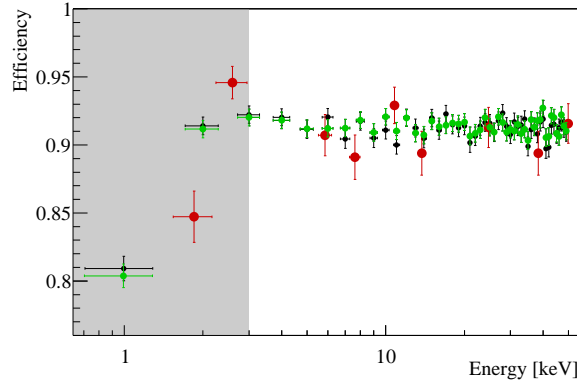
Figure 4.8: Detection efficiency on a CCVR2 channel. Particle Monte Carlo in black circles, heater Monte Carlo in green circles, heater scan data in big red circles. The gray band represents the region discarded for data analysis. The other CCVR2 channels show a similar behavior.

The Monte Carlo runs included simulated noise, generated from noise power spectra of n-pulsers measurement, and particle background, randomly generated from the CCVR2 energy spectrum and the measured event rate. In Fig.4.8 are shown the Monte Carlo results (both) compared to the n-pulsers measurement: black circles for particle Monte Carlo, green circles for heater Monte Carlo and big red circles for heater scan. The gray band was discarded from the subsequent analysis because of OT amplitude estimator bias due to negative noise fluctuations that lower the pulse amplitude. Similar results hold for the other CCVR2 channels.

From this graph two conclusions must be drawn: the Monte Carlo and the measured n-pulsers are compatible, validating the simulation results, and the trigger behavior on heater and particles is similar, demonstrating that the OT acts in the same way on pulser and particles.

In this case efficiency reaches a constant value of about 90% due to ^{210}Po contaminations and to the presence of the veto in the old version of the OT, that reflect in a non negligible quantity of dead time. Given its half-life of around 140 days, ^{210}Po is not a problem for CUORE-0, since crystals waited more than 2 years after their production to be measured.

Starting from July 2013 a n-pulsers measurement is carried out in each dataset of CUORE-0, to study the bolometers efficiency at low energy. Originally was proposed to perform more than one measurement per dataset, in such a way to have as much checks as possible of detector behavior. Thanks to the fact that subsequently was found a way to describe the efficiency slope, the runs number was lowered to one per dataset. At a first thought, one might expect a sharp slope for the efficiency as function of energy: if the pulser energy is smaller than the threshold this would not be triggered, on the contrary if it is larger it would be triggered, with efficiency directly passing from 0 to 1. The correct
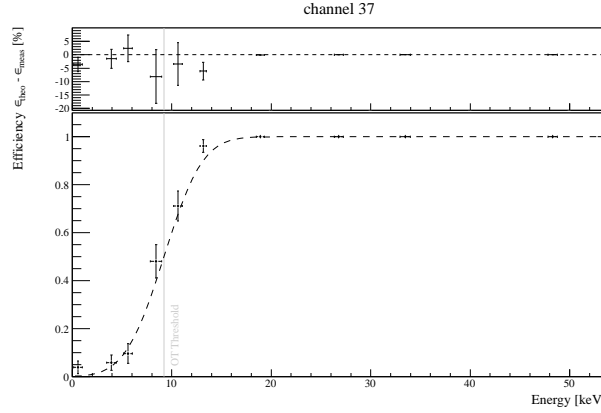
Figure 4.9: OT trigger efficiency for channel 37 as a function of energy, measured in a dedicated n-pulsers run in CUORE-0. In the lower part of the graph, points represent the measured efficiency obtained by the ratio $\frac{triggered\,pulses}{fired\,pulses}$, the dashed black line is the expected efficiency trend given by the erf and the vertical gray line is the OT threshold (50% efficiency by definition). In the upper part of the graph are shown the residuals.

way to describe the trend is to consider that the pulser peaks have a non-zero width, given by the energy resolution. Consequently the right (left) tail of a pulser peak could exceed (be below) the energy threshold and be triggered (not be triggered) leading to a intermediate efficiency.

Given this, the OT efficiency is expected to have a Gaussian cumulative density function and can be predicted with *a priori* informations. Using the error function (erf), efficiency ε at energy E is:

$$\varepsilon(E) = \frac{1}{2}\mathrm{erf}\left(\frac{E-\theta}{\sqrt{2}\sigma_{OF}}\right) + \frac{1}{2} \tag{4.12}$$

where σ_{OF} is the OF resolution and θ is the OT threshold, in this case imposed to be equal to $3 \times \sigma_{OF}$, both defined in the previous section. It is important to specify that the (selected) energy spectrum threshold is not mandatorily equal to the OT threshold, but it can be different and, for example, set equal to the value at which the 99% efficiency is reached, while at θ it is evident that efficiency is always equal to 50%. Fig.4.9 shows an n-pulsers measurement result for channel 37 of CUORE-0, with superimposed the corresponding erf, while the vertical line named OT threshold indicates the θ of the previous formula. In the upper part of the image there are the residuals between the theoretical curve and the experimental points.

The reason why no more than a single n-pulsers measurement is needed per dataset, is that by using the formula in eq.4.12, it is possible to evaluate the efficiency at any energy for that run. Indeed, taking the average pulse and the average noise, it is possible to monitor run by run the filtered baseline resolution
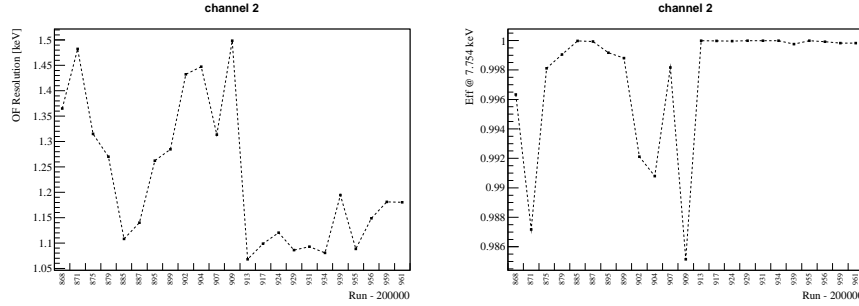
Figure 4.10: Left: Using the average noise of each run it is possible to monitor the OF baseline resolution run by run during data taking (channel 2 in the example). Right: taking this resolution it is possible to estimate, by the erf, the trigger efficiency at a given energy (typically the threshold selected for that channel during the n-pulsers run analysis, in this case the channel 2).

and the efficiency at the selected threshold. The former is possible applying the OF to the noise of the run. The latter is possible using the erf with the baseline resolution and the OT threshold corresponding to the selected run (σ_{OF} and θ of previous formula) and then looking at the efficiency for the chosen spectrum energy threshold. Predictably the lower (better) the resolution, the higher the efficiency (for a given energy), as can be seen in Fig.4.10.

4.5 Trigger application

The OT effectively presents better results with respect to the standard trigger, the DT. The working principle of this is explained in Fig.4.11 and is very simple: the difference in the signal amplitude of two samples at a fixed time distance (average) is compared with a reference value (threshold); if this quantity is bigger than the reference value for at least a given number of consecutive samplings, a trigger flag is set in the data stream on the first sample that exceeded the threshold. Also in this case the trigger is software generated revealing to be simple to be optimize channel-by-channel.

In Fig.4.12 it is shown a comparison of the two triggers used in CUORE-0, OT in red and Derivative in black. On the left there are the experimental points from two different n-pulsers runs for channel 2 (circles for OT, squares for Derivative), one run per trigger kind. On the right are presented the 90% efficiency threshold distributions (solid red line for the OT, dashed black for the DT). It is important to underline that in both cases the 90% efficiency threshold is evaluated from the erf, but for the OT the curve is given from *a priori* informations, while for the DT it is the result of a fit. As can be seen in the figure the OT energy threshold is lower than that of the DT.

Finally to validate the improvements of the OT it is possible to simply compare the two energy spectra. In Fig.4.13 the two spectra are presented,
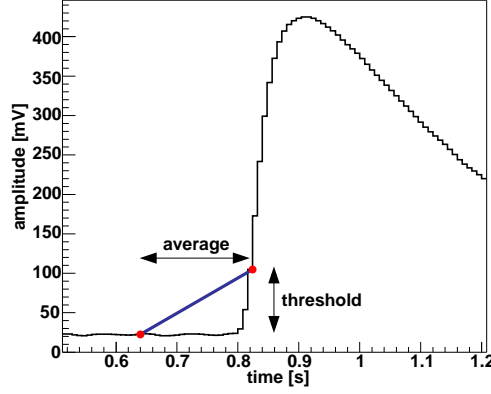
Figure 4.11: DT working principle. The trigger fires when the amplitude difference between two points at a fixed time distance (average) is larger than a reference value (threshold) for a given number of samples. Being a software generated trigger, it can be easily optimized channel-by-channel.
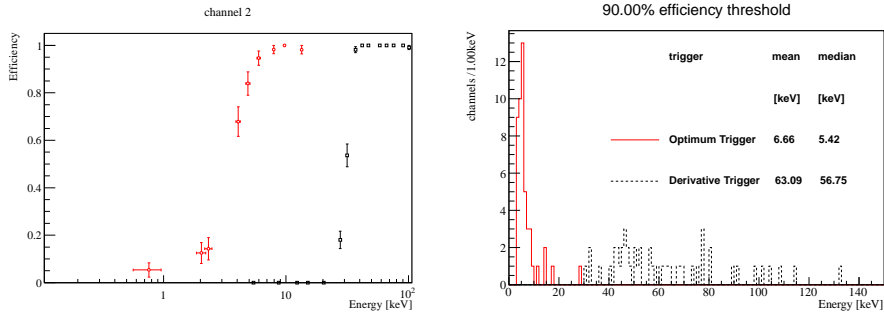
Figure 4.12: Left: slope of the efficiency as a function of the energy for Optimum (red circles) and Derivative (black squares) triggers for channel 2 of CUORE-0 in dataset 2088. Right: threshold distribution for the Optimum (solid red line) and the Derivative (dashed black line) triggers in dataset 2109. The threshold in this case is defined as the 90% efficiency resulting from the erf. For the OT the erf parameters are evaluated from the noise power spectrum, for the DT they are the result of a fit.

the one triggered with the OT in red solid line and the one triggered with the DT in black dashed line, for channel 20 using background runs from dataset 2097 of CUORE-0. OT spectrum goes down to smaller energies, with respect to DT. As it can be seen, the number of events dramatically increases going toward 0 keV. This large number of counts has to be ascribed to noise events and not to wrong triggers, as for example triggered side lobes, generated from the new implementation of the OT. This rise in the spectrum can be seen as the convolution of the trigger efficiency with the right tail of a very high Gaussian distribution of noise events centered at 0 keV, that hence results in a pedestal, which energy depends on the channel, in this case about 5 keV.

To prove that the cause of this pedestal is not the new trigger, the old and new versions can be compared on the CCVR2 data (see the previous section). This comparison is presented in Fig.4.14: the two spectra are totally compatible down to the smallest value considered (3 keV). In Fig.4.13 there are no cuts applied to the data, to magnify the difference between the two triggers, while in Fig.4.14 a channel dependent cut on a shape parameter (see sec.5.2.1.1) is applied to select only pulses of physical events together with the rejection of bad intervals.

The spectra in Fig.4.14 presents two evident peaks: one at 4.7 keV and one at 31 keV. The latter is a X-ray from Sb, which is due to EC decays of metastable Te isotopes. It is no longer visible in CUORE-0 due to the short half-lifes involved. While the peak at 4.7 keV has the energy of the L_1 atomic shell of Sb. This in principle indicates that the line could be ascribed to the EC decay of a Te isotope, but none of the known or predicted isotope decays can explain this observation, fundamentally due to half-lifes and intensity incompatibilities (for more details see [119]).
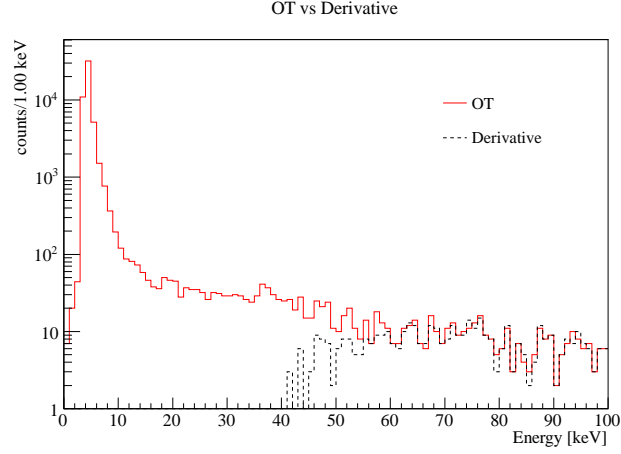
Figure 4.13: Comparison of the OT and DT on background runs from dataset 2097 for channel 20. OT spectrum goes to smaller energies and presents a very high number of events in the lowest part. This is not a physical peak, but it can be interpreted as the right tail of noise events whose distribution is a Gaussian centered at 0 keV. No quality cuts are applied to the data in these spectra.

Figure 4.14: Old and new OT versions applied to CCVR2. The two spectra are the result of the sum over 3 channels. Going towards low energies the two spectra are compatible, meaning that the new version of the trigger does not introduces fake events, like triggered side lobes. Quality cuts are applied to the data, to select good quality physical events (see sec.5.2.1.1).

Chapter 5

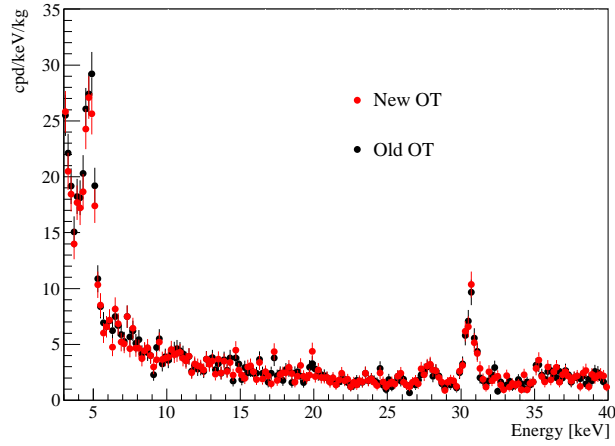# Low energy analysis

5.1 Introduction

To set limits on DM, once data are triggered with the OT, it is necessary to generate the low energy spectra of CUORE-0 channels. These spectra are produced using the so-called *first-level analysis*. During this analysis, triggered data are energy-calibrated and many other quantities are evaluated for each pulse.

Particular attention must be put into the calibration quality control, which for low energy region is harder to check than for the standard one, given the absence of a suitable energy peak in the calibration sources used in CUORE-0. Consequently a dedicated approach has been developed to overcome this problem and verify the correctness of the calibration function.

This chapter presents all the steps to be followed in the standard analysis; subsequently the method for assessing the quality of calibrated data is described.

5.2 First-level analysis

After detector signals have been digitized and triggered, it is possible to start with the first-level analysis. With this procedure an energy value is associated to each pulse, more precisely to its amplitude. In addition several environmental informations (like event time, channel number, detector floor, *etc.*) and pulse shape parameters are stored. To reach this goal, four steps are needed during this offline analysis:

1. *Optimum Filter*, to correctly evaluate the pulse amplitude;

2. *stabilization*, to eliminate the signal dependence on the temperature variation of the thermal bath;

3. *calibration*, to give an energy value to the pulse;

4. *coincidences*, to calculate time coincidences between events.

5.2.1 Optimum Filter

This algorithm has been deeply discussed in sec.4.2. The reason of its implementation is that a simple maximum-minus-minimum algorithm, applied to the acquired window, would be spoiled by the stochastic noise of the detector. Since OF maximizes the SNR, it optimize the signal resolution. Hence the filtered pulse height is taken as the signal amplitude. The filtering performed during the OT is repeated because those filtered windows are used only to trigger and are not saved.

5.2.1.1 Shape parameter

As previously stated, the OF is sensitive to pulses having the same shape of the average signal. When a pulse with different shape occurs, its filtered amplitude is suppressed and the filtered shape also is different from expectation. To suppress fake signals a pulse shape indicator was implemented in the analysis code. This means that the indicator is used only during offline analysis and not to determine the presence of a signal during trigger phase.

The algorithm is relatively simple. A triggered pulse is fitted using a cubic spline of the filtered average pulse, and the χ^2/ndf of the fit is used as shape indicator. The cubic spline is needed to have a continuous function, and to fit fractional time delays. The fitted parameters are the amplitude and the position of the pulse, while the baseline is fixed at zero. Since the OF is already a fit of the data samples, this fit only serves to remove the digitization effects and to estimate the χ^2. Before fitting, the maxima of the fit function and of the triggered pulse are aligned. The pulse position is then varied in the range $[-1, 1]$ samples, that is the maximum possible shift due to digitization. The amplitude is varied in the range $[A, A/(1 - \delta)]$, where A is the amplitude of the filtered signal and δ is the maximum allowed suppression in amplitude due to the digitization. This parameter is estimated from the filtered average pulse, computing the amplitude difference between the maximum (which has unitary amplitude) and the amplitude of the point right after. The fit range L corresponds to four filtered average pulse widths.

Finally, the shape indicator is computed as:

$$\chi^2_{OT} = \sum_{i=0}^{L-1} \frac{(\tilde{y}_i - f_i)^2}{\sigma_L^2(L-2)} \tag{5.1}$$

where $\tilde{y}$ is the filtered signal, f is the estimated fit function, and σ_L is the amount of noise expected in a window of length L. The error of each point, in fact, is not the average error of the entire filtered window in eq.(4.11), but it is lower since low frequencies are not seen in a smaller window:

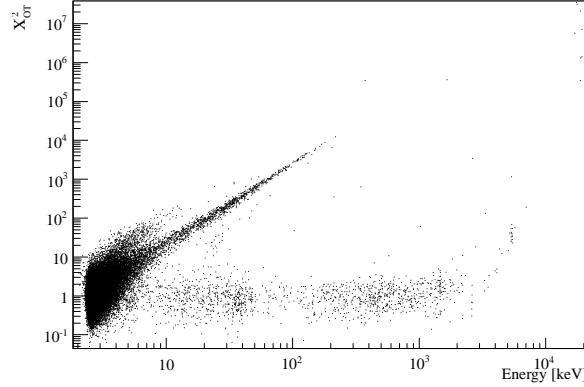$$\sigma_L^2 = \sum_{k=M/L}^{M-M/L} h^2 \frac{|s(\omega)|^2}{N(\omega)}.$$

Figure 5.1: χ^2_{OT} versus energy (see sec.5.2.3 for energy calibration) for channel 46 in dataset 2088. Looking at the corresponding pulses, bad ones are characterized by higher values of χ^2_{OT} starting from low energies. Augmenting energy, also good pulses start to rise their χ^2_{OT} value, since their shape depends on energy itself. The large amount of events below 10 keV is due to the detector noise as explained at the end of sec.4.5.

It must be noticed that, even if eq.(5.1) has the form of a χ^2 it does not follows a true χ^2 distribution. The expected value is still 1, but the variance is not $2/(L-2)$ since the errors are correlated at the filter output. An example of its distribution as function of the energy (see sec.5.2.3 for energy calibration) is given in Fig.5.1 for channel 46 in dataset 2088, where good and bad pulses are easily identifiable, the latter having higher χ^2_{OT} already at low energy. The reason why also good pulses start to have a large value of χ^2_{OT} at some energy is due to the fact that the pulse shape depends on energy. The large amount of events at small energy (< 10 keV) is due to the noise events that form the pedestal visible in the OT spectrum in Fig.4.13.

The trigger and the pulse shape algorithms take advantage of the informations that can be extracted from the OF theory. All the parameters are fixed and automatically calculated at the DAQ start. Actually the χ^2_{OT} turns out to be the most powerful parameter to discriminate between good physical events and other kinds of events, like spikes, tower vibrations or sharp baseline jumps, *e.g.* in Fig.5.2.

5.2.2   Stabilization

Signal amplitude is highly dependent on the bolometer temperature. Consequently two isoenergetic events may have different pulse amplitude. This would dramatically worsen the detector energy resolution.

To reduce this effect a pulser is used, as mentioned in sec.3.3.2. The pulser is
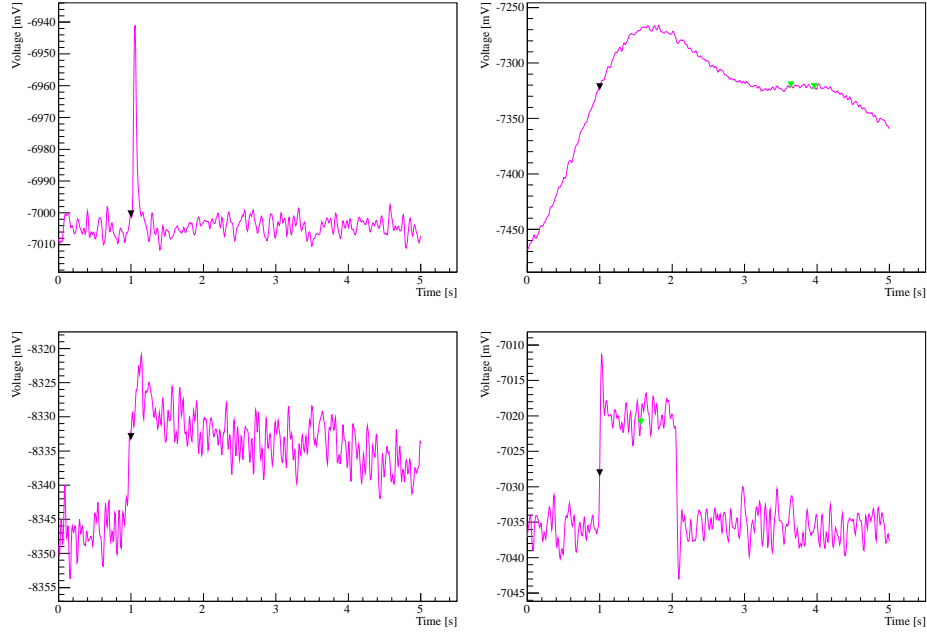
Figure 5.2: Examples of bad pulses. Top left is a spike ($\chi^2_{OT} = 79.5106$), generated by electronics or by a radioactive decay on the thermistor. Top right is the "pulse" produced by a tower vibration ($\chi^2_{OT} = 687.199$), generally due to vibration induced by the cryostat or to the water pump located in the CUORE-0 hut. Bottom left is a sudden baseline jump ($\chi^2_{OT} = 5.54894$) and bottom right some electronic noise ($\chi^2_{OT} = 8.29397$). All these kind of events is easily rejected using χ^2_{OT}, starting from energies in the range $5 \div 10\,\mathrm{keV}$, depending on the channel.

a resistor that, due to the Joule effect, heats up when a current runs through it. In this way it releases some energy (always the same quantity) in the bolometer, simulating an event. Anyway a heater event is distinguishable from a real event having a $\chi^2_{OT} > 10$ starting from $\approx 20\,\text{keV}$, depending on channel and dataset. Exploiting this knowledge it is possible to stabilize signals, imposing that every pulser event has the same amplitude. This procedure provides a function that is used to correct each pulse amplitude. Anyhow the uncertainty introduced by the absence of this correction is linear with the pulse amplitude, consequently it is negligible at low energy.

The heater signal amplitude $a_h(b)$ (function of the baseline b, directly connected to the temperature) and the energy release E_h, are related by:

$$a_h(b) = G(b)E_h$$

with $G(b)$ the gain of the bolometer, namely the signal amplification. Therefore for an event with amplitude a that released an energy E

$$a = G(b)E = \frac{a_h(b)}{E_h}E.$$

Starting from this, it is possible to observe that a/a_h is a constant function of the baseline and is proportional to the energy. At the end the stabilized amplitude is obtained as

$$a_s = \frac{a}{a_h} \cdot 5000$$

where 5000 is an arbitrary scale factor. To check the quality of the result the pulser correction efficiency is measured: a Gaussian fit is performed on the stabilized pulser amplitude and the number of events obtained by integrating the curve is calculated; then the efficiency is evaluated as the ratio between this number and the known number of fired pulsers. Typical results are around 99%. It should be noticed that it is implicitly assumed that this correction factor is not dependent on the energy deposited in the bolometer.

In Fig.5.3 the pulser signal amplitude is shown as a function of the baseline before (left) and after (right) the stabilization. On the left also the fitting line is shown; in this case it is a straight line, but the analysis software can account for up to four different regions in which subdivide the scatter plot and try to stabilize the measurement.

5.2.3 Calibration

During the calibration process an energy value is assigned to the pulse amplitude. This is performed using known peaks in the energy spectrum of the bolometer. Since the goal of CUORE-0 is the lowest contamination possible, there are no internal lines intense enough to calibrate the detector in a reasonable time. Consequently a ^{232}Th radioactive source is introduced between the outer vacuum chamber and the external lead shielding (sec.3.3.2). Tab.5.1 lists
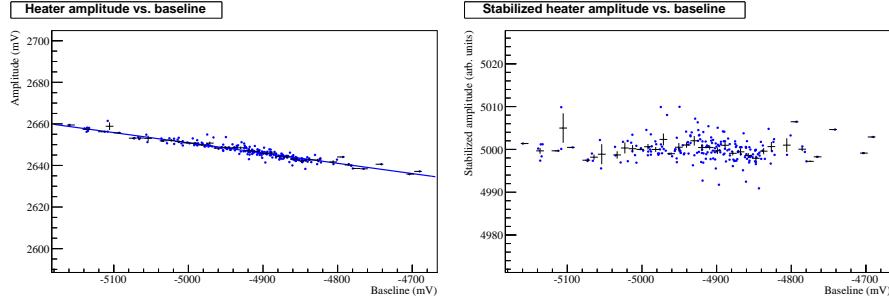
Figure 5.3: Pulser amplitude as a function of the detector baseline before (left) and after (right) stabilization. The blue line on the left is the result of a linear fit. Stabilized pulser amplitude is set to an arbitrary value of 5000 (right). With blue points are indicated the pulser events, while with black crosses the averages of points that fall in the interval given by the error width along the x-axis.

all the peaks employed for the spectrum calibration. Here second source means that there are two different lines that sum in a single peak in the spectrum.

The fitting function is a second degree polynomial with zero intercept, since it is assumed that for a zero deposit of energy there is a zero amplitude pulse[1]. Previously a third degree function with zero intercept was used to calibrate the spectra, but the calibration formula was changed after the demonstration that the second degree polynomial resolves better the peaks in the α region (above the ^{208}Tl line), leaving unchanged the ones in the γ region (from 0 to the ^{208}Tl peak). An example of CUORE-0 calibration function is shown in Fig.5.4. Here are presented the stabilized amplitude spectrum (top), the fitted calibration function (bottom, with nominal energy of the used peaks on y-axis). Typically χ^2/ndf values of the fit are below 4; having a good energy resolution, a high χ^2/ndf is expected. In the global calibration spectrum residuals from nominal peak positions are below 0.5 keV, apart from the one at about 1590 keV due to problems in the reconstruction of the double peak from ^{228}Ac and ^{208}Tl double escape [147].

5.2.4   Coincidences

Time coincidences are needed to identify signals generated by events that deposit energy in multiple crystals. The number resulting from coincidence evaluation is called multiplicity and is defined as the number of channels that record a signal within a defined time window of each other. In this analysis the interval duration is 100 ms. This window is said to be running, meaning that the time counter is reset every time that a signal is triggered, as long as the time elapsed between two consecutive events is smaller than the window length. Hence, if some particle, vibration or other perturbation crosses the tower, inducing

---

[1]When the constant term is left free to vary, it results compatible with zero.

Source	Energy [keV]	2nd source	2nd energy [keV]	Amplitude ratio
e^+e^-	511.0			
^{208}Tl	583.191			
^{228}Ac	911.204			
^{228}Ac	968.971	^{228}Ac	964.766	0.240
^{228}Ac	1588.9	^{208}Tl double esc.	1592.533	no ratio
^{208}Tl single esc.	2103.533			
^{208}Tl	2614.533			

Table 5.1: Calibration peaks from the ^{232}Th source. If present, 2nd source means that there are two lines that sum in a single peak in the energy spectrum. The amplitude ratio is defined as the branching ratio of the second decay divided by the branching ratio of the first decay within a peak; no ratio means that the sources are not correlated. Single and double escape are the energy of the ^{208}Tl peak (2614.533 keV) with a single or a double photon escape (of 511.0 keV each) from the crystal, respectively.
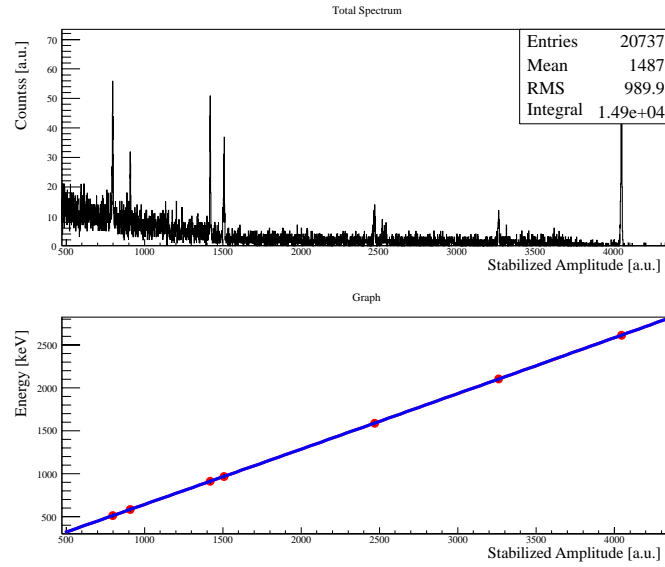
Figure 5.4: A CUORE-0 calibration function example. All seven peaks (see Tab.5.1) are used to calibrate the energy spectrum. In both graphs on the x-axis there is the stabilized amplitude. In the top panel there is the spectrum, in the bottom the fitting function (nominal energy of the peaks on y-axis). Although a second degree function with zero intercept is employed, the calibration function is practically linear. The typical χ^2/ndf value of the fit is below 4; as expected, a high χ^2/ndf arises as a consequence of the good energy resolution.

signals on various bolometers, all these registered events are correlated by the multiplicity. For example, if two events (and no others) are in time coincidence they have a multiplicity equal to 2.

Before calculating the multiplicity of an event, an energy and a χ^2_{OT} cut (only for energies smaller than 1100 keV) are implemented:

$$
\begin{cases}
E < \text{OT}_{99\%} & \Rightarrow & \text{event discarded} \\
\text{OT}_{99\%} \leq E \leq 1100 \, \text{keV} & \Rightarrow & \text{event kept } if \; \chi^2_{OT} < \chi^2_{OT-90\%} \\
E > 1100 \, \text{keV} & \Rightarrow & \text{event kept}
\end{cases}
$$

where E is the event energy, $\text{OT}_{99\%}$ is the energy at which the OT reaches the 99% trigger efficiency (different for every channel and dataset) and $\chi^2_{OT-90\%}$ is the χ^2_{OT} value corresponding to the 90% cut efficiency on signal events (channel and dataset dependent). The 99% trigger efficiency is calculated via the error function (see sec.4.4) and typical values are between 5 and 10 keV (all the values can be found in Appendix A). The $\chi^2_{OT-90\%}$ is obtained from the χ^2_{OT} distribution of events in the $80 \div 180$ keV interval with $\chi^2_{OT} < 10$ (see Fig.5.5 left), being that only signal pulses are present in this region, as evident looking at Fig.5.1: all the events (from background runs for any channel and dataset) in this region are taken and ordered by their χ^2_{OT}, at this point the 90th percentile is selected as $\chi^2_{OT-90\%}$, which generally is smaller than 3. The energy cut is to avoid undesired coincidences with noise events at low energy, while the χ^2_{OT} cut in the $\text{OT}_{99\%} \div 1100$ keV interval is to prevent coincidences with other non physical pulses, that can extend up to the MeV region.

Hence an event of defined multiplicity (namely multiplicity ≥ 1) belong to high quality data. An example of the application of these cuts is given in Fig.5.5 right, which is the same of Fig.5.1, with selected points highlighted in blue: almost all the noise and non physical events are excluded from the multiplicity calculation. Hereafter referring to multiplicity, this notation will be used: M1 for multiplicity = 1, M2 for multiplicity = 2 and so on.

5.3 Calibration check

Dealing with energy spectra it is fundamental to check the calibration quality. In the MeV region this is simple, since it is automatically done when the radioactive ^{232}Th source is used: residuals at nominal peak energies are measured during the calibration, as explained in sec.5.2.3. Instead, at low energy, the calibration quality is harder to verify. This is due to the fact that no peaks are clearly visible in the very low energy range.

A possible way is to look at the spectrum of M2 events. This is due to the possibility to find a peak around 27 keV, originated by three different X-rays from Te, as indicated in Tab.5.2. These lines are produced when the Te in a crystal hit by a particle is excited and releases one of these X-rays, which is then detected by an adjacent crystal. In background runs the statistics is too low to see anything, while in calibration runs this behavior is enhanced by the presence
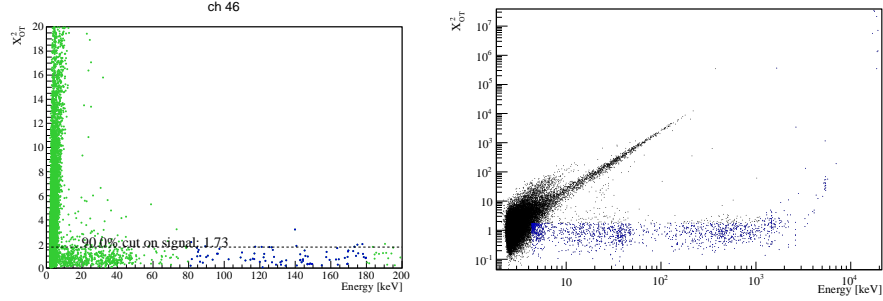
Figure 5.5: χ^2_{OT} versus energy for channel 46 in dataset 2088. Left: in blue are highlighted events in the selection $80 \div 180$ keV and $\chi^2_{OT} < 10$ used to calculate $\chi^2_{OT-90\%}$. Right: in blue are indicated the points considered for the multiplicity calculation. Only high quality/physically interesting events are included.

Origin	Energy [keV]	Intensity per 100 vacancies in the K-shell [%]
$K_{\alpha 3}$	26.875	0.00202
$K_{\alpha 2}$	27.202	25.3
$K_{\alpha 1}$	27.472	47.1
$K_{\beta 3}$	30.944	4.25
$K_{\beta 1}$	30.995	8.19
$K_{\beta 5}$	31.237	0.075
$K_{\beta 2}$	31.704	2.37
$K_{\beta 4}$	31.774	0.363

Table 5.2: Energies and intensity of K-lines originated from Te around 27 keV and 31 keV. Numbers from [84].

of the source. In particular right below most intense peaks there should be a smaller peak, with an energy equal to the energy of the main peak minus the X-rays average energy. This secondary peak should be more visible below the 2614.5 keV line, due to this peak higher rate and to the smaller background with respect the other ones.

Unfortunately, even for the dataset with the longest calibration (9.26 d for dataset 2088), there is not an evident peak in the single channel spectrum arising from the X-escape, neither around 27 keV, nor below the 2614.5 keV. Only grouping almost all channels of this calibration it is possible to see the X-ray peak in the M2 spectrum, as shown in Fig.5.6. Here, additionally, a smaller peak is visible at about 31 keV, also produced by the sum of various Te lines that have lower intensities with respect to the 27 keV ones (Tab.5.2). The 8 channels with the most and the worst resolutions have been discarded to produce this spectrum, to avoid that these pollute the peak region due to their high energy threshold.
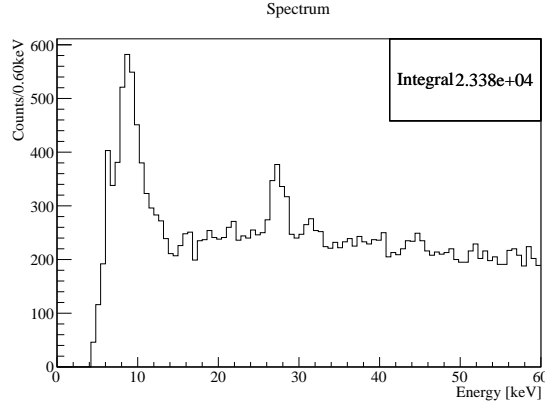
Figure 5.6: Two peaks are evident in the M2 spectrum of calibration runs of dataset 2088, at 27 keV and 31 keV. Both produced by Te K-shell X-rays, as indicated in Tab.5.2. To obtain a good energy spectrum the worst 8 channels (noisy or with bad energy resolution) have been discarded.

Given the situation, the only way is to put all the reprocessed calibration runs, from different datasets, together for a single channel. A simple sum of datasets with no further assumptions is not justified, as calibration coefficients are evaluated on a dataset basis. To overcome this problem and check the inter-dataset calibration, it is possible to use the pulser. As explained in sec.4.4, a n-pulsers measurement is performed in each dataset, thus selecting always the same pulser configuration (namely the dissipated power in the bolometer) it is possible to verify if its corresponding energy remains unchanged going through all the datasets. Pulser energies are selected to be in the region of interest DM and vary from ≈ 10 to ≈ 30 keV, depending on the channel. For example, Fig.5.7 shows the outcome for channel 52.

Once heater peaks have been fitted, results can be put together to select good datasets and discard the others. In Fig.5.8 is shown the outcome for channel 52. A dataset is maintained if the corresponding value is no more than $\sigma_{\text{dataset}} + 1$ keV from the mean, where σ_{dataset} is the error associated to the measured value. To make it easier to see in Fig.5.8 the ± 1 keV region is highlighted with a gray band around the mean. Tab.5.3 is the list of discarded channel/dataset pairs. Due to the way calibration bad intervals are defined and coefficients are calculated (see sec.3.3.3), low energy stable datasets (on a channel basis) are always a subset of high energy stable ones.

With the list of compatible datasets for each channel, it is now possible to group them and reach the highest calibration statistics possible. The fit on the 27 keV peak is performed using a fixed resolution gaussian plus a flat background. The fixed sigma is required to increase the fit quality and the number of positive results, reducing the free parameters. Its value is channel dependent and is assumed to be equal to the baseline resolution as comes from
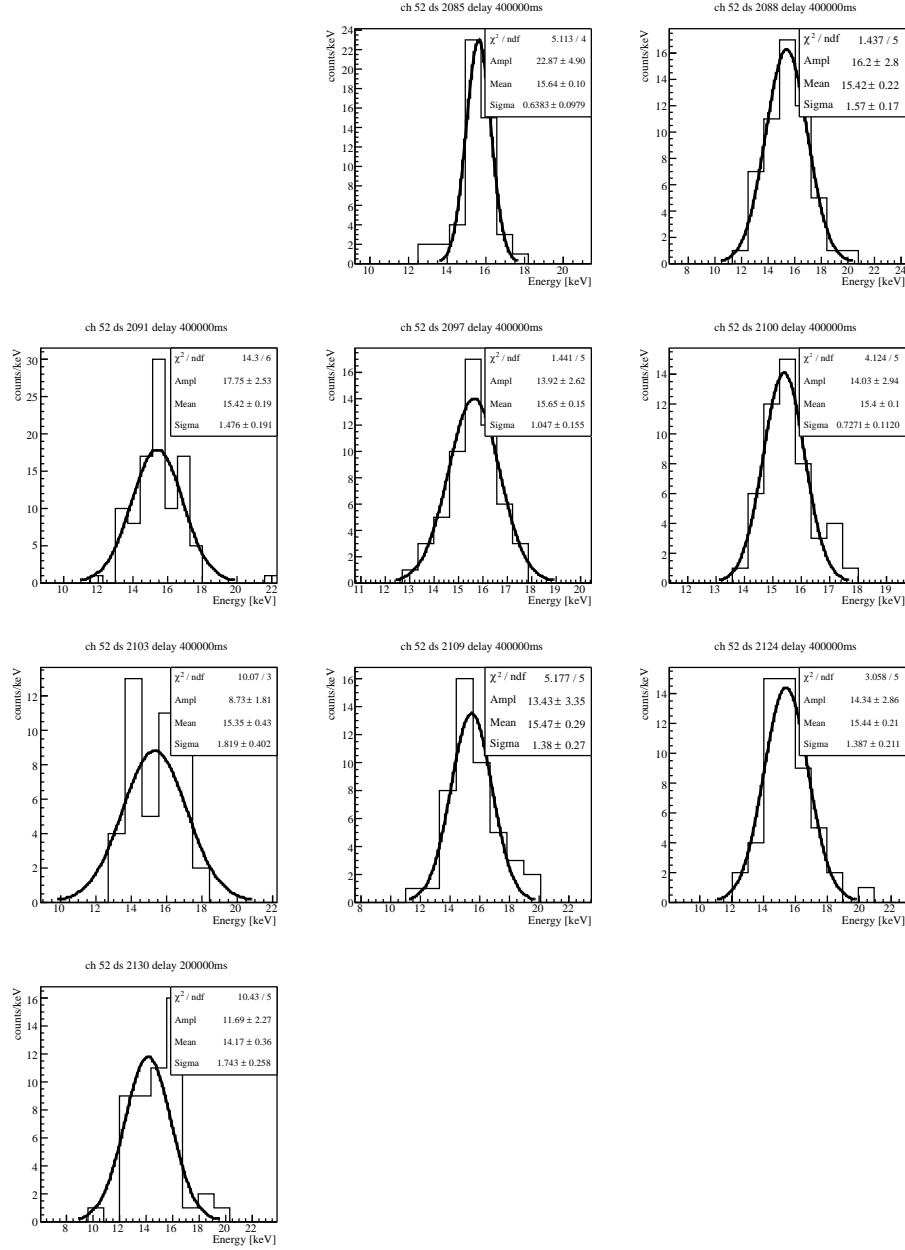
Figure 5.7: Fits on pulsers for channel 52, one per dataset. Datasets 2079 and 2139 (the first and the last ones) are absent because these whole datasets are marked as bad interval for this channel. Going across all the datasets always the same pulser is selected, so that low energy calibration stability can be checked.
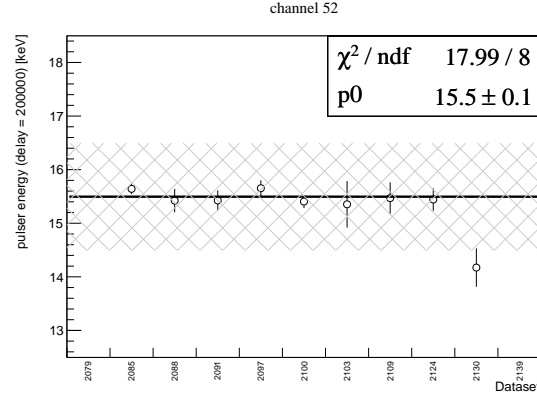
Figure 5.8: Pulser stability of channel 52. Each point represents a dataset, while the gray band corresponds to the mean energy $\pm 1\,\text{keV}$. The dataset is considered good if the distance between its point and the mean is smaller than $\sigma_{\text{dataset}} + 1\,\text{keV}$, where σ_{dataset} is the error for that dataset: in this case dataset 2130 is maintained, since its point error and the gray band are in "touch". Datasets 2079 and 2139 (the first and the last ones) are absent because these whole datasets are marked as bad interval (see sec.3.3.3) for this channel.

Channel	Datasets
5	2079, 2100, 2139
15	2124, 2130, 3139
22	2124
27	2079, 2097, 2124
29	2130
34	2130
37	2130
43	2079, 2085

Table 5.3: List of datasets to be discarded for each channel due to a non stable calibration, probed with the pulser.

Spectrum kind	Channels
M1	19, 45 (2)
M2, $E_{TOT} > 20\,keV$	2, 3, 6, 7, 9, 12, 17, 18, 19, 20, 21, 24, 25, 26, 31, 36, 41, 44, 46 (19)
M2, $E_{TOT} > 100\,keV$	2, 3, 6, 7, 9, 12, 17, 18, 19, 20, 21, 24, 25, 26, 31, 36, 41, 44, 46 (19)
M2, $E_{TOT} > 500\,keV$	2, 3, 4, 6, 9, 12, 14, 17, 18, 19, 20, 21, 24, 25, 26, 31, 32, 41, 46 (19)
All kind	2, 3, 4, 6, 7, 9, 12, 14, 17, 18, 19, 20, 21, 24, 25, 26, 31, 36, 41, 44, 46 (22)

Table 5.4: List of channels that show a well fitted 27 keV peak, divided into the four kinds of spectra. The total number of channels is indicated in parentheses. E_{TOT} indicates the total energy of the couple of events.

all the selected calibration runs. The bolometer baseline is attained by means of a dedicated trigger, that takes the name of Random Trigger, that every 300 s takes the detector data flow content and stores the measured sample. Consequently the acquired points distributions are gaussians with a resolution given by baseline RMS.

Four different sets of data are taken into account for the 27 keV peak fit:

- M1 events,

- M2 events with total energy larger than 20 keV,

- M2 events with total energy larger than 100 keV,

- M2 events with total energy larger than 500 keV;

where total energy is the sum of the energies of the two events that compose the pair. The higher the total energy, the lower the background, and the lower the statistics. To give an example, in Fig.5.9 are the four spectra for channel 32. In this case there is a visible peak only in the M2 spectrum with total energy higher than 500 keV. In total, 22 channels show a well fitted peak in at least one spectrum. The complete list is in Tab.5.4. Consequently only these channels can be used to produce low-energy spectra and thus for DM study. Comparing Tab.5.3 and Tab.5.4 it can be noticed that none of the good channels has a dataset to be excluded because of calibration instability.

Finally, to check the overall calibration of the detector, a fit on the spectrum obtained by grouping these 22 channels is performed. The fit is implemented on the 27 keV and on the 31 keV peaks using a flat background and two gaussians with a common sigma. The result is presented in Fig.5.10. Making a weighted mean of the lines of Tab.5.2 the expected values for the peaks are 27.38 keV and 31.11 keV, while the measured ones are 27.50 ± 0.06 keV 31.47 ± 0.16 keV, respectively. Both are compatible within 2σ with the real values, and lead to a weighted mean calibration uncertainty of 0.15 keV at 28.03 keV.
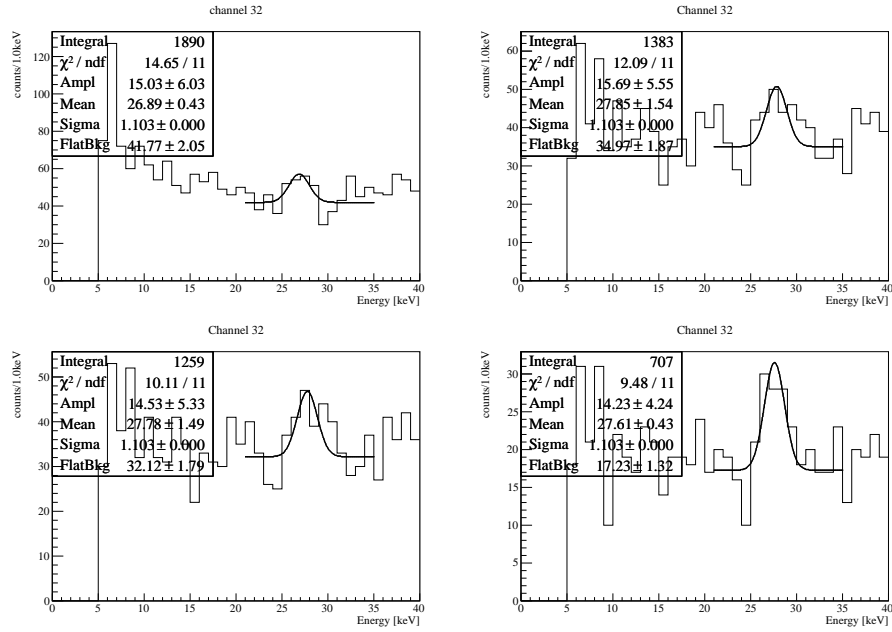
Figure 5.9: Fixed sigma gaussian plus flat background fits to the 27 keV peak for channel 32 on four different kind of spectra: M1 (top left), M2 with total energy larger than 20 keV (top right), 100 keV (bottom left) and 500 keV (bottom right). Total energy is the sum of the energies of the events that compose the pair (hence the single event energy, the one plotted, can be arbitrarily small). The peak is unambiguously identifiable only in the fourth case.

Figure 5.10: Global fit to the 27.38 keV and 31.11 keV peaks. All 22 channels indicated in Tab.5.4 are used. The overall calibration uncertainty is 0.15 keV at 28.03 keV.

Chapter 6

Low-energy spectra and modulation study

6.1 Introduction

Once energy calibration has been checked in the keV region, it is possible to apply further run selection before drawing the detector low-energy spectrum, in order to work with data of the highest quality possibl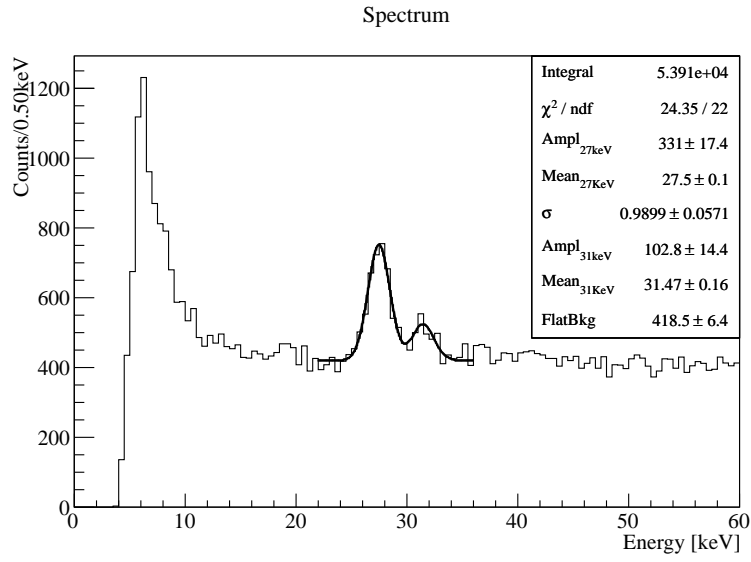e. This selection is focussed on lowering the energy threshold. Then, starting from this spectrum, one can choose what approach to follow for the DM analysis.

In this last chapter are presented the low-energy spectrum of CUORE-0, the analysis technique and the results of the study of DM.

6.2 Runs selection

Before proceeding with the low-energy spectrum production, some additional screening must be done in order to improve data quality. One cut has been already described in sec.5.3: the list of channel/dataset pairs to exclude due to calibration instability (summarized in Tab.5.3). Two further selection criteria are applied: one is to remove five runs where the event rate is extremely high and the other is to keep only runs with low noise and hence a good energy resolution.

6.2.1 High counting rate runs

For not yet completely understood reasons, there are five runs - the final ones of dataset 2109 - where the counting rate of low-energy events jumps to values much higher than the rest of the dataset and of CUORE-0 in general. In Fig.6.1 is presented the counting rate of channel 19 as a function of time for M1 events in the $10 \div 15\,\mathrm{keV}$ range. It is evident that during the last days of the dataset
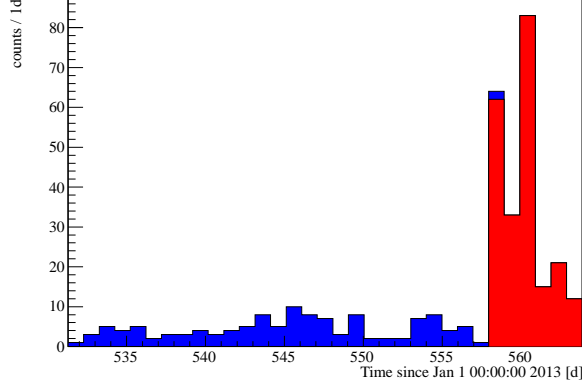
Figure 6.1: Channel 19 time displacement of events from $10 \div 15\,\mathrm{keV}$ range in dataset 2109. The bin width is $1\,\mathrm{d}$. In red are highlighted the five runs with a very high event rate.

something happened in such a way that these runs (indicated in red) account for a large part of the total number of events (up to 65%). A possible source of this high count rate is mechanical vibrations, as for example those induced by the pumps on top of the cryostat.

A useful tool to try to understand the origin of this phenomenon is the study of the noise power spectrum: if the source is mechanical or electronic, one or more peaks should be visible at some characteristic frequency. Comparing noise power spectrum of these runs with respect to other runs for various channels, no notable differences are visible (see Fig.6.2 as example), leaving the problem unsolved.

Other possible causes for this increase, such as neutron sources present underground and supernovae explosions, were ruled out. Regardless of the origin of these events, it is undeniable that such a high rate would spoil both the low-energy spectrum and the DM study. Consequently it has been chosen to exclude these runs from the subsequent studies.

6.2.2 Low noise runs

To aim for the lowest to the lowest possible energy threshold, the exclusion of noisy runs is a fundamental step. The simplest way to do this is to discard runs with a large baseline resolution. The baseline resolution of each run is evaluated as the RMS of the points sampled using the Random Trigger, already mentioned in sec.5.3. The value to apply the cut is median $+ 2\,\mathrm{RMS}$, where median and RMS are referring to the distribution of the run resolutions, in particular RMS is referring to the RMS of the RMSs (namely the resolutions) distribution. The $2\,\mathrm{RMS}$ cut is effective, but does not remove too much statistics (see Appendix B). From these calculations are excluded the five high counting rate runs and
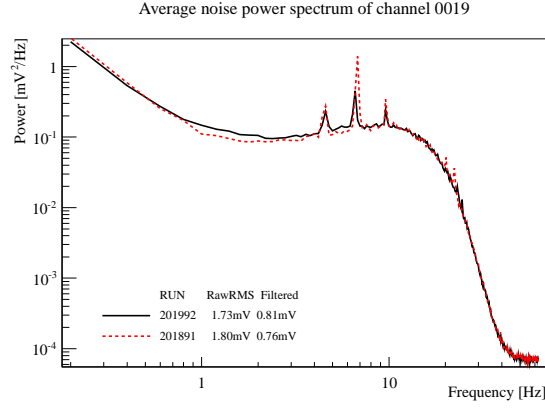
Figure 6.2: Noise power spectrum comparison for two runs of dataset 2109 for channel 19. One of the two belongs to the five runs with a high counting rate (201992). There are no evident differences, such as new peaks at some frequencies, as would be expected if the source of these events were mechanical or electronic.

the runs belonging to a dataset marked as bad from the pulser stability study, that are channel dependent, as explained in sec.5.3. An example of this is given in Fig.6.3 for channel 17. Here each point represents a run resolution, expressed as a function of time for a easier understanding of the detector behavior during data taking. The time scale is in days since January 1st 2013 in vision of the future DM analysis (see sec.6.4). Here the dashed line represents the applied cut, hence runs corresponding to points over it are discarded. Trends and cuts for all the channels (excluded channels 1 and 10) can be found in Appendix B.

6.3   low-energy spectrum

Now that the whole data selection has been defined, it can be implemented to draw the low-energy spectrum of CUORE-0. Some cuts are applied to these data, to select the desired kind of signal: all the bad intervals are rejected and only M1 events are considered (hence a χ^2_{OT} cut is implicitly implemented, as described in sec.5.2.4). The trigger and cut efficiencies are evaluated as follows:

- OT: only energies larger than the energy at which the trigger reaches 99% efficiency are considered; hence efficiency is assumed as unitary.

- χ^2_{OT}: in this case it is first fixed the signal efficiency and then the cut value comes consequently. In particular the chosen efficiency is 90% and the corresponding $\chi^2_{OT-90\%}$ is measured for each channel/dataset pair (a more detailed explanation is in sec.5.2.4).

- M1: by means of the ^{40}K peak at 1461 keV, which is produced by a single
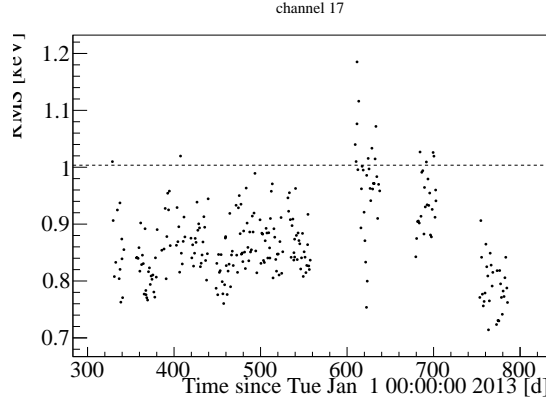
Figure 6.3: Baseline resolution time trend for channel 17. Each point corresponds to a single run, while the dashed line to the median + 2RMS of the distribution along the y-axis. Runs with a resolution below this line are kept; the others are excluded from the analysis.

γ. The M1 cut is applied to events in the energy region around the peak. A simultaneous fit of accepted and rejected events is then performed and the efficiency is evaluated as the ratio of the number of the accepted to the total number of events in the peak. Both populations are shown in Fig.6.4. The fit components are a gaussian and a flat background. To obtain a result as consistent as possible with the data, only selected channels and runs are used.

• Bad intervals: the efficiency is accounted for in the live time calculation.

Hence the cuts efficiency results to be:

$$\varepsilon_{cuts} = 0.9 \cdot \varepsilon_{M1}$$

where 0.9 comes from the 90% efficiency of $\chi^2_{OT-90\%}$.

Individual spectra, corrected for the efficiency, are presented in Fig.6.5 for all 22 selected channels. As can be seen, all the spectra exhibit a quite homogeneous behavior.

Putting together all these channels one obtains the global spectrum, for a total exposure of $9.25\,kg\cdot y$, displayed in black in Fig.6.6. The large peak visible at about $5\,keV$ is the noise pedestal, already described in sec.4.5, which end is at about $10\,keV$.

Two bumps are evident in the $\approx 30 \div 45\,keV$ range. The nature of these elements is unknown, but they are recognizable also in CCVR2 and characterize the spectrum of each single channel (see Fig.6.5). All of this sustains the hypothesis that this is a physical process taking place in the TeO_2 bolometers or in the material surrounding and supporting them. Given the shape and width
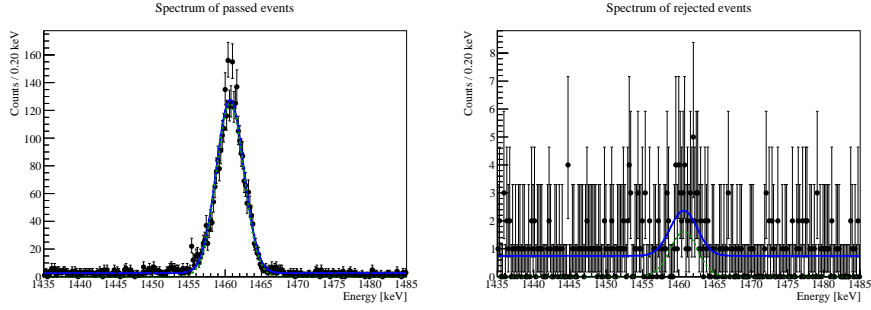
Figure 6.4: Accepted (left) and excluded (right) events for the calculation of M1 cut efficiency from the ^{40}K peak at 1460.830 keV. Accepted are the events that remain after the M1 cut application, while rejected are the ones that are discarded. In blue is indicated the gaussian and flat background sum, in green the peak component only.

they are probably multiple peaks summed together, or some β-decays. A possible candidate is the ^{210}Po, that presents a β-spectrum with an end point at 16.96 keV and with a de-excitation energy of 46.5 keV (most of the cases through a conversion electron). This produces a broad signature in the energy region that goes from 40 to 60 keV, whose shape depends on the location of the Pb contamination [136]. Another interesting feature is the drop of the counting rate after these structures, that likely is due to the achievements obtained in the material cleaning and to the crystals age. In any case, a more detailed studies and simulations are being carried out to understand these behaviors.

Finally it can be noticed that, although the number of counts is low, even compared to the one in CCVR2 [119], a DM study can be addressed only by means of the annual modulation. Indeed the expected DM signal is small to be directly appreciated as a diffuse increase in the counting rate; so the detector background would have to be considerably reduced before a measurement of the total DM counting rate could be attempted.

6.4 Annual modulation fitting approach and results

DM annual modulation fit is performed on same data selected for the low-energy spectrum, with the additional requirement to take events only from a particular energy range, to probe potential variations with changing energy. Ten ranges are taken into account:

- $10 \div 15$ keV,

- $15 \div 20$ keV,

- $20 \div 25$ keV,
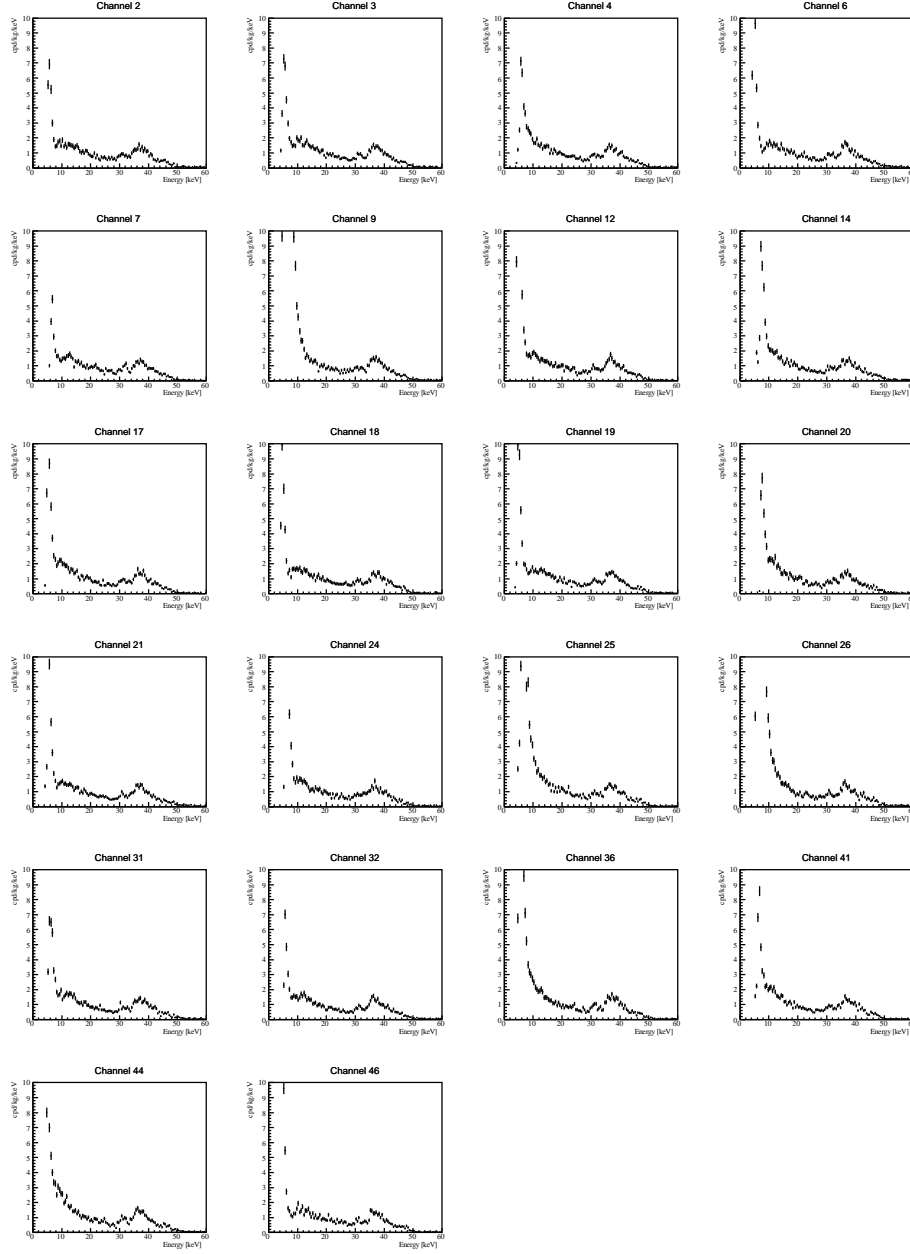
Figure 6.5: Energy spectra, corrected for the efficiency, of the 22 channels selected for low energy analysis. Each spectrum is in the $0 \div 60$ keV range and binned 0.5 keV, while the y-scale is fixed to $0 \div 10$ cpd/keV/kg. It is evident that the various spectra are consistent with each other.
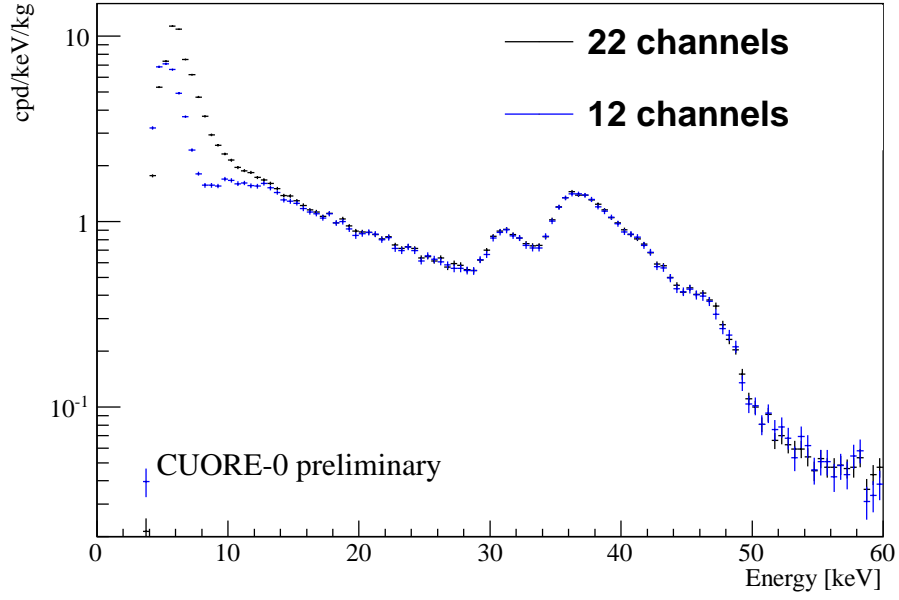
Figure 6.6: In black the global low-energy spectrum of CUORE-0 binned at 0.5 keV, produced by the sum of the 22 channels presented in Tab.5.4. The total exposure is 9.25 kg·y. In blue the global low-energy spectrum of CUORE-0 binned at 0.5 keV, produced by the sum of the 12 channels with a threshold smaller than 10 keV, taken among the ones presented in Tab.5.4. The total exposure is 5.00 kg · y. The logarithmic scale on the y-axis is to enhance the visibility of the two bumps present in the $\approx 30 \div 45$ keV range, just before the drop of the counting rate. The origin of these events is currently unknown.

- $25 \div 30\,\text{keV}$,

- $30 \div 35\,\text{keV}$,

- $35 \div 40\,\text{keV}$,

- $40 \div 45\,\text{keV}$,

- $45 \div 50\,\text{keV}$,

- $50 \div 55\,\text{keV}$,

- $55 \div 60\,\text{keV}$.

To be conservative, only channel/dataset pairs with an $\text{OT}_{99\%}$ smaller than the lower bound of the interval are kept. This is because a different approach would imply some assumption on the interaction behavior of these particles with the detector. Hence if, for example, a channel/dataset has $\text{OT}_{99\%} = 13\,\text{keV}$, all the runs of that dataset will not be considered for that channel in the time spectra construction in the $10 \div 15\,\text{keV}$ range, but it will in the other intervals. This further cut implies that the M1 efficiency is newly evaluated for each considered ensemble, using only channel/dataset pairs that passed the cut.

To correctly draw the annual trend of events, another efficiency has to be taken into account: the time bin occupancy. Indeed, the detector is not constantly acquiring background runs, hence for each temporal bin there will be a different occupancy efficiency, defined as the ratio between the live time in the bin and the bin width. A proportionality law is applied to correct this effect, *e.g.,* for a bin occupied 50% of the time, the number of events will be doubled. No modulation corrections are considered within each bin because of their small expected amount and more generally because there is no *a priori* information to evaluate their contribution. Calling ε_{bin} the total bin efficiency:

$$\varepsilon_{bin} = \varepsilon_{cuts} \cdot \varepsilon_t$$

where ε_t is the bin occupancy.

As with the energy spectrum, the single channel time trend is produced first and then the global time spectrum. The latter is constructed bin-by-bin, by summing up all the single channel spectra contents for that bin (the width is the same), not corrected for the efficiency, which is calculated and applied afterwards. Hence the bin content and its error are (content $\pm$ error):

$$\frac{\sum\limits_{i} N_{bin,i} \pm \sqrt{\sum\limits_{i} N_{bin,i}}}{\sum\limits_{i} \varepsilon_{bin,i}}$$

where i runs over all the selected channels.

Once the global time spectrum is constructed, on it are performed a fit with a flat function (absence of modulation) and a fit with a flat component plus a cosinusoidal, that accounts for the modulation:

$$B + A \cos\left(\frac{2\pi}{T}(t - t_0)\right)$$

where B is the flat component, which accounts both for the whole non-DM signal and for the constant part of the DM rate, A is the modulation amplitude, T is the period and t_0 the phase. The period is free to vary in the range $0.5 \div 2$ y and the phase is free to vary in the range $-400 \div 400$ d. For the $10 \div 15$ keV time spectrum, only the 12 channels with the lowest threshold are used (5.00 kg $\cdot$ y exposure, energy spectrum in blue in Fig.6.6), whereas the others exploit all 22 selected channels (9.25 kg $\cdot$ y exposure). Figures 6.7, 6.8, 6.9 and 6.10 present the fit outcomes for the $10 \div 15$ keV, $15 \div 20$ keV, $20 \div 25$ keV and $25 \div 30$ keV regions (the rest are in the Appendix C), while all the results are summarized in Tab.6.1. The bin is 30.51 d, since it is automatically calculated trying to satisfy the required width (30 d in this case) and considering the total elapsed time, given by first run start and the last run stop.

The modulation fit in the $10 \div 15$ keV has a non null modulation amplitude, but the period is smaller than 1 y more than 7σ.

The modulation fit in the $15 \div 20$ keV, $20 \div 25$ keV and $25 \div 30$ keV intervals shows a non-null modulated amplitudes, varying from 0.024 cpd/keV/kg ($20 \div 25$ keV) to 0.032 cpd/keV/kg ($15 \div 20$ keV), with a significance ranging from 2 to 3σ, that are compatible each other within 1σ. In all these cases the modulation period is compatible within 1σ with 1 y and the modulation phase is compatible with an inversion of phase with respect to June 2nd (maximum on December 2nd, the 336th day of the year) within 1σ, apart from the $25 \div 30$ keV range, where 2σ are needed. All the other fits are non compatible with a signal annual modulation, at least in a sufficiently evident and convincing way: modulation amplitude compatible with zero or period non compatible with 1 y and/or at the maximum of the allowed range (730 d $= 2$ y). Preliminary results from Toy Monte Carlo seem to indicate that the probability to obtain a fit with signal modulation amplitude equal or larger to the one measured in the three interesting intervals, irrespectively of the period and of the phase, starting from a flat distribution, could reach a non-negligible percentage. Anyhow, deeper studies are ongoing.

Comparing the expected WIMP rates in TeO_2 for different masses and $\sigma_0 = 10^{-41}$ cm^2 indicated in Fig.6.11 with these numbers, it is evident that they are a factor ≈ 10 smaller than the measured ones.

In conclusion, although a non null modulation amplitude with a period compatible with 1 y and a phase compatible with December 2nd (phase inversion) has been measured in three energy intervals from 15 to 30 keV, given the small exposure, the large errors and the reduced number of annual cycles, there is no concrete evidence to claim for a DM signal detection. The fact that in the $10 \div 15$ keV range the fit period is largely non compatible with 1 y means that probably detector stability and background have to be better understood, and that the data in other energy intervals are not ready to search for a DM signal yet. In addition some preliminary tests indicate that it is not hard to obtain a

All selected channels (bin 30.51 d) in 10.0 - 15.0 keV range

Figure 6.7: Modulation binned fits (bin width of 30.51 d) in the energy range $10 \div 15$ keV. In red solid line the flat fit (results on left pad), in blue dashed line the free T and t_0 fit (results on the right pad). The accumulated exposure is 5.00 kg·y. The free phase and period fit sees a modulation of 0.107 cpd/keV/kg amplitude with a period smaller than 1 y more than 7σ.

fit with a non-null modulation amplitude starting from a flat distribution. The CUORE experiment, with its higher mass and with a larger number of annual cycles, will be able to dwindle errors and to verify if there is a signal modulation repeating in time with the expected period.

All selected channels (bin 30.51 d) in 15.0 - 20.0 keV range

CUORE-0 preliminary

Entries	15
χ^2 / ndf	10.63 / 10
BkgAmpl	1.088 ± 0.010
ModulAmpl	0.03176 ± 0.01250
Period	308.9 ± 56.1
t_0	331.6 ± 40.2

Entries	15
χ^2 / ndf	17.7 / 13
BkgAmpl	1.082 ± 0.008

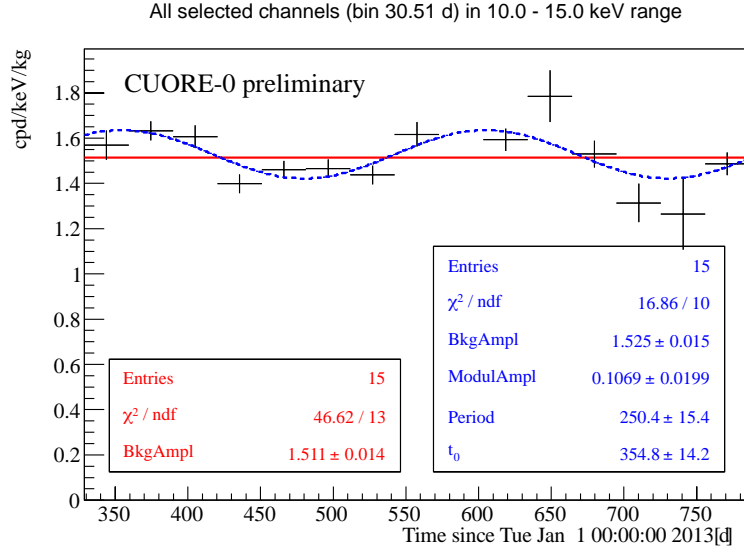Time since Tue Jan 1 00:00:00 2013[d]

cpd/keV/kg

Figure 6.8: Modulation binned fits (bin width of 30.51 d) in the energy range $15 \div 20$ keV. In red solid line the flat fit (results on left pad), in blue dashed line the free T and t_0 fit (results on the right pad). The accumulated exposure is 9.25 kg $\cdot$ y. The free phase and period fit sees a modulation of 0.032 cpd/keV/kg amplitude with a phase of 332 d and a period of 309 d. Values are compatible within 1σ with a period of 1 y and with a phase inversion (maximum of the signal on December 2nd).

All selected channels (bin 30.51 d) in 20.0 - 25.0 keV range

CUORE-0 preliminary

Entries	15
χ^2 / ndf	11.38 / 10
BkgAmpl	0.7847 ± 0.0082
ModulAmpl	0.02422 ± 0.01127
Period	364.6 ± 56.4
t_0	294.3 ± 44.1

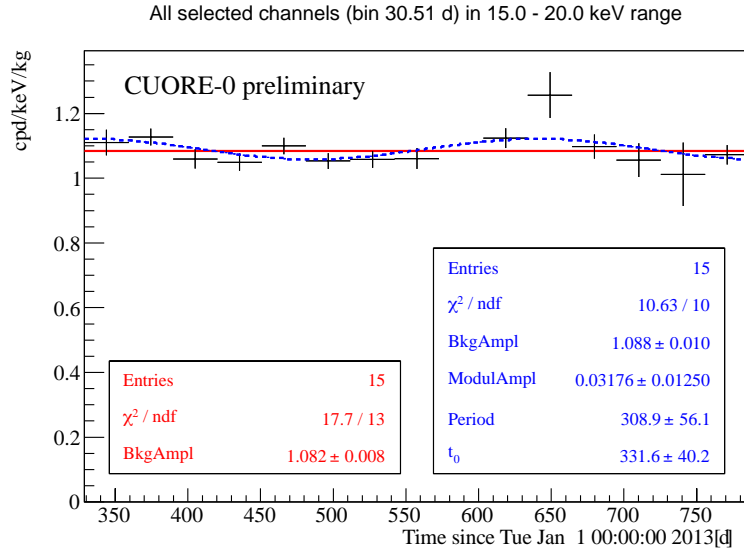| Entries	15
χ^2 / ndf	16.11 / 13
BkgAmpl	0.7788 ± 0.0072

Figure 6.9: Modulation binned fits (bin width of 30.51 d) in the energy range $20 \div 25$ keV. In red solid line the flat fit (results on the left pad), in blue dashed line the free T and t_0 fit (results on the right pad). The accumulated exposure is 9.25 kg·y. The free phase and period fit sees a modulation of 0.024 cpd/keV/kg amplitude with a phase of 294 d and a period of 365 d. Values are compatible within 1σ with a period of 1 y and with a phase inversion (maximum of the signal on December 2nd).

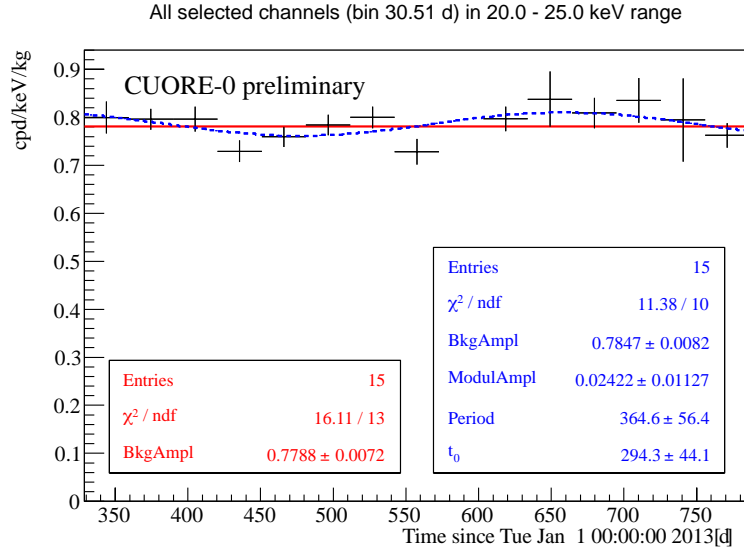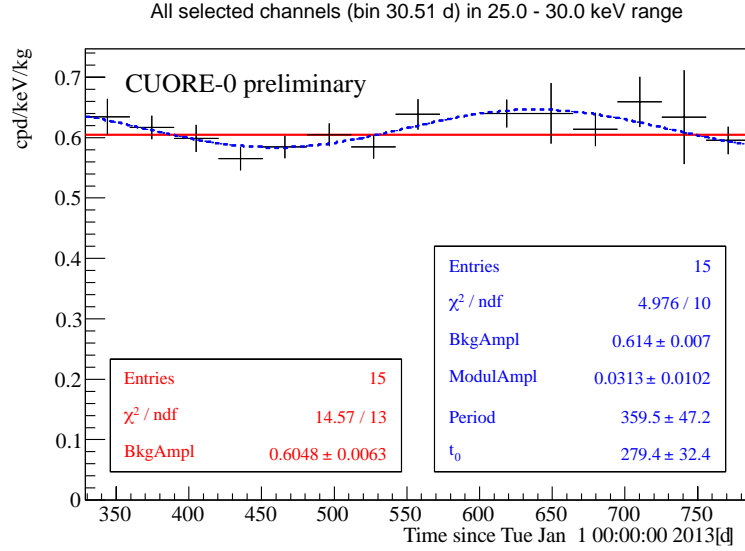All selected channels (bin 30.51 d) in 25.0 - 30.0 keV range

Figure 6.10: Modulation binned fits (bin width of 30.51 d) in the energy range $25 \div 30$ keV. In red solid line the flat fit (results on left pad), in blue dashed line the free T and t_0 fit (results on the right pad). The accumulated exposure is 9.25 kg·y. The free phase and period fit sees a modulation of 0.031 cpd/keV/kg amplitude with a phase of 279 d and a period of 360 d. Values are compatible within 1σ with a period of 1 y and within 2σ with a phase inversion (maximum of the signal on December 2nd).
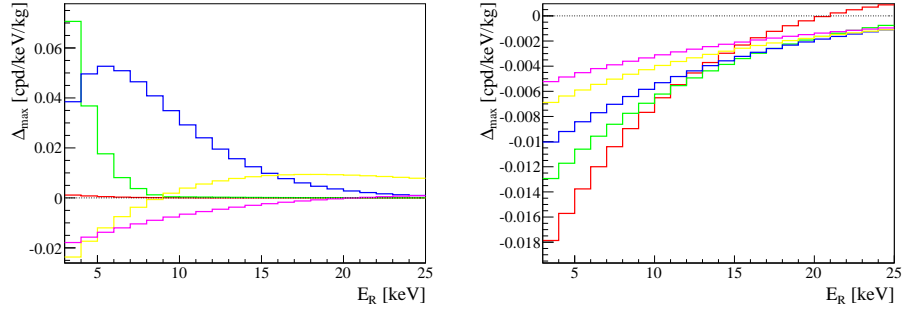
Figure 6.11: Expected maximum minus minimum modulation amplitude in TeO$_2$ for different WIMP masses (M_χ) as a function of the recoil energy, assuming a cross section of 10^{-41} cm^2. Left: $M_\chi = 5$ GeV in red, $M_\chi = 10$ GeV in green, $M_\chi = 20$ GeV in blue, $M_\chi = 50$ GeV in yellow and $M_\chi = 100$ GeV in purple. Right: $M_\chi = 100$ GeV in red, $M_\chi = 150$ GeV in green, $M_\chi = 200$ GeV in blue, $M_\chi = 300$ GeV in yellow and $M_\chi = 400$ GeV in purple. Some masses show a modulation phase inversion.

Range	Mod. Amp. (A)	Period (T)	Phase (t_0)	Mod. fit	Flat fit
[keV]	[cpd/keV/kg]	[d]	[d]	χ^2/ndf	χ^2/ndf
$10 \div 15$	0.107 ± 0.020	250 ± 15	355 ± 14	$16.86/10$	$46.62/13$
$15 \div 20$	0.032 ± 0.012	309 ± 56	332 ± 40	$10.63/10$	$17.7/13$
$20 \div 25$	0.024 ± 0.011	365 ± 56	294 ± 44	$11.38/10$	$16.11/13$
$25 \div 30$	0.031 ± 0.010	359 ± 47	279 ± 32	$4.976/10$	$14.57/13$
$30 \div 35$	0.016 ± 0.012	490 ± 420	260 ± 170	$7.503/10$	$9.382/13$
$35 \div 40$	0.035 ± 0.013	730 ± 415	9 ± 71	$12.82/10$	$20.08/13$
$40 \div 45$	0.013 ± 0.014	730 ± 280	-110 ± 99	$15.49/10$	$16.62/13$
$45 \div 50$	0.0074 ± 0.0070	237 ± 72	337 ± 84	$8.664/10$	$9.926/13$
$50 \div 55$	0.0090 ± 0.0031	204 ± 16	331 ± 17	$4.778/10$	$13.3/13$
$55 \div 60$	0.0067 ± 0.0024	231 ± 14	400 ± 6	$23.41/10$	$31.28/13$

Table 6.1: Fit results for all considered energy ranges. The only intervals that seem to have interesting results are the $15 \div 20$ keV, $20 \div 25$ keV and $25 \div 30$ keV ones. In particular they show a period compatible with 1 y and a phase compatible with a phase inversion (maximum of modulated signal on December 2nd) within $1\,\sigma$, apart in the case of the $25 \div 30$ keV phase, where $2\,\sigma$ are needed. The remaining energy regions are not compatible with the presence of a signal modulation with a period of 1 y having a modulation amplitude compatible with zero or a period non compatible with 1 y and/or at the maximum of the allowed range $(730\,\text{d} = 2\,\text{y})$.

Conclusions

In this Ph. D. work I developed the low energy analysis and I studied the annual modulation of the counting rate within the CUORE-0 detector.

To this end, the first step is an improved version of the software-generated low energy trigger. This new version of the trigger shows a 100% detection efficiency plateau, to be compared with the older implementation that reached a $\lesssim 90\%$ plateau efficiency. Additionally new tools have been introduced for the data quality at low energy. In particular, it is now possible to evaluate the trigger efficiency with *a priori* information without the need of a dedicated measurement.

Thanks to an energy calibration check, performed at the end of the standard analysis procedure, it resulted that 22 bolometers out of 52 are usable for the low energy studies. At the same time, the overall CUORE-0 calibration uncertainty is estimated as $0.15\,\mathrm{keV}$ at $28.03\,\mathrm{keV}$.

Subsequently, after an accurate event selection, the low-energy spectrum of CUORE-0 is produced. The counting rate ranges from $2.2\,\mathrm{cpd/keV/kg}$ at $10\,\mathrm{keV}$ to $0.05\,\mathrm{cpd/keV/kg}$ at $60\,\mathrm{keV}$. The spectrum shows the presence of two bumps between 30 and $45\,\mathrm{keV}$, whose origin is currently under investigation, probably due to more peaks summed together or two β-spectra.

Finally, an annual modulation fit has been performed for data arising from ten different ranges of the energy spectrum, of $5\,\mathrm{keV}$ each: starting from $10 \div 15\,\mathrm{keV}$ up to $55 \div 60\,\mathrm{keV}$. The exposure is $5.00\,\mathrm{kg} \cdot \mathrm{y}$ for the lower interval and $9.25\,\mathrm{kg} \cdot \mathrm{y}$ for the others. The fits show a possible indication of a modulation signal. In the $15 \div 20\,\mathrm{keV}$, $20 \div 25\,\mathrm{keV}$ and $25 \div 30\,\mathrm{keV}$ regions, results are compatible within $1\,\sigma$ with a period of $1\,\mathrm{y}$ and with an inversion of phase with respect June 2nd , while in the other cases the signal is not compatible with the presence of a modulated signal with a period of $1\,\mathrm{y}$. In particular, in the range $10 \div 15\,\mathrm{keV}$, the period of the modulation is more than $7\,\sigma$ smaller than $1\,\mathrm{y}$.

In conclusion, given the small exposure, the large errors and the reduced number of measured annual cycles, in addition to some preliminary results that indicate that it is possible to obtain a non-null modulation amplitude starting from a flat distribution quite easily, there are no clear evidences for a DM signal. CUORE, with its mass 19 times larger than CUORE-0 and with more annual cycles, will be able to see if an annual signal modulation is present.

Appendix A

$OT_{99\%}$ values

In Tab.A.1 and Tab.A.2 are listed the $OT_{99\%}$ values for each channel in each dataset. The $OT_{99\%}$ is the energy at which the OT reaches a trigger efficiency of 99%. As explained in sec.4.3 and sec.4.4 the trigger threshold (the θ of eq.(4.12)), at which the 50% efficiency is reached, is set at $3\,\sigma$ from 0, where σ is the baseline resolution, hence 99% efficiency is reached at $5.3\,\sigma$ from 0. Values presented in these tables are obtained using the erf and are given in keV.

		dataset									
channel		2079	2085	2088	2091	2097	2100	2103	2109	2124	2130	2139
	2	4.94595	5.16549	6.05609	6.16278	5.42552	5.10299	5.22638	6.05807	5.31037	5.25117	5.22974
	3	5.63652	5.5987	5.03542	4.81624	4.75605	4.65815	4.94849	4.90556	5.35692	5.79903	4.05414
	4	5.57923	6.61896	5.99317	5.40029	5.30189	5.42745	5.33237	5.43592	6.10156	5.91752	4.41081
	5	18.1072	19.5519	19.9026	18.5734	18.7193	18.7219	18.4891	18.5272	19.4732	19.4507	16.7353
	6	4.25773	4.50329	4.29497	4.40292	4.08958	4.26534	4.48596	4.22423	4.28799	4.82903	3.86012
	7	5.96975	6.68238	6.43754	6.26829	6.11073	6.29615	6.38192	6.30071	6.3299	7.02801	5.66967
	8	6.19583	7.28333	7.70083	7.04838	6.63634	7.13897	7.45867	7.57634	7.118	7.37915	6.22906
	9	5.38943	5.30785	5.99212	6.15873	5.79608	5.57232	5.65685	5.46766	6.99615	7.0438	4.78583
	11	6.92969	6.4614	6.78004	6.64292	6.4868	6.43354	6.39606	6.39949	6.86424	7.50897	5.15013
	12	5.06853	4.37567	4.76245	4.47063	4.2921	4.38627	4.37708	4.37464	4.60593	5.32387	4.01368
	13	9.88315	7.60821	8.14678	7.4366	7.51481	7.82828	7.58973	7.20492	7.8349	10.359	7.67585
	14	7.66423	6.86607	7.00125	7.07126	6.76763	7.06088	7.12421	6.81454	7.77661	7.53343	5.54385
	15	13.5237	14.8781	14.7113	14.609	14.3888	14.4857	14.4199	14.8743	17.8891	14.6995	12.572
	16	7.48677	8.9899	9.11327	8.78252	8.71558	8.81719	8.7841	8.80248	10.3178	9.30722	7.49521
	17	5.08598	4.99332	4.89934	4.77673	4.57517	4.74449	4.76204	4.72757	5.38607	5.29761	4.30323
	18	4.2793	4.37323	4.27475	4.22682	4.12281	4.20623	4.44743	6.95073	4.48515	4.73772	3.70126
	19	4.34437	4.74466	4.53461	4.43132	4.34041	4.50842	4.66933	4.71378	5.11771	4.88458	3.85207
	20	6.96806	7.29076	7.34883	6.98941	6.93376	7.13688	7.14231	7.05865	7.21824	7.67848	6.48353
	21	5.60143	5.44662	5.30159	5.06197	4.95737	5.10431	5.12433	4.91723	5.05016	5.98282	4.2671
	22	30.312	26.4926	22.3174	19.5708	20.6938	21.2991	21.9515	21.6552	24.4516	13.7297	20.8201
	23	5.97944	5.62691	6.03637	5.8001	5.557	5.81094	5.82771	7.0349	6.74027	7.18655	5.05273
	24	7.06198	5.34981	5.85661	5.70126	5.47783	5.6824	5.78173	5.61068	6.21053	6.67444	4.84378
	25	7.04811	5.95534	6.17937	5.86941	5.81884	5.95597	5.87722	5.89849	5.9516	7.88638	4.82962
	26	7.01571	5.69158	5.88512	5.67082	5.57363	5.50594	5.70719	5.37654	6.30274	7.62477	5.55719

Table A.1: OT$_{99\%}$ values for channels from 2 to 25 (1 and 10 are excluded) as a function of the dataset. Numbers in keV.

channel	2079	2085	2088	2091	2097	2100	2103	2109	2124	2130	2139
27	27.1249	27.2402	34.5989	34.7394	35.3072	35.0053	35.7426	35.0877	37.0988	35.7806	27.7252
28	8.28595	5.68407	6.73538	6.31158	6.23807	6.2672	6.17176	6.40787	7.00621	7.10149	5.10898
29	9.82445	9.75008	10.9235	10.6197	10.5018	10.5736	10.7096	10.6073	11.6132	10.5717	8.92306
30	12.1347	7.11078	9.00579	8.60324	8.03474	7.55059	7.41475	7.38149	8.83491	8.20779	5.91149
31	9.47389	6.56483	5.89921	5.77638	6.13723	5.73314	5.70446	5.70767	6.41278	9.96272	5.15217
32	5.39744	5.68121	6.02721	5.40555	5.35753	5.53085	5.49903	5.62819	5.66031	6.53305	5.0492
33	9.78834	9.54928	9.48977	9.34248	9.25432	9.3688	9.53143	9.4246	9.32336	10.5841	8.93959
34	8.47518	8.4353	8.49334	8.46429	8.31524	8.47484	8.55167	8.45912	8.37554	9.77758	7.59745
35	19.1277	23.4043	33.4384	36.8903	18.8256	18.8608	17.8677	18.6366	19.6935	23.5319	19.6457
36	4.91724	4.99383	5.42301	5.52989	4.93085	4.64741	4.94657	4.88763	5.50694	7.23074	4.01862
37	11.8646	11.503	11.7247	11.6312	11.6591	11.6131	11.8242	11.5855	12.0101	14.819	9.94963
38	7.36816	6.47801	7.09233	6.88017	6.60104	6.61	6.63379	6.77172	7.2139	9.80996	5.974
39	9.91109	7.77288	8.64681	8.2662	8.06164	8.263	10.6208	10.4749	8.07472	11.3815	7.6359
40	6.99447	7.27316	7.60673	7.54424	7.28174	7.46008	7.51421	7.29898	10.5636	7.8432	5.99897
41	5.78726	5.84428	6.50829	6.19681	6.15112	6.1889	6.2764	6.23519	6.46029	6.42933	5.10453
42	5.77889	5.9269	6.03188	5.95233	5.79624	5.76303	5.72513	5.9648		11.0386	6.75122
43	83.6662	16.5338	11.1335	10.1885	10.3547	9.29084	9.45705	10.0664		14.0192	8.02012
44	4.7192	5.01717	4.91536	4.75273	4.89223	4.60736	4.7094	4.75975	6.80798	5.89714	4.58033
45	5.05928	5.27691	5.21666	5.18118	5.08254	5.21657	5.39259	5.2132	5.2517	6.05752	4.6708
46	4.61031	4.12372	4.32222	4.21147	4.02129	4.30701	4.36968	4.30795	4.24581	5.816	4.09948
47	8.31393	8.03147	8.05864	7.83276	7.63331	7.9436	8.03673	8.25418	8.27009	10.9589	7.63361
48	6.93639	6.57556	6.65386	6.4674	6.3059	6.42363	6.4984	6.47202	6.42554	7.50422	5.95389
50	7.88833	12.1719	9.48499	9.93941	9.37678	10.2182	9.60356	9.81206	11.5199	5.87914	5.56113
51	9.27941	8.17517	8.03706	8.61608	7.75807	7.81235	8.07695	7.87604	8.16572	10.2403	7.15437
52	12.9104	7.69106	7.74467	7.75382	7.76462	7.50493	8.09504	8.01387	7.44536	11.1813	7.87801

Table A.2: $OT_{99\%}$ values for channels from 26 to 52 (49 is excluded) as a function of the dataset. Channels 42 and 43 in dataset 2124 have no $OT_{99\%}$ since they are excluded from the analysis. Numbers in keV.

Appendix B

Low noise runs

Baseline resolution for all the CUORE-0 channels in all the considered datasets reported in Tab.3.1 as function of the time. The x-axis is in days since January 1st 2013 to be consistent with the modulation spectra, while the y-axis is in keV. The dashed line represents the value over which the resolution is considered too large (hence noise too high) and runs are discarded from the analysis. This value is defined as the median $+ 2$ RMS of the distribution. From this calculation are excluded the five runs discussed in sec.6.2.1.

Fig.B.1 for channels $2 \div 5$.
Fig.B.2 for channels $6 \div 9$.
Fig.B.3 for channels $11 \div 15$.
Fig.B.4 for channels $16 \div 20$.
Fig.B.5 for channels $21 \div 25$.
Fig.B.6 for channels $26 \div 30$.
Fig.B.7 for channels $31 \div 35$.
Fig.B.8 for channels $36 \div 40$.
Fig.B.9 for channels $41 \div 45$.
Fig.B.10 for channels $46 \div 51$.
Fig.B.11 for channels 52.

Fig.B.12 shows the comparison between the low energy spectra (bin width is 0.5 keV) obtained with three different cuts on the run resolutions: median $+$ 1 RMS, median $+ 2$ RMS and no cut, with exposures of 8.35 kg·y, 9.25 kg·y and 9.64 kg·y, respectively. Given that the median$+2$ RMS and the median$+1$ RMS spectra differ only in the first two bins after 10 keV (the lower limit of the analyzed spectrum), with a 0.90 kg · y gain in exposure and that the difference between the median $+ 2$ RMS and the no cut spectra extends to higher energies with a 0.39 kg · y loss in exposure, it has been decided to apply the median $+$ 2 RMS cut in the analysis.
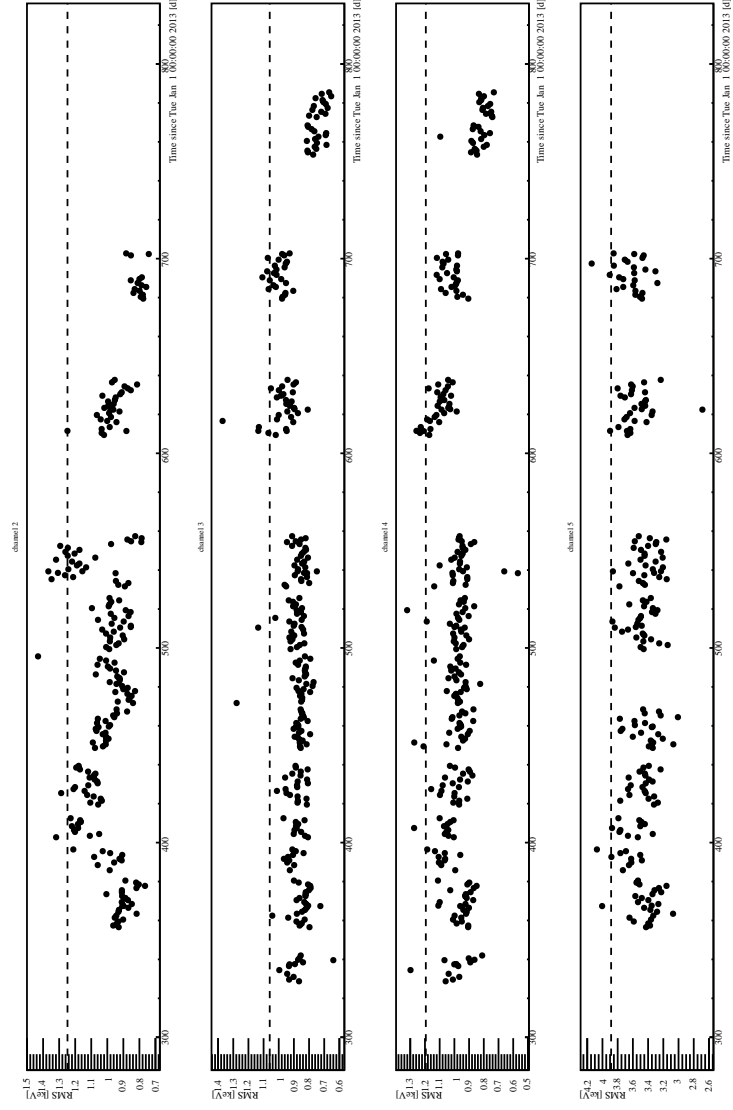
Figure B.1: Baseline resolution time trend for channels 2 ÷ 5. Each point corresponds to a single run, while the dashed line to the median + 2RMS of the distribution along the y-axis. Runs with a resolution below this line are maintained, the others are excluded from the analysis.
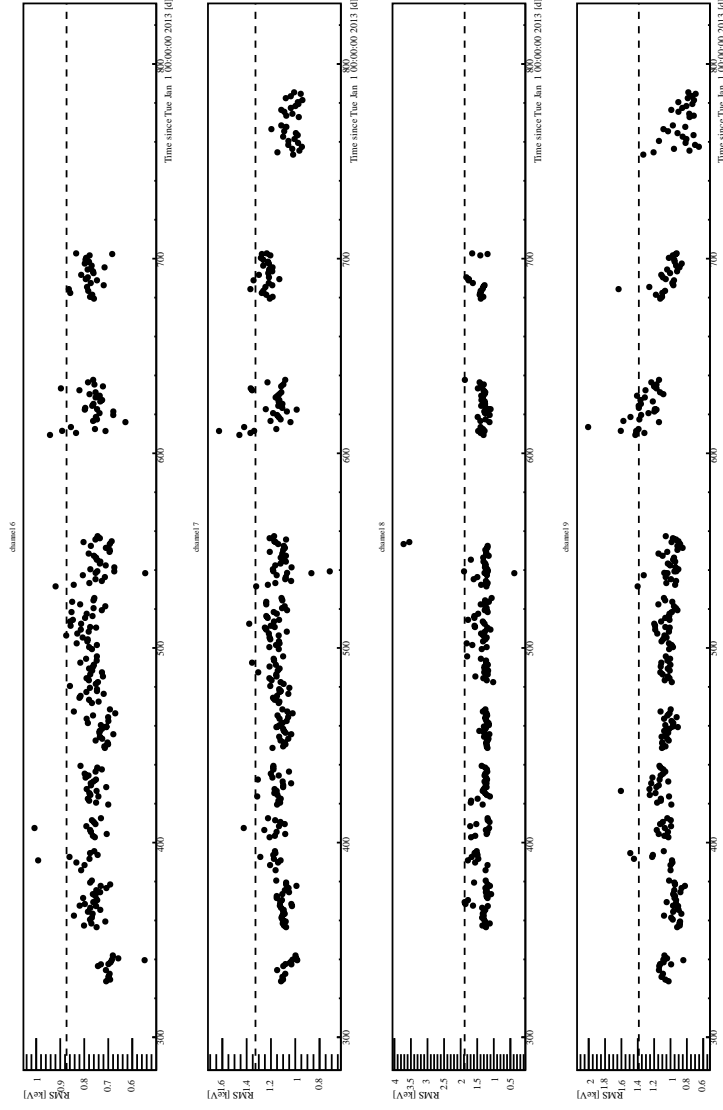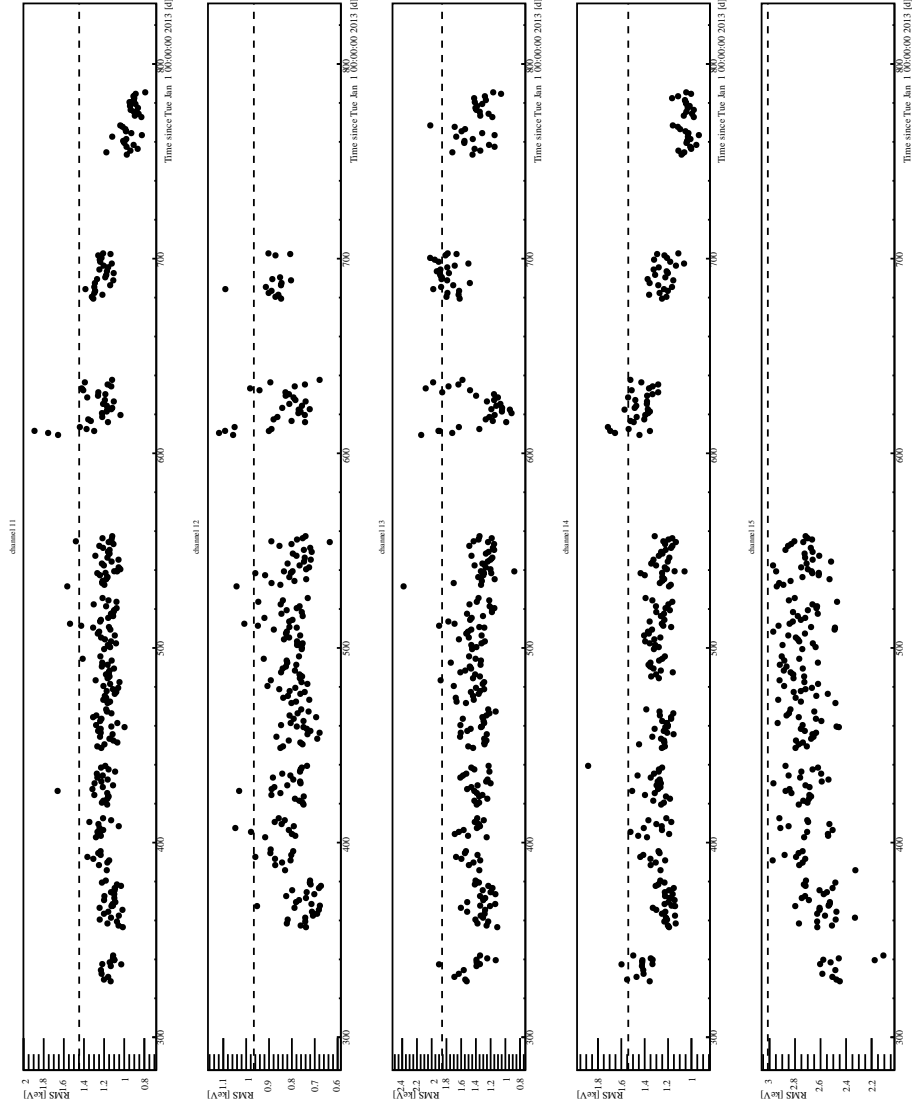
Figure B.2: Baseline resolution time trend for channels 6 ÷ 9. Each point corresponds to a single run, while the dashed line to the median + 2RMS of the distribution along the y-axis. Runs with a resolution below this line are maintained, the others are excluded from the analysis.
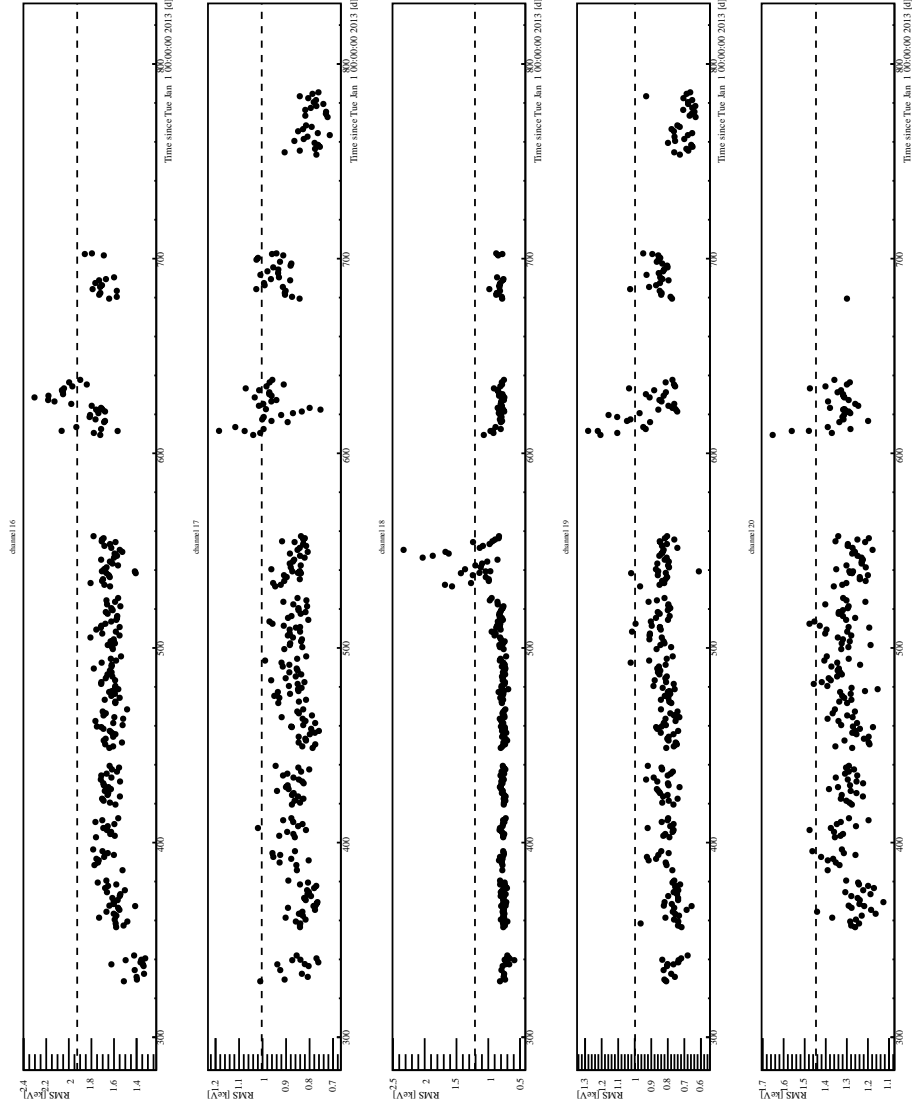
Figure B.3: Baseline resolution time trend for channels 11 ÷ 15. Each point corresponds to a single run, while the dashed line to the median + 2RMS of the distribution along the y-axis. Runs with a resolution below this line are maintained, the others are excluded from the analysis.
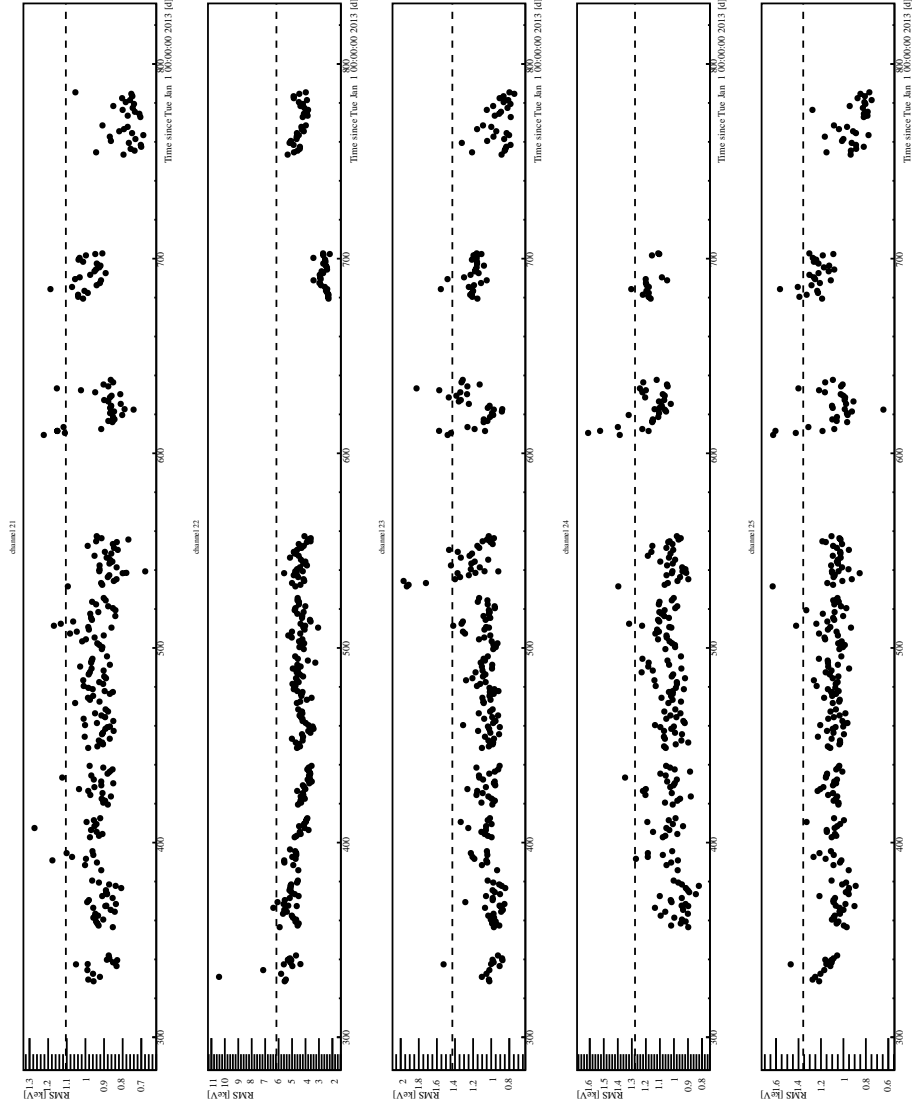
Figure B.4: Baseline resolution time trend for channels 16 ÷ 20. Each point corresponds to a single run, while the dashed line to the median + 2RMS of the distribution along the y-axis. Runs with a resolution below this line are maintained, the others are excluded from the analysis.

Figure B.5: Baseline resolution time trend for channels 21 ÷ 25. Each point corresponds to a single run, while the dashed line to the median + 2RMS of the distribution along the y-axis. Runs with a resolution below this line are maintained, the others are excluded from the analysis.
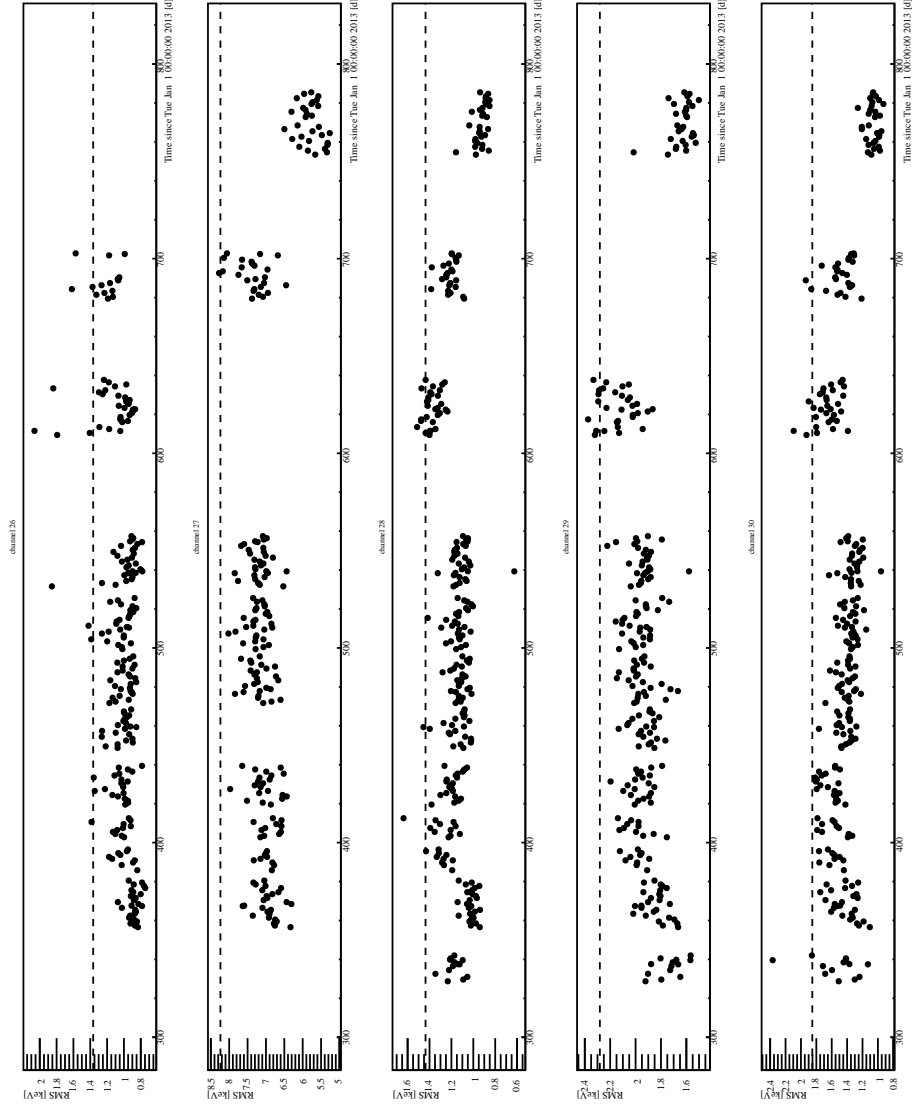
Figure B.6: Baseline resolution time trend for channels 26 ÷ 30. Each point corresponds to a single run, while the dashed line to the median + 2RMS of the distribution along the y-axis. Runs with a resolution below this line are maintained, the others are excluded from the analysis.

Figure B.7: Baseline resolution time trend for channels 31 ÷ 35. Each point corresponds to a single run, while the dashed line to the median + 2RMS of the distribution along the y-axis. Runs with a resolution below this line are maintained, the others are excluded from the analysis.
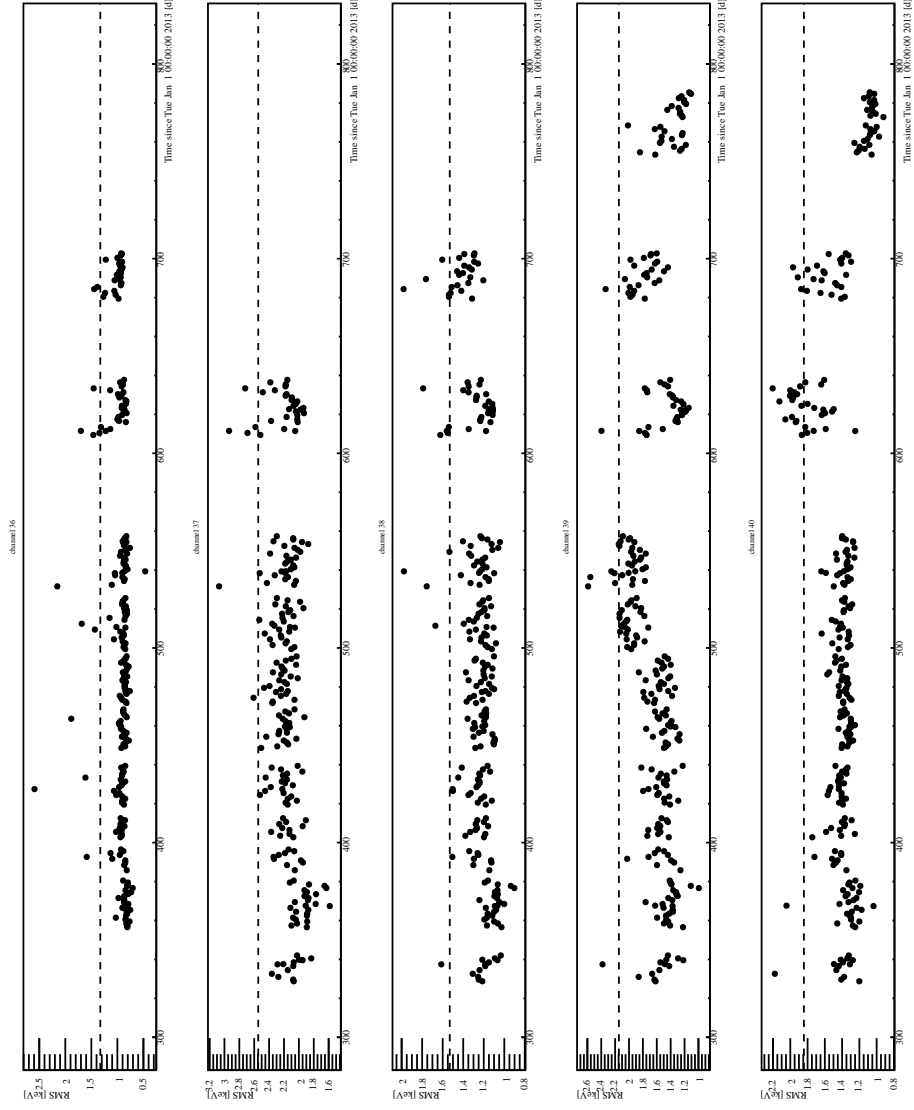
Figure B.8: Baseline resolution time trend for channels 36 ÷ 40. Each point corresponds to a single run, while the dashed line to the median + 2RMS of the distribution along the y-axis. Runs with a resolution below this line are maintained, the others are excluded from the analysis.

Figure B.9: Baseline resolution time trend for channels 41 ÷ 45. Each point corresponds to a single run, while the dashed line to the median + 2RMS of the distribution along the y-axis. Runs with a resolution below this line are maintained, the others are excluded from the analysis.
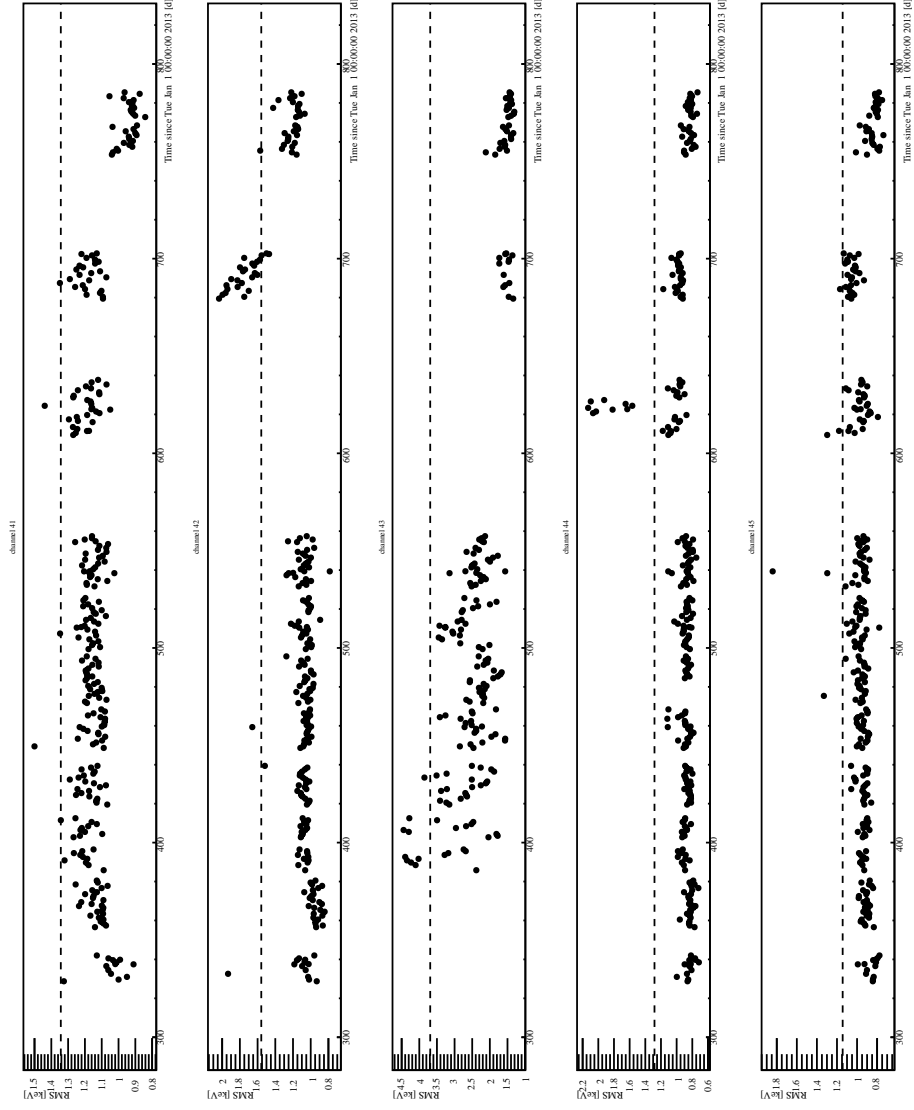
Figure B.10: Baseline resolution time trend for channels 46 ÷ 51. Each point corresponds to a single run, while the dashed line to the median + 2RMS of the distribution along the y-axis. Runs with a resolution below this line are maintained, the others are excluded from the analysis.
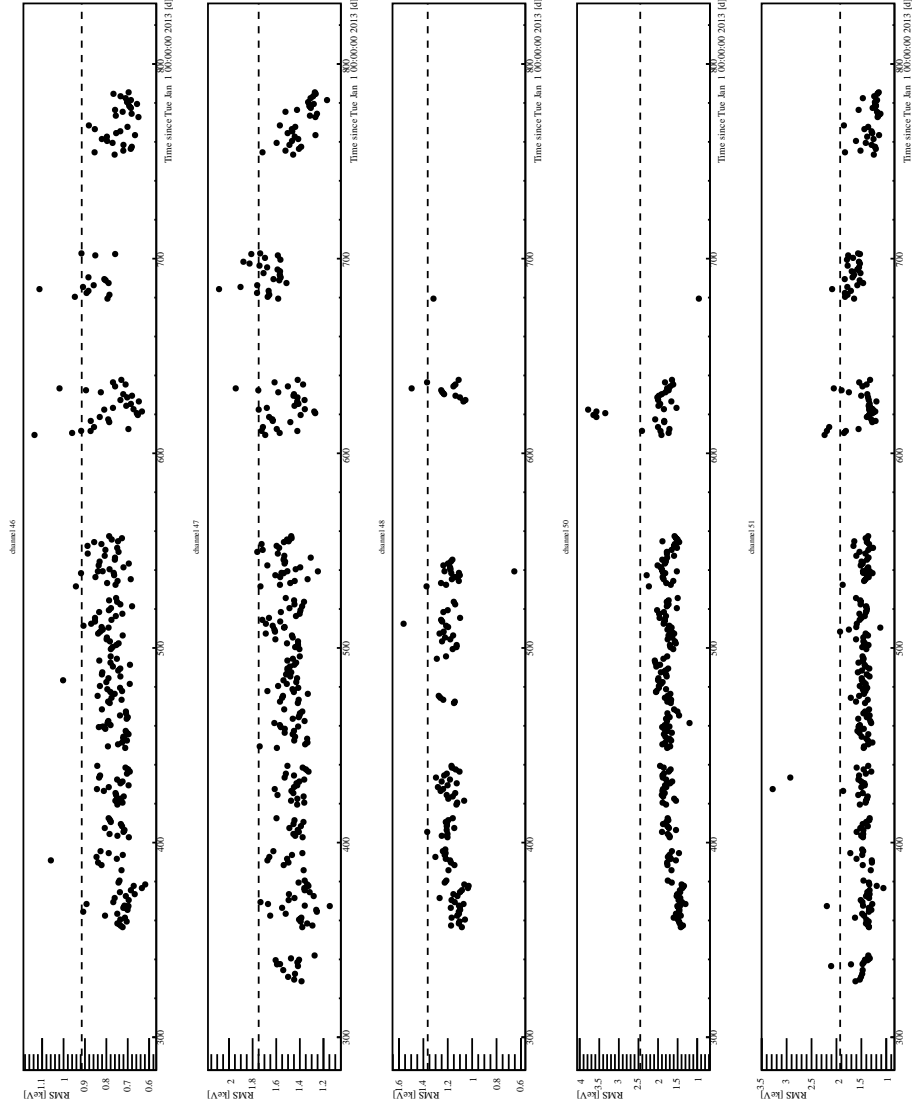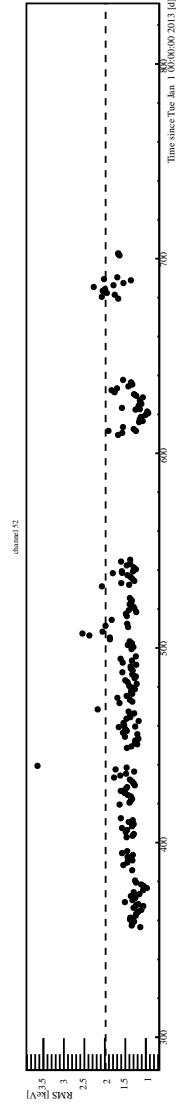
Figure B.11: Baseline resolution time trend for channel 52. Each point corresponds to a single run, while the dashed line to the median + 2RMS of the distribution along the y-axis. Runs with a resolution below this line are maintained, the others are excluded from the analysis.
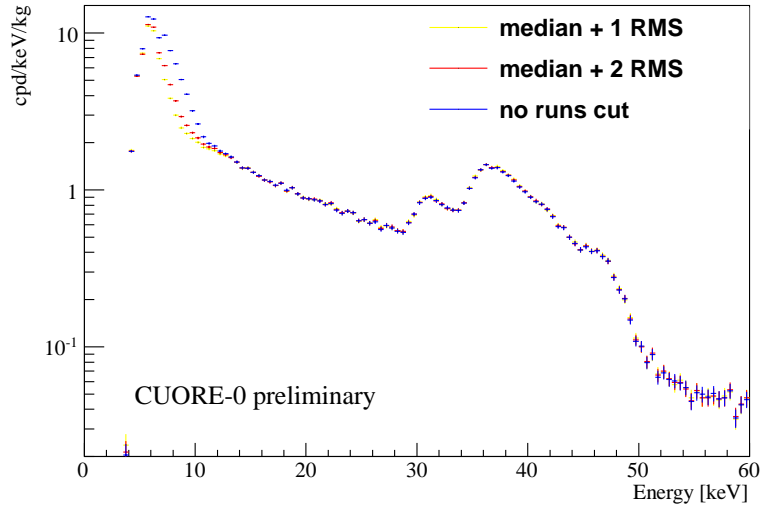
Figure B.12: Energy spectra (bin width is $0.5\,\mathrm{keV}$) with obtained with three different cuts on the run resolutions: median $+ 1\,\mathrm{RMS}$ ($8.35\,\mathrm{kg} \cdot \mathrm{y}$ exposure), median $+ 2\,\mathrm{RMS}$ ($9.25\,\mathrm{kg} \cdot \mathrm{y}$ exposure) and no cut ($9.64\,\mathrm{kg} \cdot \mathrm{y}$ exposure). Median and RMS are evaluated for each channel from its run resolutions distribution. Channels used to produce these spectra are the 22 indicated in Tab.5.4.

Appendix C

Modulation fits

Fits to the time spectra in the following energy ranges (the ones not shown in sec.6.4):

- $30 \div 35\,\mathrm{keV}$ (Fig.C.1),
- $35 \div 40\,\mathrm{keV}$ (Fig.C.2),
- $40 \div 45\,\mathrm{keV}$ (Fig.C.3),
- $45 \div 50\,\mathrm{keV}$ (Fig.C.4),
- $50 \div 55\,\mathrm{keV}$ (Fig.C.5),
- $55 \div 60\,\mathrm{keV}$ (Fig.C.6).

All of these intervals have a fit which is not compatible with the presence of an annual modulation for one or more of these reasons: modulation amplitude compatible with $0\,\mathrm{cpd/keV/kg}$, period non compatible with $1\,\mathrm{y}$ and/or at the maximum of the allowed range ($730\,\mathrm{d} = 2\,\mathrm{y}$).

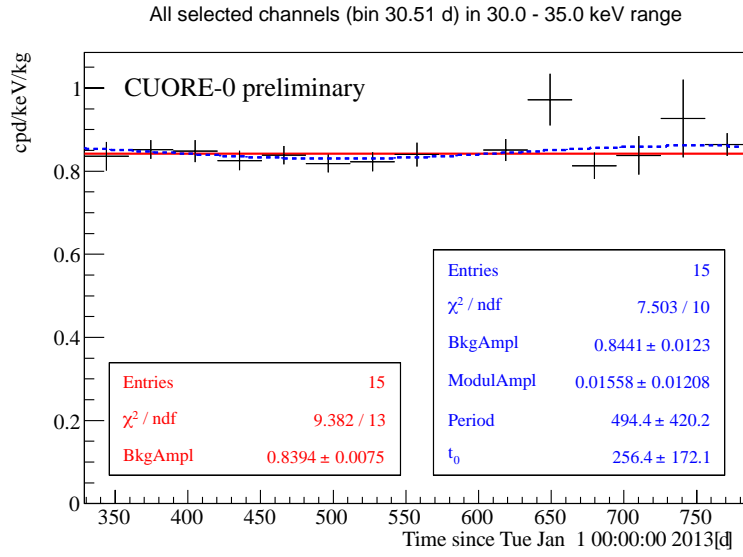All selected channels (bin 30.51 d) in 30.0 - 35.0 keV range

Figure C.1: Modulation binned fits (bin width of 30.51 d) in the energy range $30 \div 35$ keV. In red solid line the flat fit (results on left pad), in blue dashed line the free T and t_0 fit (results on the right pad). The accumulated exposure is 9.25 kg·y. The free phase and period fit sees a modulation of 0.016 cpd/keV/kg almost compatible with the absence of signal.

Figure C.2: Modulation binned fits (bin width of $30.51\,\mathrm{d}$) in the energy range $35 \div 40\,\mathrm{keV}$. In red solid line the flat fit (results on left pad), in blue dashed line the free T and t_0 fit (results on the right pad). The accumulated exposure is $9.25\,\mathrm{kg \cdot y}$. The free phase and period fit sees a modulation of $0.035\,\mathrm{cpd/keV/kg}$ amplitude with a period at the maximum allowed value.

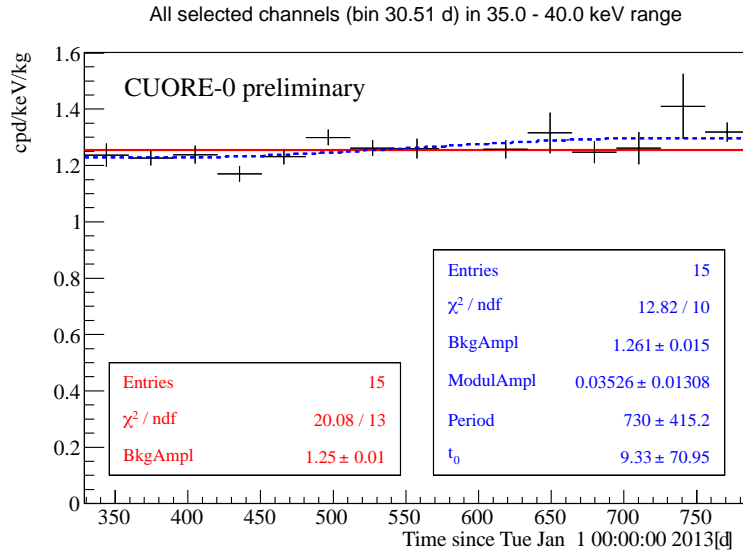All selected channels (bin 30.51 d) in 40.0 - 45.0 keV range

Figure C.3: Modulation binned fits (bin width of 30.51 d) in the energy range $40 \div 45$ keV. In red solid line the flat fit (results on left pad), in blue dashed line the free T and t_0 fit (results on the right pad). The accumulated exposure is 9.25 kg·y. The free phase and period fit sees a modulation of 0.013 cpd/keV/kg compatible with the absence of signal and a period at the maximum allowed value.

All selected channels (bin 30.51 d) in 45.0 - 50.0 keV range

Entries	15
χ^2 / ndf	9.926 / 13
BkgAmpl	0.2953 ± 0.0044

Entries	15
χ^2 / ndf	8.664 / 10
BkgAmpl	0.296 ± 0.005
ModulAmpl	0.007394 ± 0.006928
Period	237 ± 71.6
t_0	336.8 ± 83.9

Figure C.4: Modulation binned fits (bin width of $30.51\,\mathrm{d}$) in the energy range $45 \div 50\,\mathrm{keV}$. In red solid line the flat fit (results on left pad), in blue dashed line the free T and t_0 fit (results on the right pad). The accumulated exposure is $9.25\,\mathrm{kg\cdot y}$. The free phase and period fit sees a modulation of $0.0073\,\mathrm{cpd/keV/kg}$ almost compatible with the absence of signal.
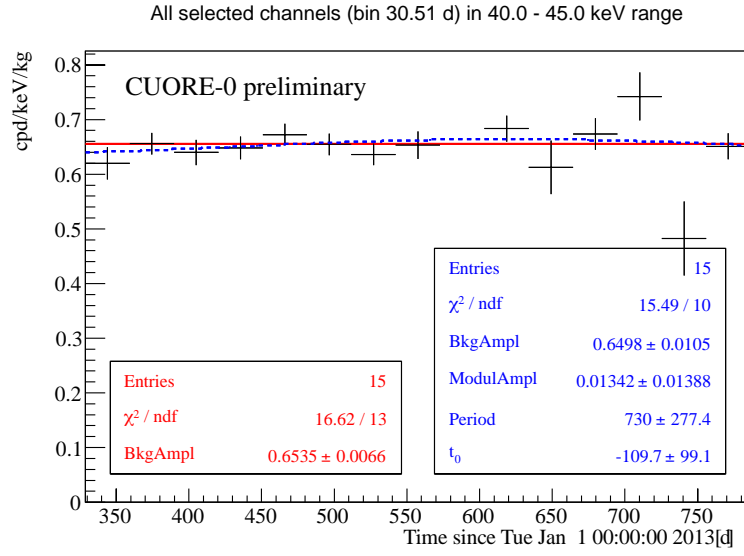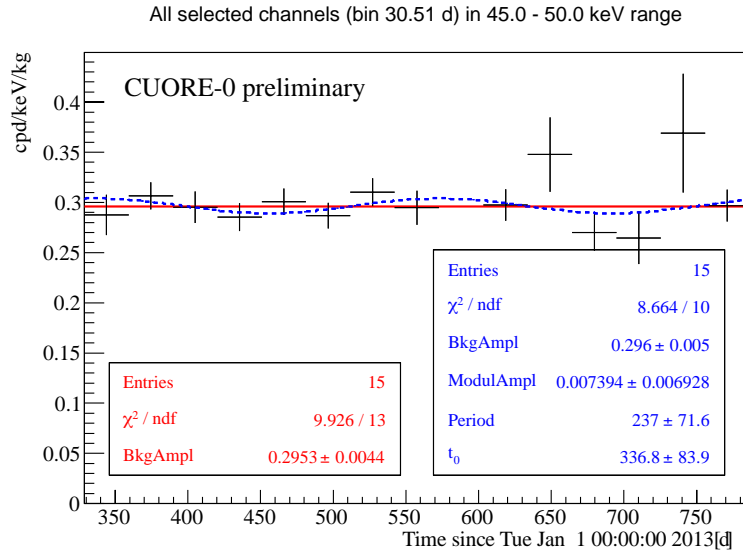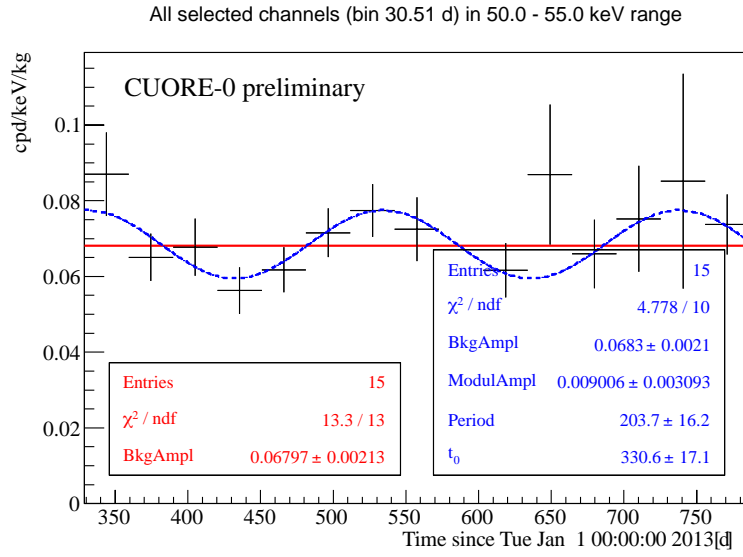
Figure C.5: Modulation binned fits (bin width of 30.51 d) in the energy range $50 \div 55$ keV. In red solid line the flat fit (results on left pad), in blue dashed line the free T and t_0 fit (results on the right pad). The accumulated exposure is 9.25 kg·y. The free phase and period fit sees a modulation of 0.0090 cpd/keV/kg amplitude with a period far from 1 y of about $10\,\sigma$.

All selected channels (bin 30.51 d) in 55.0 - 60.0 keV range

Entries	15
χ^2 / ndf	31.28 / 13
BkgAmpl	0.04491 ± 0.00173

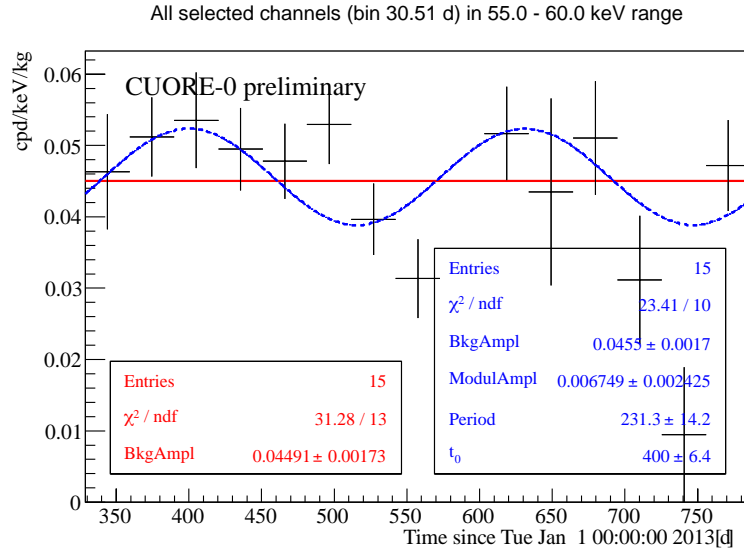|	
Entries	15
χ^2 / ndf	23.41 / 10
BkgAmpl	0.0455 ± 0.0017
ModulAmpl	0.006749 ± 0.002425
Period	231.3 ± 14.2
t_0	400 ± 6.4

CUORE-0 preliminary

Figure C.6: Modulation binned fits (bin width of 30.51 d) in the energy range $55 \div 60$ keV. In red solid line the flat fit (results on left pad), in blue dashed line the free T and t_0 fit (results on the right pad). The accumulated exposure is 9.25 kg·y. The free phase and period fit sees a modulation of 0.0067 cpd/keV/kg amplitude with a period far from 1 y more than $9\,\sigma$, while the phase is at the maximum allowed value.

Bibliography

[1] F. Zwicky, *Republication of: The redshift of extragalactic nebulae.* Gen. Relat. Gravit. **41**, 207 (2009). 4

[2] B. Ryden, *Introduction to cosmology.* Addison-Wesley (2003). 4

[3] P. A. R. Ade *et al.*, *Planck 2013 results. I. Overview of products and scientific Results.* Astron. Astrophys. **571**, A1 (2014). 5, 6

[4] V. C. Rubin, and W. K. Ford, Jr., *Rotation of the Andromeda Nebula from a Spectroscopic Survey of Emission Regions.* Astrophys. J. **159**, 379 (1970). 6

[5] K. G. Begeman, A. H. Broeils, and R. H. Sanders, *Extended rotation curves of spiral galaxies. Dark haloes and modified dynamics.* MNRAS **249**, 523 (1991). 7

[6] G. G. Raffelt, *Dark matter: Motivation, candidates and searches.* arXiv:hep-ph/9712538 (1997). 7

[7] R. G. Carlberg *et al.*, *The Ω_M-Ω_Λ Dependence of the Apparent Cluster Ω.* Astrophys. J. **516**, 552 (1999). 7

[8] R. G. Carlberg *et al.*, *Galaxy Cluster Virial Masses and Omega.* Astrophys. J. **462**, 32 (1996). 7

[9] A. E. Evrard, C. A. Metzler, and J. F. Navarro, *Mass Estimates of X-Ray Clusters.* Astrophys. J. **469**, 494 (1996). 7

[10] I. Smail *et al.*, *A comparison of direct and indirect mass estimates for distant clusters of galaxies.* Astrophys. J. **479**, 70 (1997). 7

[11] http://hubblesite.org/ 9

[12] H. Dahle *et al.*, *Weak Gravitational Lensing by a Sample of X-Ray–luminous Clusters of Galaxies. II. Comparison with Virial Masses.* Astrophys. J. **579**, 227 (2002). 9

[13] R. Coladonato, *Cosmic Background Explorer.* ELV payload environment (1991). 10

[14] C. L. Bennett *et al.*, *Nine-Year Wilkinson Microwave Anisotropy Probe (WMAP) Observations: Final Maps and Results.* Astrophys. J. Suppl. S. **208**, 20 (2013). 10, 11

[15] R. Adam *et al.*, *Planck 2015 results. I. Overview of products and scientific results.* arXiv:1502.01582 (2015). 10, 11, 12

[16] S. Burles, K. M. Nollett, and M. S. Turner, *Big-bang nucleosynthesis: Linking inner space and outer space.* arXiv:astro-ph/9903300 (1999). 12

[17] K. A. Olive *et al.* (Particle Data Group), *Review of particle physics.* Chin. Phys. C, 38, 090001 (2014). 13, 18

[18] D. G. York *et al.*, *The sloan digital sky survey: Technical summary.* AJ **120**, 1579 (2000). 14

[19] P. J. E. Peebles, *Principles of physical cosmology.* Princeton Series in Physics, Princeton University Press, (1993). 14, 17

[20] L. Anderson *et al.*, *The clustering of galaxies in the SDSS-III Baryon Oscillation Spectroscopic Survey: baryon acoustic oscillations in the Data Releases 10 and 11 Galaxy samples.* MNRAS **441**, 24 (2014). 14

[21] M. Davis, M. Lecar, C. Pryor, and E. Witten, *The formation of galaxies from massive neutrinos.* Astrophys. J. **250**, 423 (1981). 14

[22] G. R. Blumenthal, S. M. Faber, J. R. Primack, and M. J. Rees, *Formation of galaxies and large-scale structure with cold dark matter.* Nature **311**, 517 (1984). 15

[23] B. Paczynski, *Gravitational microlensing by the galactic halo.* Astrophys. J. **304**, 1 (1986). 15

[24] K. Griest, *Galactic microlensing as a method of detecting massive compact halo objects.* Astrophys. J. **366**, **412** (1991). 15

[25] R. Nemiroff, *Probing galactic halo dark matter with microlensing.* A&A **247**, 73 (1991). 15

[26] A. De Rújula, P. Jetzer, and E. Masso, *On the nature of the dark halo of our galaxy.* A&A **254**, 99 (1992). 15

[27] C. Afonso *et al.*, *Limits on Galactic dark matter with 5 years of EROS SMC data.* A&A **400**, 951 (2003). 15

[28] http://chandra.harvard.edu/ 16

[29] M. Milgrom, *A modification of the Newtonian dynamics as a possible alternative to the hidden mass hypothesis.* Astrophys. J. **270**, 365 (1983). 16

[30] D. Clowe, A. Gonzalez, and M. Markevitch, *Weak-Lensing Mass Reconstruction of the Interacting Cluster 1 E 0657-558: Direct Evidence for the Existence of Dark Matter.* Astrophys. J. **604**, 596 (2004). 16, 17

[31] M. C. Weisskopf *et al.*, *An Overview of the Performance and Scientific Results from the Chandra X-Ray Observatory.* PASP **114**, 1 (2002). 16

[32] M. Johns, *The Giant Magellan Telescope (GMT).* Proc. SPIE **6267**, 762 (2006). 16

[33] G. Nurre, *Hubble Space Telescope.* Upper and Middle Atmospheric Density Modeling Requirements for Spacecraft Design and Operations, **73** (1987). 16

[34] D. Clowe *et al.*, *A direct empirical proof of the existence of dark matter.* Astrophys. J. Lett. **648**, L109 (2006). 17

[35] A. Mahdavi, H. Hoekstra, A. Babul, D. D. Balam, and P. L. Capak, *A dark core in abell 520.* Astrophys. J. **668**, 806 (2007). 17

[36] M. Bradač *et al.*, *Revealing the properties of dark matter in the merging cluster macs.* Astrophys. J. **687**, 959 (2008). 17

[37] R. Davis, Jr., D. S. Harmer, and K. C. Hoffman, *Search for neutrinos from the Sun.* Phys. Rev. Lett. **20**, 1205 (1968). 17

[38] J. N. Abdurashitov *et al.*, *Measurement of the solar neutrino capture rate with gallium metal.* Phys. Rev. C **60**, 055801 (1999). 17

[39] S. Fukuda *et al.*, *Solar ^{8}B and hep Neutrino Measurements from 1258 Days of Super-Kamiokande Data.* Phys. Rev. Lett. **86**, 5651 (2001). 17

[40] Q. R. Ahmad *et al.*, *Direct evidence for neutrino flavor transformation from neutral-current interaction in the Sudbury Neutrino Observatory.* Phys. Rev. Lett. **89**, 011301 (2002). 17

[41] Fixsen, D. J., *The Temperature of the Cosmic Microwave Background.* Astrophys. J. **707**, 916 (2009). 17

[42] G. Jungman, M. Kamionkowski, and K. Griest, *Supersymmetric dark matter.* Phys. Rep. **267**, 195 (1996). 18

[43] S. Dodelson, and L. M. Widrow, *Sterile Neutrinos as Dark Matter.* Phys. Rev. Lett. **72**, 17 (1994). 18

[44] K. Abazajian, G. M. Fuller, and M. Patel, *Sterile Neutrino Hot, Warm, and Cold Dark Matter.* Phys. Rev. D **64**, 023501 (2001). 18

[45] X. D. Shi, and G. M. Fuller, *A New Dark Matter Candidate: Non-thermal Sterile Neutrinos.* Phys. Rev. Lett. **82**, 2832 (1999). 18

[46] R. Peccei, and H. Quinn, *Constraints imposed by CP conservation in the presence of pseudoparticles.* Phys. Rev. D **16**, 1791 (1977). 18

[47] Baker, C. A *et al.*, *Improved Experimental Limit on the Electric Dipole Moment of the Neutron.* Phys. Rev. Lett. **97**, 131801 (2006). 18

[48] M. S. Turner, *Windows on the axion.* Phys. Rept. **197**, 67 (1990). 18

[49] M. Dine, and W. Fischler, *The not-so-harmless axion.* Phys. Lett. B **120**, 137 (1983). 18

[50] J. Preskill, M. B. Wise, and F. Wilczek, *Cosmology of the invisible axion.* Phys. Lett. B **120**, 127 (1983). 18, 19

[51] L. Abbott, and P. Sikivie, *A cosmological bound on the invisible axion.* Phys. Lett. B **120**, 133 (1983). 18

[52] J. E. Kim, and G. Carosi, *Axions and the strong CP problem.* Rev. Mod. Phys. **82**, 557 (2010). 18

[53] C. Hagmann, *A Search for Cosmic Axion.* Ph.D. thesis, University of Florida, Gainesville, FL 32611-8440 (1990). 19

[54] E. Arik *et al.*, *Probing eV-scale axions with CAST.* JCAP 02(2009)008 . 19

[55] Asztalos *et al.*, *High resolution search for dark-matter axions.* Phys. Rev. D **74**, 012006 (2006). 19

[56] F. Della Valle *et al.*, *The PVLAS experiment for measuring the magnetic birefringence of vacuum.* Nuovo Cimento Soc. Ital. Fis. C **36**, 41 (2013). 19

[57] E. W. Kolb, and M. S. Turner, *The Early Universe.* Addison-Wesley, Redwood City, (1989). 20

[58] S. P. Martin, *A Supersymmetry Primer.* arXiv:hep-ph/9709356v6 (2011). 21

[59] N. Craig, *The State of Supersymmetry after Run I of the LHC.* Lectures at the training week of the GGI workshop "Beyond the Standard Model after the first run of the LHC", arXiv:1309.0528v2 (2014). 21

[60] E. A. Baltz, M. Battaglia, M. E. Peskin, and T. Wizansky, *Determination of dark matter properties at high-energy colliders.* Phys. Rev. D **74**, 103521 (2006). 23

[61] Dan Hooper and Edward Baltz, *Strategies for Determining the Nature of Dark Matter.* Annu. Rev. Nucl. Part. Sci. **58**, 293 (2008). 23

[62] O. Adriani *et al.*, *The cosmic-ray positron energy spectrum measured by PAMELA.* Phys. Rev. Lett. **111**, 081102 (2013). 23, 25

[63] L. Accardo *et al.*, *High Statistics Measurement of the Positron Fraction in Primary Cosmic Rays of 0.5–500 GeV with the Alpha Magnetic Spectrometer on the International Space Station.* Phys. Rev. Lett. **113**, 121101 (2014). 23, 24, 25

[64] M. Boezio *et al.*, *Measurements of cosmic-ray electrons and positrons by the Wizard/CAPRICE collaboration.* Adv. Space Res. **27**, 669 (2001). 25

[65] R. L. Golden *et al.*, *Measurement of the positron to electron ratio in the cosmic rays above 5 GeV.* Astrophys. J. **457**, L103 (1996). 25

[66] J. J. Beatty *et al.*, *New Measurement of the Cosmic-Ray Positron Fraction from 5 to 15 GeV.* Phys. Rev. Lett. **93**, 241102 (2004). 25

[67] M. Aguilar *et al.*, *Cosmic-ray positron fraction measurement from 1 to 30 GeV with AMS-01.* Phys. Lett. B **646**, 145 (2007). 25

[68] M. Ackermann *et al.*, *Measurement of Separate Cosmic-Ray Electron and Positron Spectra with the Fermi Large Area Telescope.* Phys. Rev. Lett. **108**, 011103 (2012). 25

[69] P. Blasi, *The origin of the positron excess in cosmic rays.* Phys. Rev. Lett. **103**, 051104 (2009). 24

[70] T. Linden, and S. Profumo, *Probing the pulsar origin of the anomalous positron fraction with AMS-02 and Atmospheric Cherenkov Telescopes.* Astrophys. J. **772**, 18 (2013). 24

[71] L. Bergström, J. Edsjö, and G. Zaharijas, *Dark matter interpretation of recent electron and positron data.* Phys. Rev. Lett. **103**, 031103 (2009). 24

[72] D. P. Finkbeiner, L. Goodenough, T. R. Slatyer, M. Vogelsberger, and N. Weiner, *Consistent Scenarios for Cosmic-Ray Excesses from Sommerfeld-Enhanced Dark Matter Annihilation.* JCAP 1105(2011)002 . 24

[73] Y. Fukuda *et al.*, *Evidence for oscillation of atmospheric neutrinos.* Phys. Rev. Lett. **81**, 1562 (1998). 24

[74] M. G. Aartsen *et al.*, *Multipole Analysis of IceCube Data to Search for Dark Matter Accumulated in the Galactic Halo.* Eur. Phys. J. C **75**, 20 (2015). 24

[75] S. Adrián-Martínez *et al.*, *First results on dark matter annihilation in the Sun using the ANTARES neutrino telescope.* JCAP 11(2013)032. 24

[76] J. D. Lewin, and P. F. Smith, *Review of mathematics, numerical factors, and corrections for dark matter experiments based on elastic nuclear recoil.* Astropart. Phys. **6**, 87 (1996). 24

[77] A.K. Drukier, K. Freese, and D.N. Spergel, *Detecting cold dark-matter candidates.* Phys. Rev. D **33**, 3495 (1986). 26

[78] F.J. Kerr, and D. Lynden-Bell, *Review of galactic constants.* MNRAS **221** 1023 (1986). 26

[79] J. Primack, D. Seckel, and B. Sadoulet, *Detection of cosmic dark matter.* Annu. Rev. Nucl. Part. Sci. **38**, 751 (1988). 28

[80] R. H. Helm, *Inelastic and elastic scattering of 187-Mev electrons from selected even-even nuclei.* Phys. Rev. **104**, 1466 (1956). 28

[81] M. T. Ressell *et al.*, *Nuclear shell model calculations of neutralino-nucleus cross sections for Si-29 and Ge-73.* Phys. Rev. D **48**, 5519 (1993). 29

[82] V. I. Dimitrov, J. Engel, and S. Pittel, *Scattering of weakly interacting massive particles from Ge-73.* Phys. Rev. D **51**, R291 (1995). 29

[83] A. Alessandrello *et al.*, *The bolometers as nuclear recoil detectors.* Nucl. Instrum. Meth. A **409**, 451 (1998). 30

[84] S. Y. F. Chu, L. P. Ekstrom, and R. B. Firestone, *The Lund/LBNL nuclear data search.* Available at http://ie.lbl.gov/toi/index.asp 31, 81

[85] A. K. Drukier, K. Freese, and D. N. Spergel, *Detecting cold dark-matter candidates.* Phys. Rev. D **33**, 3495 (1986). 32

[86] R. Bernabei *et al.*, *First results from DAMA/LIBRA and the combined results with DAMA/NaI.* Eur. Phys. J. C **56**, 333 (2008). 34

[87] P. Belli *et al.*, *Observations of annual modulation in direct detection of relic particles and light neutralinos.* Phys. Rev. D **84**, 055014 (2011). 34

[88] R. Bernabei *et al.*, Model independent result on possible diurnal effect in DAMA/LIBRA-phase1. Eur. Phys. J. C **74**, 2827 (2014). 34

[89] R. Bernabei *et al.*, *The Annual Modulation Signature for Dark Matter: DAMA/LIBRA-Phase1 Results and Perspectives.* Adv. High Energy Phys. **2014**, Article ID 605659 (2014). 34, 35

[90] http://dmtools.brown.edu/ 36

[91] R. Bernabei *et al.*, *The liquid xenon set-up of the DAMA experiment.* Nucl. Instrum. and Meth. A **482**, 728 (2002). 37

[92] A. Hime, *DEAP & CLEAN detectors for low energy particle astrophysics.* AIP Conf. Proc. **842**, 852 (2006). 37

[93] T.Alexander *et al.*, *Light Yield in DarkSide-10: a Prototype Two-phase Liquid Argon TPC for Dark Matter Searches.* Astropart. Phys. **49**, 44 (2013). 37

[94] A Badertscher *et al.*, *ArDM: first results from underground commissioning.* JINST **8**, C09005 (2013). 37

[95] K. Abe *et al.*, *XMASS detector.* Nucl. Instr. Meth. A **716**, 78 (2013). 37

[96] G. J. Alner *et al.*, *Nuclear recoil limits from the ZEPLIN I liquid xenon WIMP dark matter detector.* New Astron. Rev. **49**, 245 (2005). 37

[97] G.J.Alner *et al.*, *First limits on WIMP nuclear recoil signals in ZEPLIN-II: a two phase Xe detector for dark matter detection.* Astropart. Phys. **28**, 287 (2007). 37

[98] D.Akimov *et al.*, *WIMP-nucleon cross-section results from the second science run of ZEPLIN-III.* Phys. Lett. B **709**, 14 (2012). 37

[99] J. Angle *et al.*, *First Results from the XENON10 Dark Matter Experiment at the Gran Sasso National Laboratory.* Phys. Rev. Lett. **100**, 021303 (2008). 37

[100] E. Aprile, *et al.*, *Dark Matter Results from 225 Live Days of XENON100 Data.* Phys. Rev. Lett. **109**, 181301 (2012). 37

[101] E. Aprile, *The XENON1T dark matter search experiment.* Springer Proc. Phys. **148**, 93 (2013). 37

[102] D. S. Akerib *et al.*, *The Large Underground Xenon (LUX) Experiment.* . Instrum. Meth. A **704**, 111 (2013). 37

[103] Mani Tripathi, *LZ: A 2nd Generation Direct Dark Matter Search Experiment.* presentation at TAUP 2013 (2013). 37

[104] M. Agostini *et al.*,The background in the neutrinoless double beta decay experiment GERDA. Eur. Phys. J. C **74**, 2764 (2014). 37

[105] C. E. Aalseth *et al.*, *CoGeNT: A search for low-mass dark matter using p-type point contact germanium detectors.* Phys. Rev. D **88**, 012002 (2013). 37

[106] D. G. Phillips II *et al.*, *The MAJORANA experiment: an ultra-low background search for neutrinoless double-beta decay.* J. Phys. Conf. Ser. **381**, 012044 (2012). 37

[107] E. Armengaud *et al.*, *Final results of the EDELWEISS-II WIMP search using a 4-kg array of cryogenic germanium detectors with interleaved electrodes.* Phys. Lett. B **702**, 329 (2011). 38

[108] R. Agnese *et al.*, *Silicon Detector Dark Matter Results from the Final Exposure of CDMS II.* Phys. Rev. Lett. **111**, 251301 (2013). 38

[109] R. Agnese *et al.*, *Search for Low-Mass WIMPs with SuperCDMS.* Phys. Rev. Lett. **112**, 241302 (2014). 38

[110] G. Angloher *et al.*, *Results on low mass WIMPs using an upgraded CRESST-II detector.* Eur. Phys. J. C **74**, 3184 (2014). 38

[111] S. Archambault *et al.*, *Dark Matter Spin-Dependent Limits for WIMP Interactions on ^{19}F by PICASSO.* Phys. Lett. B **682**, 185 (2009). 38

[112] E. Behnke *et al.*, *First Dark Matter Search Results from a 4-kg CF3I Bubble Chamber Operated in a Deep Underground Site.* Phys. Rev. D **86**, 052001 (2012). 38

[113] J. B. R. Battat *et al.*, *Updates from the Dark Matter Time Projection Chamber Group (DMTPC).* J. Phys. Conf. Ser. **469**, 012001 (2013). 38

[114] G. J. Alner *et al.*, *The DRIFT-II dark matter detector: Design and commissioning.* Nucl. Instrum. Meth. A **555**, 173 (2005). 38

[115] D. Santos *et al.*, *MIMAC: A Micro-TPC Matrix of Chambers for direct detection of Wimps.* J. Phys.: Conf. Ser. **65**, 012012 (2007). 38

[116] F. Cappella *et al.*, *On the potentiality of the $ZnWO_4$ anisotropic detectors to measure the directionality of Dark Matter.* Eur. Phys. J. C **73**, 2276 (2013). 38

[117] C. Kittel, *Introduction to Solid State Physics.* Wiley (1996). 40

[118] M. Shubin, T. Sunada, *Mathematical theory of lattice vibrations.* Pure and Appl. Math. Quaterly **2**, 745 (2006). 40

[119] F. Alessandria *et al.*, *The low energy spectrum of TeO_2 bolometers: results and dark matter perspective for the CUORE-0 and CUORE experiments.* JCAP 01(2013)038. 39, 71, 92

[120] Y. B. Levison, *Nonequilibrium Phonons in Nonmetallic Crystals.* Modern Problems in Condensed Matter Sciences **16**, 91 (1986). 41

[121] N.F. Mott, and J. H. Davies, *Metal insulator transition in doped semiconductors.* Phylos. Mag. B **42**, 845 (1980). 42

[122] A. Miller, and A. Abrahams, *Impurity conduction at low concentrations.* Phys. Rev. **120** (1960). 42

[123] N. Wang *et al.*, *Electrical and thermal properties of neutron-transmutation-doped Ge at 20 mK.* Phys. Rev. B **41**, 6 3761 (1990). 42

[124] K. M. Itoh *et. al.*, *Neutron transmutation doping of isotopically engineered Ge.* Appl. Phys. Lett. **64**, 2121 (1994). 42

[125] C. Arnaboldi *et al.*, *CUORE: a cryogenic underground observatory for rare event.* Nucl. Instrum. Meth. A **518**, 775 (2004). 47

[126] D. R. Artusa *et al.*, *Searching for neutrinoless double-beta decay of ^{130}Te with CUORE.* Adv. High Energy Phys. **2015**, Article ID 879871 (2015). 47

[127] S. R. Elliot, A. A. Hahn, M. K. Moe, *Direct evidence for two-neutrino double-beta decay in ^{82}Se.* Phys. Rev. Lett. **59**, 2020 (1987). 47

[128] G. Shaw, and F. Mandl, *Quantum Field Theory.* Wiley (1984). 48

[129] E. Majorana, *Teoria simmetrica dell'elettrone e del positrone.* Il Nuovo Cimento **14**, 171 (1937). 48

[130] J. Schechter, and J. W. F. Valle, *Neutrinoless double-β decay in $SU(2)\times U(1)$ theories.* Phys. Rev. D **25**, 2951 (1982). 48

[131] A. S. Barabash, *Double Beta Decay: Historical Review of 75 years of Research.* Phys. Atom. Nucl. **74**, 603 (2011). 48

[132] D. Tosi, *The search for neutrino-less double-beta decay.* arXiv:1402.1170 (2014). 48

[133] E. Andreotti *et al.*, ^{130}Te *Neutrinoless Double-Beta Decay with CUORI-CINO.* Astropart. Phys. **34**, 822 (2011). 49, 54

[134] C. Arnaboldi, G. Pessina, and E. Previtali, *A Programmable Calibrating Pulse Generator With Multi-Outputs and Very High Stability.* IEEE Trans. Nucl. Sci. **50**, 979 (2003). 49

[135] C. Arnaboldi *et al.*, *Production of high purity TeO_2 single crystals for the study of neutrinoless double beta decay.* J. Cryst. Growth **312**, 2999 (2010). 49

[136] F. Alessandria *et al.*, *CUORE crystal validation runs: results on radioactive contamination and extrapolation to CUORE background.* Astropart. Phys. **35**, 839 (2012). 50, 92

[137] http://www.aurubis.com/ 50

[138] D. R. Artusa *et al.*, in preparation. 50

[139] F. Alessandria *et al.*, *Validation of techniques to mitigate copper surface contamination in CUORE.* Astropart. Phys. **45**, 13 (2013). 50

[140] M. Clemenza, C. Maiano, L. Pattavina, and E. Previtali, *Radon-induced surface contaminations in low background experiments.* Eur. Phys. J. C **71**, 1 (2011). 50

[141] C. Brofferio *et al.*, *Electrical characterization of the low background Cu-PEN links of the CUORE experiment.* Nucl. Instrum. Meth. A **718**, 211 (2013). 50

[142] E. Andreotti *et al.*, *The low radioactivity link of the CUORE experiment.* JINST **4**, P09003 (2009). 50

[143] M. Vignati, *Model of the Response Function of CUORE Bolometers.* PhD thesis, Sapienza - Università di Roma (2009). 50, 66

[144] C. Arnaboldi *et al.*, *A programmable multichannel antialiasing filter for the CUORE experiment.* Nucl. Instrum. Meth. A **617**, 327 (2010). 51

[145] C. Arnaboldi *et al.*, *The front-end readout for CUORICINO, an array of macro-bolometers and MIBETA, an array of μ-bolometers.* Nucl. Instrum. Meth. A **520**, 578 (2004). 51

[146] C. Arnaboldi *et al.*, *The Programmable Front-End System for CUORICINO, An Array of Large-Mass Bolometers.* IEEE Trans. Nucl. Sci. **49**, 2440 (2002). 51

[147] K. Alfonso *et al.*, Search for Neutrinoless Double-Beta Decay of 130Te with CUORE-0. arXiv:1504.02454 (2015). 78

[148] C. P. Aguirre *et al.*, *Initial performance of the CUORE-0 experiment.* Eur. Phys. J. C **74**, 2956 (2014). 54

[149] K. Alfonso *et al.*, *Search for Neutrinoless Double-Beta Decay of ^{130}Te with CUORE-0.* arXiv:1504.02454 (2015). 54

[150] l. Canonica, *Results from the search for neutrinoless double beta decay of ^{130}Te with CUORE-0.* Presentation at Laboratori Nazionali del Gran Sasso (April 2015). 54

[151] F. Alessandria *et al.*, *Sensitivity and Discovery Potential of CUORE to Neutrinoless Double-Beta Decay.* arXiv:1109.0494 (2011). 55

[152] E. Gatti, and P. F. Manfredi, *Processing the signals from solid state detectors in elementary particle physics.* Riv. Nuovo Cim. **9N1**, 1 (1986). 56

[153] S. Di Domizio, F. Orio, and M. Vignati, *Lowering the energy threshold of large-mass bolometric detectors.* JINST **6**, P02007 (2011). 56

[154] Bracewell, R., *The Fourier Transform and Its Applications*, 3rd ed. McGraw-Hill (1999). 60

[155] W. H. Press, S. A. Teukolsky, W. T. Vetterling, and B. P. Flannery, *Numerical recipes in C (2nd ed.): the art of scientific computing.* Cambridge University Press (1992). 60

[156] J. Gibbs, *Fourier's series*, Nature **59**, 200 (1898).

60